Stimulated Emission Studies of Ultracold Rydberg Atoms

by

Erik Gallup Brekke

A dissertation submitted in partial fulfillment

of the requirements for the degree of

Doctor of Philosophy

(Physics)

at the

UNIVERSITY OF WISCONSIN-MADISON

2009

0.1 Abstract

Rydberg atoms have many novel properties that make them appealing, most noticeably their long lifetimes and very strong dipole interactions. This dissertation describes experiments involving the optical detection and manipulation of ultracold Rydberg atoms using a novel stimulated emission probe.

This stimulated emission probe was first used to explore the dynamics of ultracold Rydberg atoms. Two-photon excitation creates Rydberg atoms which can be observed via loss of atoms from the MOT, or by fluorescent emission. The addition of a stimulated-emission probe enabled further measurement of the rate of transfer from the Rydberg state. A model was developed to better understand the data, revealing that superradiant transfer is an important mechanism in the atom dynamics at these densities.

We have further performed non-degenerate four-wave mixing through the Rydberg states using the stimulated emission probe, causing preferential emission into a diffraction limited direction. This result can be optimized by detuning the excitation lasers from the Rydberg resonance, resulting in up to 50 percent of the light emitted in a diffraction limited direction.

The final experiment described in this dissertation is the investigation of atom-atom interactions within a small excitation volume. We have shown that these interactions can be enhanced through the application of resonant microwaves. Suppression of Rydberg atom excitation was qualitatively observed and quantitatively analyzed using a universal scaling law. This gave a measure of the atom-atom interaction strength in agreement with the theoretical prediction. This represents a large advance in the understanding of Rydberg atom interactions, and their possible use in quantum computing or single photon applications.

0.2 Acknowledgements

I want to begin by thanking my advisor Thad Walker. It has been wonderful to work with someone who has such a fabulous enthusiasm for physics and excitement about our experiment. I have learned a great deal from him, and will always owe him my great thanks.

In addition, I have had several helpful conversations with Mark Saffman and Deniz Yavuz, who have both been very willing to share their knowledge and insight into our experiment. It has been much appreciated and essential to our continued success.

Jason Day, my colleague for most of my time in Thadlab, has made great contributions to the work contained in this thesis. I appreciate both his physics insight and his friendship. In addition, I have had the privilege of sharing thoughts and days with many great members of the atom trainers and quantum computing, including Jennifer Sebby-Strabley, Todd Johnson, Erich Urban, Brian Lancor, Thomas Henage, Bob Wyllie, and Lisa Hardy. I have greatly benefitted from their discussions and friendships.

There is more to life than physics, and I am very grateful for the the many friends in the graduate program and beyond who have helped me to remember that. In particular, Matt Miller and Matt Palotti have been wonderful friends, making the days great fun with frisbee, jokes, and games.

I owe a great deal of thanks to my wife Susie for her patience and encouragement. She made many sacrifices to help me along the way, and I love her more than I could say. Thank you for being wonderful, and for always making the days joyful, even when stress abounded.

Finally, and most importantly, I would like to thank God. He has blessed me with many wonderful gifts, and the ability to accomplish much. All this though is secondary to His love and presence, for which I am most thankful.

CONTENTS

LIST OF FIGURES

LIST OF TABLES

1. INTRODUCTION

1.1 Background and Motivation

The study of Rydberg atoms in cold atomic clouds is one of the most exciting areas in atomic physics today. Their unique properties, especially their extremely large interaction strengths and long lifetimes, make Rydberg atoms an intriguing area for a number of applications. While Rydberg atoms were first detected in the Balmer series of Hydrogen in 1885, recent advances in laser technology have provided more efficient means for their production and control. Especially since the first generation of Rydberg atoms in a cold atomic sample in 1998 [Anderson *et al.*, 1998], interest in and pursuit of Rydberg atom physics has increased dramatically. The primary results of this dissertation are the extension of the base of knowledge regarding the properties of ultracold Rydberg atoms and the development of a new tool for use in their manipulation: the stimulated emission probe.

Since the first production of ultracold Rydberg atoms, many groups have been investigating their properties and interactions. For instance, understanding Rydberg atom dynamics has led many groups to investigate the onset of ionization and the formation of cold plasmas [Li *et al.*, 2005] [Walz-Flannigan *et al.*, 2004], leading to a better understanding of the interaction properties. The existence of novel ultralong range Rydberg molecular states was first proposed in 2000 [Greene *et al.*, 2000] and recently observed [Bendkowsky *et al.*, 2009]. In addition to the importance of long

range interactions, the small energy differences between Rydberg levels also result in interesting phenomenon. The recent results of [Wang *et al.*, 2007] and the results of the experiments in this dissertation indicate that superradiance plays an important role in the dynamics of Rydberg clouds, including the enhancement of atom-atom interactions and the speed-up of ionization.

Samples of Rydberg atoms have many possible applications, but perhaps the most intriguing is the development of successful strategies for quantum computation and quantum manipulation [Jaksch *et al.*, 2000]. While the details of quantum computation can be found elsewhere [Nielsen *et al.*, 2000], its appeal lies in the ability to make use of quantum bits ("qubits"), allowing better modeling of quantum mechanical systems and improvement in computation through several new algorithms [Grover, 1996] [Shor, 1996]. The proposal of [Lukin *et al.*, 2001] uses the strong dipole interaction of Rydberg atoms to accomplish single atom control for quantum computation. If the atom-atom dipole interactions have energies larger than the transition linewidth, excitation of more than one atom will be prohibited, a feature called the 'dipole blockade'. Towards this goal, a number of groups have demonstrated the related phenomenon of suppression of Rydberg excitation in large atomic clouds [Singer *et al.*, 2004] [Tong *et al.*, 2004] [Cubel Liebisch *et al.*, 2005] [Vogt *et al.*, 2006] [Vogt *et al.*, 2007] [Heidemann *et al.*, 2007], and recently this concept has been successfully implemented to blockade coherent excitation of single atom qubits [Urban *et al.*, 2009] [Gaëtan *et al.*, 2009].

In addition to blockade between two isolated atoms, coherent control between ground and Rydberg atoms has begun to be realized, using isolated atoms [Johnson *et al.*, 2008], atomic clouds [Reetz-Lamour *et al.*, 2008] [Weatherill, 2008], and Bose-Einstein Condensates [Heidemann *et al.*, 2008]. An intriguing result of dipole blockade in samples of spatially confined cold atoms [Sebby-Strabley, 2004] is collec-

tive excitation, which has recently been observed [Heidemann *et al.*, 2007].

The properties of dipole blockade raise further interest when combined with four-wave mixing [Bloembergen, 1996]. If the proper phase-matching is accomplished, photons are emitted into a diffraction-limited solid angle. Thus, the dipole blockade between ultracold Rydberg atoms combined with a phase-matched geometry could be used to produce a source of single photons on demand with extremely high collection efficiency [Saffman and Walker, 2002].

The experiments described in this dissertation represent significant advances in the field. We have introduced a novel method for detecting and studying the dynamics of Rydberg atoms in the stimulated emission probe [Day, 2008] and used it to generate phase-matched emission [Brekke *et al.*, 2008]. In addition, the enhanced atom-atom interactions resulting from resonant microwave coupling between nearby Rydberg states have been observed in a pulsed excitation scheme. Combining the four-wave mixing scheme of our stimulated emission probe with these strong atom-atom interactions would provide an excellent system for the generation of a single photon source.

1.2 Summary of Thesis

This dissertation discusses experiments involving the exploration and manipulation of ultracold Rydberg atoms excited from a Magneto-Optical Trap (MOT). The primary novel feature which was developed for the work in this dissertation is a stimulated emission probe of the Rydberg state. This probe has been applied to perform three major experiments: the study of Rydberg atom dynamics leading to the realization of superradiance, the generation and optimization of four-wave mixing resulting in photon emission into a preferential direction, and the investigation of microwave enhanced atom-atom interactions in a small volume.

The beginning of the dissertation is dedicated to a summary of the apparatus used in generating and observing ultracold Rydberg atoms. We trap and cool 1 x 10^8 atoms in a standard MOT with a $\sim$1 mm radius giving a density of 2 x 10^{10} atoms/cm^3. We exploit a two-photon transition to excite atoms in the MOT into the Rydberg state, avoiding intermediate population and allowing for the narrow transition linewidths necessary for effective dipole blockade. Using this two-photon excitation we can access $|s\rangle$ or $|d\rangle$ Rydberg levels from n=28 to 58, encompassing a wide range of atom-atom interaction strengths. We have demonstrated two effective means of Rydberg detection. In the first the measured loss rate from the MOT is compared to the loss rate without Rydberg population. This technique gives an excellent idea of the relative Rydberg population, but not an exact calibration of the number of Rydberg atoms without further information on the loss rate per Rydberg atom. The second method detects decay photons from the $6P_{3/2}$ state. Information about the exact number of atoms can then be extracted from the excitation rate and detection efficiency of the system. The number of Rydberg atoms created in our apparatus can be varied tremendously, from ~ 10 to $\sim 10^4$.

Chapter 3 of this dissertation describes the experiments performed to obtain an understanding of Rydberg atom dynamics in the limit of weak excitation. Variation of the frequency of the excitation lasers allows for a measurement of the linewidth of the Rydberg transition. This width is consistently larger than expected, and a number of possible causes are explored and discussed. These measurements also give us a good understanding of the loss rate following Rydberg excitation, revealing that only $\sim$1:500 of the excited atoms is lost from the MOT.

The focus of Chapter 3 is the introduction of our novel means of exploring Rydberg populations, the stimulated emission probe. As opposed to field ionization techniques, the intensity of this probe can be varied to control the rate at which atoms are re-

moved from the Rydberg state, giving an important new means of optical detection of Rydberg atoms. This is used to measure the rate that atoms leave the Rydberg state, revealing that atoms leave on a timescale faster than spontaneous emission or black-body radiation would allow. The exact value depends on the Rydberg level used, but is typically $\sim 7\mu$s. In order to better understand why atoms are leaving the Rydberg state at this fast rate, we introduce a model of the population dynamics. This model allows us to obtain an experimental measurement of the transfer rate out of the Rydberg state, as well as the total rate of loss from the MOT per atom. The MOT loss rate is in agreement with the expected loss from black-body ionization. The transfer rate out of the Rydberg state, however, suggests a yet unexplored mechanism causing rapid population transfer.

In Chapter 4 I explore the likely mechanism for the fast transfer rate, superradiance. It begins with a brief introduction to the principles of superradiant transfer, and the important distinction of emission proportional to N^2 when the atoms are confined to a size smaller than the wavelength of emitted light. These principles are implemented in a simulation of superradiance developed to duplicate the conditions of our experiment. Due to the abundance of decay channels from the Rydberg state, this simulation is expanded until the addition of Rydberg states does not affect the outcome. The accuracy of the simulation was verified by comparison to known features of superradiance and previous experimental observations. The expected transfer rate can be extracted from the simulation, typically giving values of order $10^5\ s^{-1}$, in agreement with the experimental observations of Chapter 3. Our work is the first to emphasize the importance of superradiance for understanding the features of Rydberg gas dynamics.

Chapter 5 of this dissertation discusses an important means of attaining high detection efficiency for a single photon source. When the excitation and stimulated emission lasers are oriented in a proper phase-matched geometry, the Rydberg atoms emit into a

diffraction limited direction in a process known as four-wave mixing. To our knowledge, this is the first work to demonstrate four-wave mixing through a Rydberg state, and this represents one of the primary goals of this dissertation. We have verified our four-wave mixing in three ways: by measuring the spatial profile of the emitted photons, the dependence of the output beam on the laser geometry, and the dependence of the percent of the total light emitted in the phase-matched direction versus the number of atoms in the MOT. The process was optimized by detuning the excitation lasers from the Rydberg resonance, and up to 50% of the total emitted light was contained in a diffraction limited beam.

In order to pursue the study of atom-atom interactions in our system, it was necessary to develop a number of new experimental techniques. Chapter 6 describes the methods that were used in these experiments, and represents a "toolbox" that will be drawn from to accomplish the future investigations. The first technique discussed is our method for using microwaves to couple nearby Rydberg states, which can be verified through the observation of the Autler-Townes splitting. Next, I discuss our method for limiting the volume using perpindicular excitation beams, including spatial selection using the large ac Stark shift resulting. Finally, I will explain the method of pulsed Rydberg excitation, allowing the determination of the number of Rydberg atoms and the excitation rate. This pulsed scheme also revealed the importance of ionization, motivating the use of $|s\rangle$ states rather than $|d\rangle$ states. These techniques have been presented separately to allow the reader an uninterrupted discussion of the important results discussed in Chapters 7 and 8.

A driving motivation for the study of Rydberg atoms is their very strong atom-atom interactions, the origin of which is discussed in Chapter 7. These interactions result in a complicated dependence for the number of Rydberg atoms produced. Here I derive the expected scaling of the Rydberg excitation to examine the regime where

these interactions first become significant. This enables not only a qualitative understanding of the expected behavior, but also a quantitative measure of the interaction strength. In addition, two particular cases of atom-atom interactions will be examined: The van der Waals interaction and the first order dipole-dipole interaction resulting from resonant microwave coupling. Microwave coupling can significantly increase the interaction strength, making this an attractive alternative to relying simply on the van der Waals interaction to achieve blockade.

Evidence for the suppression of excitation is examined in Chapter 8 for both the van der Waals and resonant microwave cases. By monitoring the number of Rydberg atoms created while varying the density and excitation rate, we observe a deviation from linear dependence in the case of resonant microwave coupling. This is an indication that the increased atom-atom interactions are suppressing excitation. In addition, we can analyze the onset of suppression using the scaling developed in Chapter 7, which shows excellent agreement. The fit is used to obtain a value for the interaction strength of $C_3\beta$ = 270±120 MHz μm^3 and 300±120 MHz μm^3 for the density and intensity dependence, respectively. While the uncertainty is quite high, these values are in agreement with the theoretical prediction, suggesting a good understanding of the system.

The dissertation concludes in Chapter 9 with a summary of the work presented here and a discussion of its importance in the field. The research conducted in this dissertation is ongoing, with several planned improvements and exciting future pursuits.

2. EXCITATION APPARATUS

2.1 Introduction

In this chapter I will discuss the means by which we create and observe Rydberg atoms. One of the goals in the development of this system was to develop an excitation scheme whose parameters can be easily adjusted to investigate different regimes. Thus, we have created a system where the volume of excitation, density of Rydberg atoms, and interaction strength between atoms can be controlled independently.

I will begin with a very brief description of our source of ultracold atoms: the Magneto-Optical Trap (MOT). Since MOTs have become commonplace in today's atomic physics experiments and many excellent references exist on their fundamental properties [Metcalf and van der Straten, 1999], the physics behind a MOT will not be discussed here. Instead, only the properties of our MOT which are important to our experiments will be discussed. Typically we trap and cool 1 x 10^8 atoms with a $\sim$1 mm radius giving a density of 2 x 10^{10} atoms/cm^3.

Next I will discuss the lasers used in creating and manipulating Rydberg atoms. For our experiments we use three lasers: two for the excitation and a stimulated-emission probe. The first step of excitation from the ground 5s state detuned from the 5p state at 780 nm is accomplished with a commercial amplified diode system and can deliver up to 18 mW to the atomic cloud. The second step from 5p to the Rydberg state is generated by frequency doubling a 960 nm diode, giving up to 10 mW at the atomic

cloud, and is tuneable from 479-483 nm. Finally, the stimulated-emission laser transfers the atoms to the 6p state. It is a commercial diode system, giving up to 100 mW of light at the atoms, and is tuneable from 1013 to 1027 nm.

The effective control of the atoms requires precise frequency stabilization. Thus, I will next discuss our means of stabilizing both the excitation lasers and stimulated emission laser. Using a combination of saturated absorption and a novel technique of dual-cavity stabilization we are able to stabilize all lasers to better than 1 MHz.

Finally, I will discuss our means of Rydberg atom detection. We employ two complimentary techniques, which combine to give excellent understanding of the system. First, we observe the loss of atoms from the MOT, which indicates an additional loss undergone by atoms in the Rydberg state. In addition, we also observe decay fluorescence from the 6p state, which is present from both spontaneous and stimulated emission from the Rydberg state. The primary components of this optical train are a dichroic mirror, several frequency filters, and lenses which image the atom cloud onto a sensitive photo-multiplier tube.

2.2 Magneto-Optical Trap

The MOT is an effective tool for a variety of atomic applications. We use it here as a source of ultracold atoms to be excited to the Rydberg state. Atoms are first cooled and spatially confined to a volume of 1 mm in radius using standard MOT technology. From there they can be transferred to the Rydberg state using the excitation lasers.

The primary components of our MOT include a vacuum chamber, primary trapping and cooling laser, hyperfine repumping laser, and the coils necessary for generation of magnetic fields. An energy level diagram of the Rubidium 5s and 5p states is given in Figure 2.1 as an aid for understanding the trapping process.

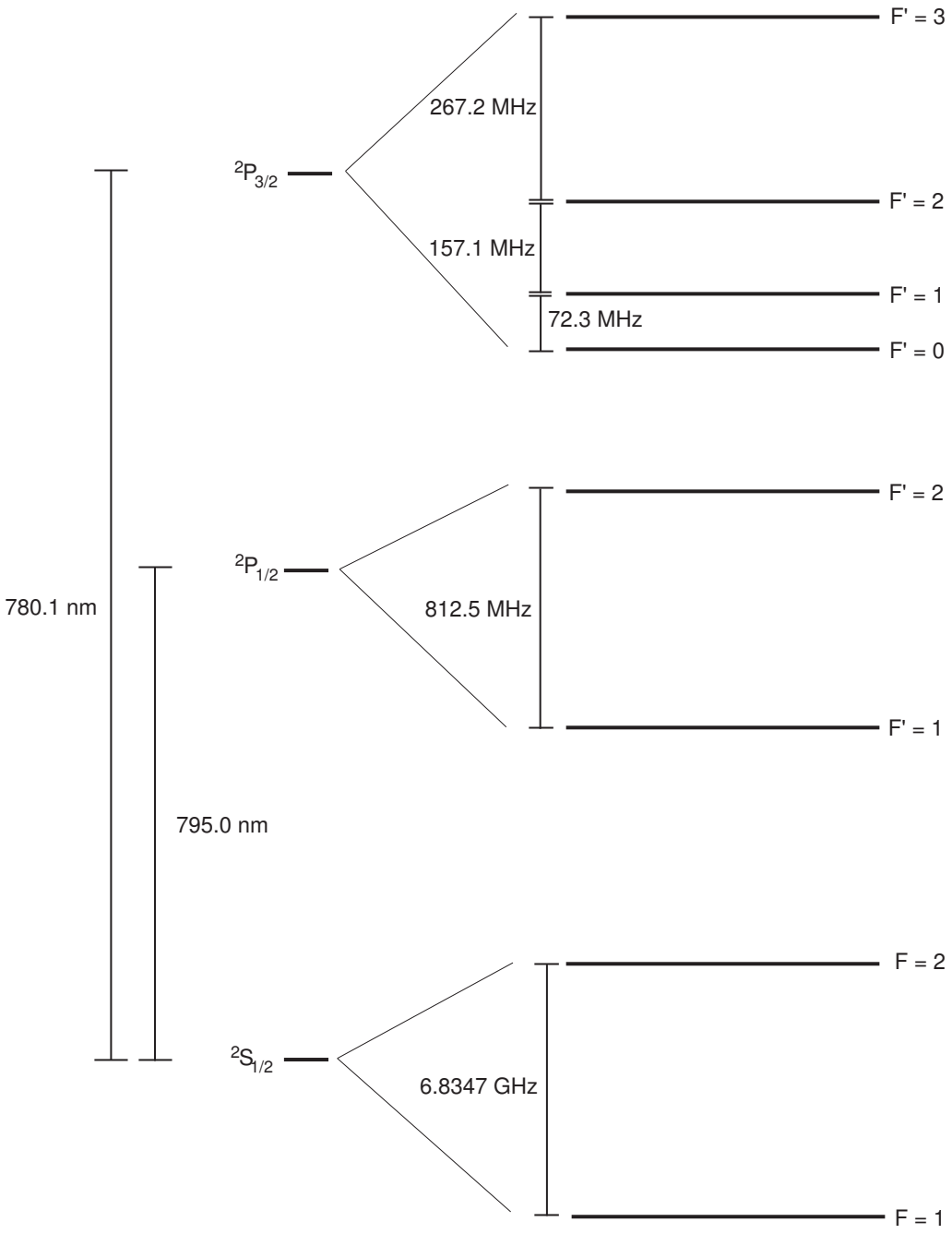

Fig. 2.1: 5s and 5p states of Rubidium 87.

The trapping light is provided by a Titanium:Sapphire laser pumped by a Coherent Innova-310 Argon Ion Laser, and is tuned 15 MHz below the cycling transition, $^2S_{1/2}$ $F = 2$ to $^2P_{3/2}$ $F' = 3$. In addition, a homebuilt diode laser is used to"repump" atoms from $^2S_{1/2}$ $F = 1$ to $^2P_{3/2}$ $F' = 2$ if they have undergone an infrequent Raman transition into the F = 1 ground state. The details of this trap, including these lasers, the ultra-high vacuum system, and the magnetic field coils, are well described elsewhere [Sebby-Strabley, 2004].

These components are necessary to achieve a "bright" MOT, with all atoms in the F = 2 ground state. While this is often all that is needed, creating a "dark" MOT with atoms in the F = 1 state has several benefits. As a result of radiation pressure and multiple photon scattering [Walker *et al.*, 1990] there is a fundamental density limit to a "bright" MOT. By imaging an opaque object onto the center of the MOT and employing a depumping laser which removes atoms from the F = 2 to F = 1 state the density can be increased [Ketterle *et al.*, 1993], though this increase is not significant in our experiment.

The main reason "dark" MOT is used in our experiment is to allow access to a different ground state hyperfine level. For the purposes of Rydberg excitation, this can be important to prevent detuned excitation resulting from the trapping laser as opposed to the first excitation laser. Accessing the F = 1 atoms also provides a wide range of possible detunings from the intermediate state. As a result, we gained control over the magnitude and sign of the AC stark shift from the first excitation beam, the importance of which will be seen more fully in Chapter 6.

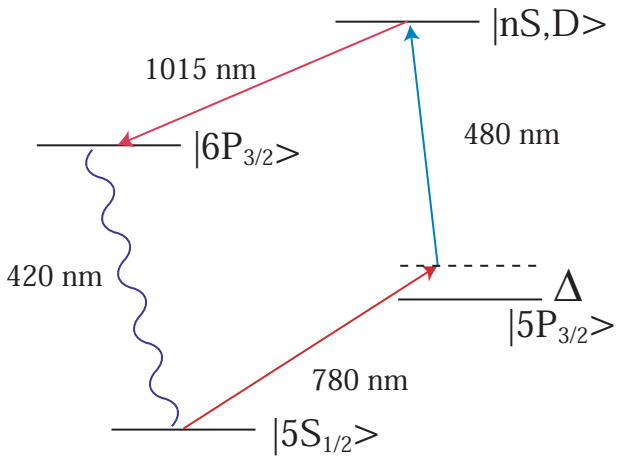

Fig. 2.2: Relevant energy levels for the production and observation of ultracold Rydberg atoms.

2.3 Rydberg Lasers

In this section I will provide an overview of the lasers used for the production of Rydberg atoms from the MOT and their manipulation. A diagram showing the relevant energy levels is shown in Figure 2.2. It is possible to create Rydberg atoms using the atoms in the $5P_{3/2}$ $F' = 3$ excited state populated by the trapping laser, and this has been observed in our lab. However, this process populates the intermediate state, and its decay back to the ground state effectively broadens the Rydberg transition and contributes decoherence to the system. In order to avoid this, we use a two-photon transition which is detuned from the intermediate state. By using this excitation scheme, it is possible to have a narrow transition linewidth and a coherent process.

2.3.1 780 nm Laser

The first step in this two-photon excitation is done with a Toptica TA-100 external cavity diode laser and tapered amplifier system at 780 nm. The Toptica is frequency stabilized using saturated absorption spectroscopy and locked to the $5s_{1/2}, F = 2$ to $5p_{3/2}, F' = 3$ transition. In order to detune from the $F' = 3$ state, a high-frequency acoustic-optical modulator (AOM) is used to shift the frequency up 470 MHz. The efficiency of the AOM is 17%, resulting in 20 mW of light being delivered to the atoms.

We have two possible means of delivering this light to the atoms. The first is useful for exciting the maximum number of Rydberg atoms, and is oriented in a geometry to allow four-wave mixing (as described in Chapter 5). Thus it is used for the majority of the experiments described in this dissertation. In this orientation, the laser has an intensity profile that has a $1/e^2$ Gaussian radius (henceforth referred to as the beamwaist) of 4 mm. The beamwaist is larger than the spatial extent of the MOT to allow uniform excitation and avoid spatially dependent AC stark shifts. Loss of power is not a concern because of the high Rabi frequency associated with this transition. Typically when using this orientation, we excite from the $F = 2$ ground state, so the first step is blue detuned 470 MHz.

As an alternative setup, we can also input this 780 nm beam perpendicular to the second excitation beam. In this case the laser can be focused to a beamwaist of 11 μm at the atomic cloud. This orientation allows for the selection of a very small volume for excitation, and also results in a very large ac Stark shift of the ground energy level. This will be an important point when attempting to attain maximum containment of the atoms as discussed in Chapter 8. Both of these setups can be seen in Figure 2.3.

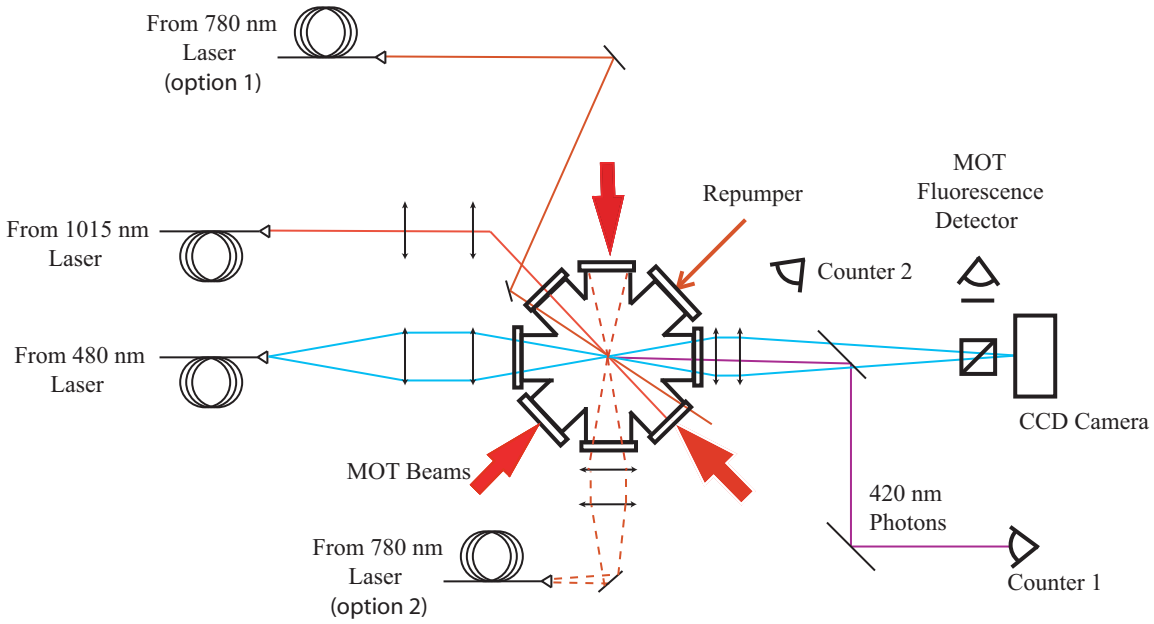

Fig. 2.3: Complete experimental setup for the creation of ultracold Rydberg atoms. The orientation of all lasers can be seen, including the two alternate locations for the first excitation step at 780 nm .

2.3.2 480 nm Laser

The second step in the two-photon process is done with a home built frequency doubled diode laser system that operates from 479 to 483 nm, often referred to as the blue laser. With this tuning range we can populate Rydberg states from n=28 to n=58. The blue light is achieved by frequency doubling an amplified 960 nm Toptica diode in a homebuilt casing. The diode produces 30 mW of 960 nm light. After going through an optical isolator, a small part of this goes into a frequency stabilized cavity locking system, which will be fully described in Section 2.4. The rest goes into an Eagleyard tapered amplifier. This amplifier follows the exact frequency spectrum of the seeded 960 nm light, giving good (<1 MHz) linewidth. However, the spatial mode is of lower quality, with $M^2 > 1.5$. Using this amplifier we are able to achieve 13.5 dB of amplification, resulting in 450 mW of output light at 960 nm.

This 960 nm light is the input for a bow-tie cavity designed to optimize frequency doubling. This cavity contains a periodically-poled potassium titanyl-phosphate (PPKTP) crystal purchased from Raicol. When optimally focused and aligned, 10 mW of 480 nm light exits the cavity, with 6 mW typically reaching the atomic cloud. The setup for both the amplified master laser and the doubling cavity can be seen in Figure 2.4.

Since the full details of the doubling system have been well described elsewhere [Day, 2008], only the basic concepts will be given here. Frequency doubling in a crystal arises when asymmetries in the crystal lattice make the crystal birefringent. This results in a nonlinearity of the response of the crystal to external fields that does not exist for symmetric crystals. The induced polarization field in the crystal will have frequency components at both the fundamental and second harmonic frequencies of the driving field. The power at the second harmonic frequency produced by a plane

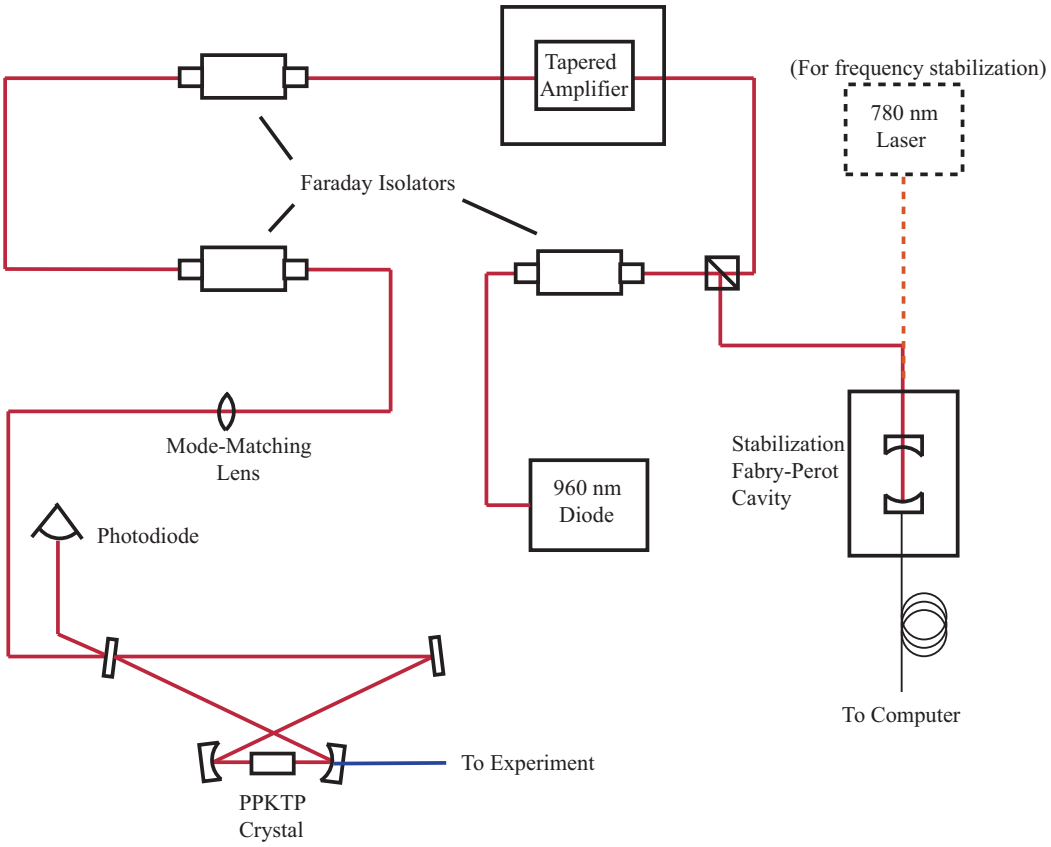

Fig. 2.4: Diagram of the major components of the 480 nm laser. The 960 nm master diode pumps a tapered amplifier and has a portion used for frequency stabilzation. The amplifier output is frequency doubled in a bow-tie cavity.

wave at the pump frequency passing through an optical crystal of length l is shown in Equation 2.1. Here, $P_{2\omega}$ is the power at the harmonic frequency, P_{ω} the power at the fundamental frequency ω, d_{NL} the nonlinear coefficient of the crystal, w the beamwaist, and n the index of refraction at the pump frequency.

$$P_{2\omega} = P_{\omega}^2 \frac{2\omega^2 d_{NL}^2 l^2}{\pi \epsilon_0 c^3 w^2 n^3} \mathrm{sinc}^2 \left(\frac{\Delta k l}{2} \right), \tag{2.1}$$

The sinc function is maximized when $\Delta k = 0$, which is known as the phase-matching condition. Effectively, this means that the index of refraction must be equal for the fundamental and harmonic frequency so the waves will travel in phase with each other and frequency doubling can continue. The index of refraction in the PPKTP crystal varies with temperature, and this variation is dependent on the wavelength involved. Thus we achieve the phase-matching condition by controlling the temperature of our crystal. This in fact sets the limit on what Rydberg levels can be accessed, as extreme temperatures risk damage of the anti-reflection coating on the crystal or formation of condensation. More detailed information about frequency doubling theory can be found in standard textbooks on nonlinear optics [Yariv, 1971].

The optical train for the blue laser entering the atom cloud is shown in Figure 2.5. The system is designed to both allow for a very tight focus of 12 μm and to easily alternate different configurations. The train is built in a Thorlabs cage system, providing excellent stability and control. After exiting the fiber with a waist of 3 μm, the divergence is reduced by a Thorlabs C240TM-A asphere with a focal length of 8.0 mm. In order to attain minimal beamwaist at the atoms, the laser not collimated by this lens, but instead continues to expand to a beamwaist of 6.2 mm, where it is then collimated using a Thorlabs AC508-400-A achromatic doublet. After an arbitrary distance, an identical AC508-400-A then focuses the laser to a beamwaist of 12 μm at

the atoms. This allows for small excitation volume and high Rabi frequencies.

As an alternative to a small focused beamwaist at the atoms, we have two methods of exciting the entire atomic cloud. The easiest to switch to from the focused configuration requires simply intentionally moving the last AC508-400-A achromatic doublet so that the atoms are not at the focus of the beam, but rather in a divergent portion where all of the atoms are illuminated. Since this lens is positioned on a translation stage within the cage system, it is easily adjusted to either position. As an alternative to this scheme, we can also remove both doublet lenses, and adjust the achromat to collimate the laser beam exiting the fiber, resulting in a beamwaist of 575 μm. This also allows excitation of all atoms, but the collimated beam reduces the distribution of k-vectors in the beam. As we will see in chapter 5, this is an important consideration for four-wave mixing.

2.3.3 Stimulated Emission Probe

The final laser used in the manipulation of the Rydberg atoms is a 1015 nm laser, which is often referred to as the stimulated emission probe. The Sacher Tiger laser used is tuneable from 1013 to 1027 nm, and is able to access all of the Rydberg levels we create. This laser transfers atoms from the Rydberg state to the $6P_{3/2}$ state, enabling control of the rate at which atoms are removed from the Rydberg state. The Sacher laser outputs 300 mW of light, which is transported in three different directions after isolation. A very small amount is used to measure the laser frequency in a wavemeter, some is used for laser stabilization, and the rest is fiber coupled to the experiment. The full setup is shown in Figure 2.6. Using this setup up to 90 mW of 1015 nm light can be delivered to the atoms. Just like the situation for the 960 nm light, there are no convenient transitions for saturated absorption locking of the 1015 nm laser, and so again a more complex scheme is necessary. This is fully described in Section 2.4.

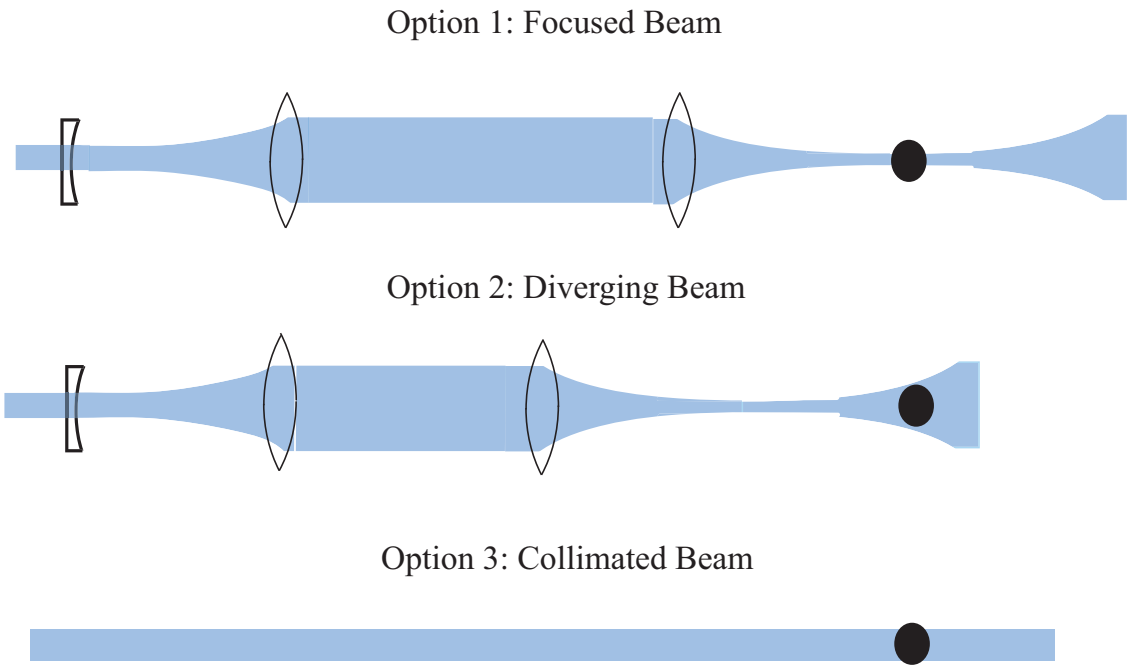

Fig. 2.5: This figure shows the three options for the optical train of the 480 nm or 1015 nm laser. The position of the focusing lens can be varied to either have the focus at the atoms or have all of the atoms within a diverging beam. In addition, all lenses can be removed to have a simple collimated beam. The 480 nm laser train does not have the initial concave lens shown, and instead the collimation lens can be positioned to allow beam divergence.

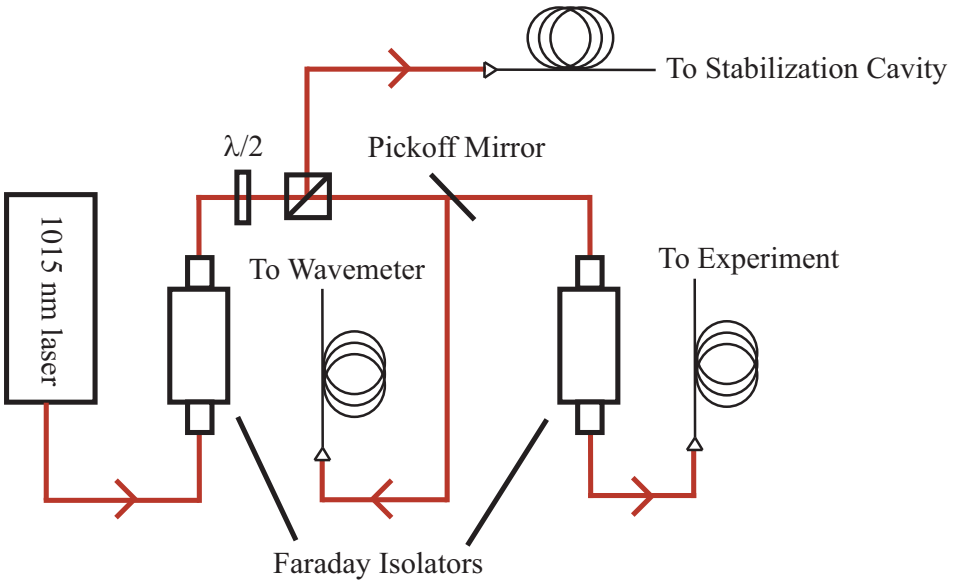

Fig. 2.6: Diagram of the major components of the 1015 nm laser. Light from the diode is diverted into three beams for locking, wavelength measurement, and the experiment. The laser is locked to a Fabry-Perot cavity which is in turn locked to the 780 nm laser.

The optical train for the stimulated emission probe is nearly identical to that of the blue laser seen in Fig. 2.5. The main difference is that in this case the laser beam is collimated after exiting the fiber in all cases by an A397TM-B f=11 mm asphere to a beamwaist of 825 μm. This adaptation to the scheme allows for faster and easier transition between the focused beam and the collimated beam. In this case a Thorlabs ACN254-040-B f=-40 mm lens causes the beam to diverge to a large waist. After this, f=400 mm achromats are again used to collimate and focus the beam, resulting in a focused beamwaist of 13 μm. Similar to the 480 nm light, this beamwaist can also be positioned to allow illumination of the entire atomic cloud. For the stimulated emission probe, almost all experiments to date have been done with a collimated beam. As the excitation volume can be controlled using the other two lasers, and this laser has more power than necessary, there is no need to bring it to a focus for most of our applications.

2.4 Laser Stabilization

Controlling the frequency of the lasers used to create and manipulate the Rydberg atoms is essential to understanding the important features of Rydberg atoms. Much of the data that will be discussed in this dissertation requires slowly scanning one of the Rydberg lasers across resonance. In order for this data to be meaningful, all laser frequencies must remain stable during the length of a scan, and we must have a controlled way of adjusting the laser frequencies. In addition, the data collected in Chapter 8 requires averaging the signal over long periods of time, making it essential to have a system without any laser frequency drift.

In most atomic experiments, laser frequency stabilization is accomplished by using Doppler-free FM-spectroscopy and saturated absorption. This technique is well known and used in a variety of experiments, with a full description given in [Newell, 2003].

While this technique is very powerful, it relies upon having a ground state transition near the desired laser frequency. As a result, it is a very convenient technique for the trapping or repumping lasers as well as the first step in Rydberg excitation. However, the frequencies of light needed for the second step in Rydberg excitation and the stimulated emission probe are not conveniently located near transitions, and this technique cannot be used. Recent work by [Mohapatra *et al.*, 2007] has shown that Electromagnetically-Induced Transparency (EIT) in room-temperature Rydberg atoms could provide a convenient frequency standard, but this has not been pursued by our lab.

Another alternative to a saturated absorption locking scheme that is available at any frequency is locking to a temperature controlled Fabry-Perot cavity. When the length of the cavity is a half-integer multiple of the wavelength of the incident laser light, the light is transmitted through the cavity and detected by a photodiode. Then the laser is locked to stabilize the transmission through the cavity. In fact, this technique was originally used to stabilize the lasers used in this experiment. However, problems arise due to drifts over time in the temperature of the cavity or the pressure inside, which change the length of the cavity or the index of refraction inside. Either of these can change the frequency by a few MHz. Even with temperature control of the cavity and a pressure sealed box, these drifts could not be minimized to better than a MHz per minute. As a result, further development was required to address this problem.

Our current scheme uses both the ideas of an atomic transition as a completely stable frequency reference and the frequency flexibility of a Fabry-Perot cavity, similar to [Bohlouli-Zanjani *et al.*, 2006]. Instead of relying on having a passively stable Fabry-Perot cavity that will maintain a constant frequency reference, we actively feed back to the cavity. This is accomplished by putting a 780 nm laser (that is already stabilized by a saturated absorption setup) into the cavity as a "control" laser. The

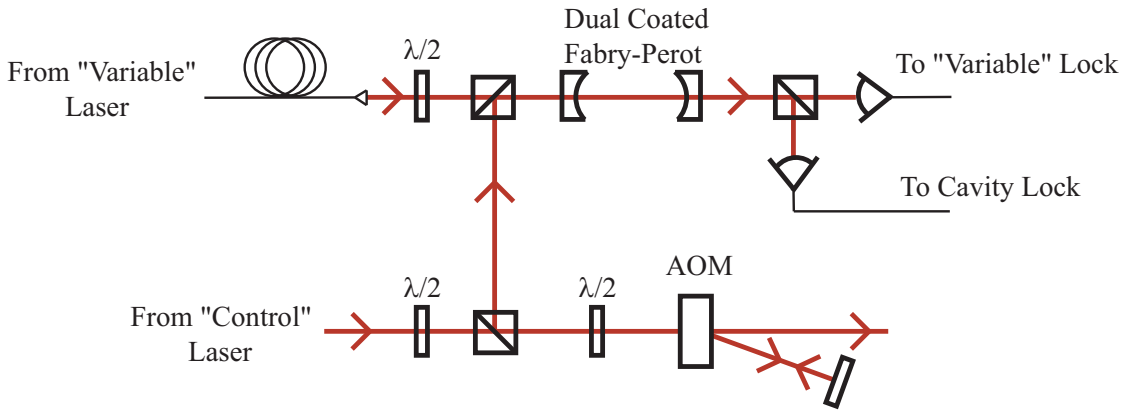

Fig. 2.7: Diagram showing the dual laser locking scheme. The cavity is stabilized to a 780 nm "control" laser, and the 960 or 1015 nm "variable" is then stabilized to the cavity.

cavity piezo undergoes feedback to keep the 780 nm light resonant with the cavity, completely stabilizing the cavity as a frequency reference. At this point, either the 960 nm or 1015 nm light can be used as an additional "variable" laser input to the cavity, with its polarization orthogonal to the "control" laser so it can be seperated by a polarizing beamsplitter cube. Feedback to the piezo of the "variable" laser then optimizes the transmission through the cavity, stabilizing this laser to the cavity. The complete scheme of locking the cavity to a stable "control" laser, and then locking the "variable" laser to the cavity is seen in Figure 2.7. Since both the blue laser and stimulated emission probe must be controlled independently, two identical schemes were constructed using this technique.

There are several complications to this scheme which must be overcome when putting it into practice. Most of these complexities revolve around the properties of a Fabry-Perot cavity, which will only be described briefly here. The details can be found in any standard textbook on lasers and cavities, such as [Svelto, 1998]. For our purposes it is sufficient to see that the full width at half maximum (FWHM) for the transmission peak will limit the precision of the lock. The quality of a cavity in terms

of the distance between transmission peaks (free spectral range (FSR)) compared to their FWHM is defined as the finesse of the cavity, and is dependent on the reflectivity of the mirrors used according to Equation 2.2.

$$F = \frac{\pi\sqrt{R}}{1-R}, \tag{2.2}$$

Thus, in order to achieve a small FWHM for both the "control" and "variable" lasers, the reflectivity must be excellent at both frequencies. This was achieved by ordering special made mirrors from Lambda Optics, with reflectivity of better than 97% for both lasers used in the respective cavities. The FSR was chosen to be its smallest reasonable value at 300 MHz. As a result, we were able to achieve a FWHM of 5.2 MHz for the 960 nm cavity and 6.0 MHz for the 1015 nm cavity.

In addition to having a stable laser, we also need the laser to be tuneable in order to find the resonance or scan the laser across it. The easiest way to adjust the frequency of the "variable" laser is to move a FSR away, resulting in a 300 MHz change in frequency. However, finer adjustment is available due to the fact that different wavelengths are used in the cavity. Eq. 2.3 shows that the needed change in length of the cavity to move a FSR depends upon the wavelength of light used.

$$\Delta L_{FSR} = \frac{\lambda}{2}, \tag{2.3}$$

As a result of this wavelength dependence, moving the cavity length a FSR for the "control" laser will only move a fraction of a FSR for the "variable" laser. This allows us to select a different transmission peak for the "control" laser and have the absolute frequency of the "variable" laser shift by ∼60 MHz due to the difference in wavelength.

This feature allows excellent frequency selection for the "variable" laser, but it is still necessary to fine tune and scan the frequency. A high-frequency AOM can be used

to tune the frequency of a laser over a range of ∼150 MHz, and if double passed the range of tuning can approach 300 MHz. However, most high-frequency AOM's only have ∼20% efficiency per pass, and this greatly reduces the power available. Since power is essential to both the blue laser and stimulated emission probe, we instead put the double pass AOM on the 780 nm "control" laser, and adjust the frequency that the cavity is locked to. A computer control adjusts the frequency shift of the AOM, with which we can continuously scan over 200 MHz. This setup allows the complete independent control of the frequency of both the blue laser and stimulated emission probe while simultaneously providing frequency stability within 1 MHz. A detailed discussion concerning the measurement of these laser linewidths in relation to the observed transition linewidths is found in Chapter 3.

2.5 Rydberg Detection

Having the tools to create and manipulate ultracold Rydberg atoms, I will now discuss the means by which we detect the presence and state of these Rydberg atoms. Our ultimate goals require the manipulation of Rydberg states with optical fields, giving a motivation to develop a system of detection which also relies upon this optical field. As a result, we have developed a novel technique of Rydberg atom detection which has features unavailable in the common detection schemes. Many groups doing Rydberg physics make use of an electric field to ionize the atoms and collect the ions on a micro-channel plate (MCP)[Walz-Flannigan *et al.*, 2004] [Singer *et al.*, 2005]. Most noticeably our technique both allows optical manipulation and eliminates the need for stray electric fields. In addition, the resolution of the system is improved, with the ability to exactly select single Rydberg levels for detection. Finally, we are also able to obtain information about the Rydberg atom dynamics, the importance of which we

will see in Chapter 3.

2.5.1 Loss Rate

The first means by which we detect the presence of Rydberg atoms is by observing the MOT fluorescence. This fluorescence is emitted isotropically from the MOT, and part of it collected onto a photodiode with known efficiency after a bandpass filter to eliminate background. The number of atoms in the MOT is then proportional to the light collected, and has previously been determined [Newell, 2003] to be

$$N_{MOT} = \frac{V}{A} \times \frac{\eta\tau}{(hc/\lambda)p_{ee}\Theta} \times [6.1]\,. \tag{2.4}$$

where, V is the voltage measured by the photodiode from the fluorescence signal of the MOT, A = 9.9×10^6 is the gain of the current-to-voltage converter, $\eta = 2$ W/A is the photodiode detection efficiency at a 780 nm wavelength, $\tau = 27$ ns is the lifetime of the $5P$ state, $p_{ee} = \sim 0.122$ is the typical fraction of the MOT atoms in the excited state, $\Theta = 0.006$ is the fractional solid angle subtended by the photodiode, and the quantity in the [ ] brackets takes transmission losses from three filters into account.

To determine how the presence of Rydberg atoms effects the number of atoms in the MOT, we examine the MOT dynamics, given by

$$\frac{dN}{dt} = L - (\gamma_1 + \gamma_0)N, \tag{2.5}$$

where γ_0 is the standard loss rate from the MOT (due to background collisions and laser induced collisions) and γ_1 is the additional loss rate due to Rydberg population. In steady state, this can be solved for γ_1 to find

$$\gamma_1 = \gamma_0(\frac{N_0}{N} - 1), \tag{2.6}$$

where N_0 is the number of atoms in the MOT without Rydberg atom production. While this loss rate does not give an exact calibration for the number of Rydberg atoms due to

an unknown loss rate per atom in the Rydberg state, it does give an effective measure of the relative Rydberg population. Trap loss is in fact a very sensitive measurement, and it is easy to observe a 0.1 s^{-1} change in the loss rate from the MOT. Thus, even with very low Rydberg excitation rates of 10 s^{-1}, a 1% inelastic or ionization channel can easily be detected.

2.5.2 Decay Photons

As a second means to gain even more information about the presence of Rydberg atoms, we collect decay photons from the intermediate $6p_{3/2}$ state. If a Rydberg atom is produced, it will spontaneously decay to the $6p_{3/2}$ state with a probability that can be determined by the frequencies and matrix elements involved. Thus, the observation of these decay photons at 420 nm is a direct result of Rydberg population.

In order to observe these photons, we use two H7360-01 photon counting modules from Hamamatsu and a multi-channel scalar card from FAST ComTec. A 5 nm band-pass filter is placed in front of the photon counting modules which blocks photons from radiative transitions other than 6p to 5s. While the $6p_{1/2}$ to $5s_{1/2}$ would also be transmitted, this transition is forbidden by selection rules when we excite to $nd_{5/2}$. Having two counters allows the simultaneous observation of decay photons in multiple directions, and the FAST ComTec card has an arrival resolution within 100 ns. The need for these features will be seen in Chapters 5 and 8.

Collecting these decay photons allows for a calibrated measurement of the number of Rydberg atoms if the branching ratio, decay rate, and collection efficiency are all precisely known. The most difficult to measure is the quantum efficiency of the photon counters. To do this, we obtained a source of 420 nm photons using a white light which we passed through a monochrometer calibrated and aligned to transmit 420 nm light. We covered the output slit of the monochrometer with a 5 nm spectral width

420 nm bandpass filter to remove any background light and then recorded the current produced from the incident 420 nm light on a photodiode with a known current per unit power at that wavelength. This allowed us to calculate the flux of 420 nm photons in the beam. By comparing this number to the count rate of the photon counters we determined their quantum efficiencies to be 5.5% and 5.3%. Combining this fact with the known solid angles and transmission of the various optics allowed a determination of the collection efficiency.

Only a small fraction of the Rydberg atoms will decay to the $6P_{3/2}$ state, and only some of these will decay from here to the $5S_{1/2}$ ground state resulting in observable 420 nm photons. To understand the branching ratio we must investigate the various decay rates out of the Rydberg state. Following [Gallagher, 1994], the decay rate $A_{n'l',nl}$ from a Rydberg state $|nl\rangle$ to a lower lying state $|n'l'\rangle$ varies with the average oscillator strength $\overline{f}$ as follows:

$$A_{n'l',nl} = \frac{-2e^2\omega^2_{n'l',nl}}{mc^3}\overline{f}_{n'l',nl}. \tag{2.7}$$

where the average oscillator strength $\overline{f}_{n'l',nl}$ is defined as

$$\overline{f}_{n'l',nl} = \frac{2}{3}\omega_{n'l',nl}\frac{l_>}{2l+1}|\langle n'l'|\, r\, |nl\rangle|^2, \tag{2.8}$$

where $l_>$ is the greater of l and l'. Plugging Equation 2.8 into Equation 2.7 reveals a ω^3 dependence of the decay rate on the frequency of the radiated photon. As a result, transitions to the lowest energy levels will be favored due to their large frequencies. While these transitions will have a smaller value of the matrix element $|\langle n'l'|\, r\, |nl\rangle|^2$, the frequency dependence more than compensates for this reduction, making the ground state highly favored. These matrix elements must be calculated numerically, with the reduced matrix element evaluated as $(\int P_{n'l'} r P_{nl} dr)^2$, as described in Appendix A

To obtain the branching ratio, this decay rate must be compared to the total decay rate from the Rydberg state. The total rate will be $A_{nl} = 1/\tau_{nl}$ where τ_{nl} is the lifetime

of the Rydberg state $|nl\rangle$. The lifetime of state $|nl\rangle$ is given by,

$$\tau_{nl} = \tau_0(n - \delta_{lj})^{\alpha}, \tag{2.9}$$

where n is the principal quantum number, δ_{lj} is the quantum defect of the state $|nlj\rangle$ as calculated by (Li,2003) and (Han,2006), and τ_0 and α are parameters dependent upon atomic species and angular momentum state, as detailed in [Gallagher, 1994]. The branching ratio $b_{n'l'}$ for the radiative transition from the Rydberg state $|nl\rangle$ to $|n'l'\rangle$ is then,

$$b_{n'l'} = \frac{A_{n'l',nl}}{A_{nl}}. \tag{2.10}$$

For most of the Rydberg states produced in this dissertation, the branching ratio is around 0.15 into $6P_{3/2}$. The branching ratio from the $6P_{3/2}$ to $5S_{1/2}$ can be found in a similar way to be 0.31. It is unlikely that population would make multiple transitions into the $6P_{3/2}$ state, as the long-wavelength photons required for multiple transitions are not favored.

Using this information and the count rate (C_6) of 420 nm decay photons we can obtain an estimate of the Rydberg atom number N_r:

$$N_r = \frac{c_6 P}{b_{6P} b_{5S} \eta \frac{\Theta}{4\pi} A_r} \tag{2.11}$$

where η is the detection efficiency including filters and beamsplitters, and $\frac{\Theta}{4\pi}$ is the fractional solid angle.

The situation becomes more complicated as we consider that mechanisms other than spontaneous decay can transfer atoms from the Rydberg state. However, these two methods of Rydberg atom detection serve as an excellent diagnostic of the Rydberg state, especially when combined with the stimulated emission probe, as we will see in Chapter 3.

3. RYDBERG DYNAMICS

3.1 Introduction

In this chapter I will discuss our observations of Rydberg atom dynamics. A great amount of information about the dynamics of Rydberg atoms can be obtained simply by observing the populations after excitation. These observations show the important role of collisional phenomena [Farooqi *et al.*, 2003] [Carroll *et al.*, 2006], including resonant [Afrousheh *et al.*, 2004] [Afrousheh *et al.*, 2006] [Bohlouli-Zanjani *et al.*, 2007] [Vogt *et al.*, 2006] and near-resonant [Li *et al.*, 2005] [Amthor *et al.*, 2007] energy transfer. Since surprisingly fast spontaneous conversion of Rydberg clouds into plasmas at high densities has been observed [Robinson *et al.*, 2000] [Li *et al.*, 2004] [Li *et al.*, 2005] [Walz-Flannigan *et al.*, 2004], there is a large amount of interest in understanding the main processes governing Rydberg dynamics. Our experiments here focus on the novel regime of relatively low Rydberg densities (10^7 /cm^3), with densities several orders of magnitude lower than those studied elsewhere.

I will begin with a brief discussion of the Rydberg states to which we excite. Our method of two-photon excitation gives several possibilities for the final state. The particular characteristics of these states will be discussed, including the rate at which we are able to excite Rydberg atoms. In addition, there will be a brief explanation of the important interactions associated with our choice of state. This will be expanded upon later in Chapter 7.

Varying the frequency of our excitation lasers allows spectroscopic observation of the excitation linewidth of the Rydberg state. These linewidths are consistently larger than expected, which could make successful blockade more difficult. Numerous techniques have been used to verify the linewidth and attempt to examine the causes of broadening. Though these transition linewidths are still not well understood, these experiments have led to a better understanding of the excitation techniques used. These measurements also give excellent insight into the extent of trap loss during Rydberg excitation.

Next I will illustrate how our novel Rydberg detection technique provides new insight into the rate of transfer from the Rydberg state. The common method of Rydberg detection used by other groups (MCP ion detection), is limited to observing the binding energy of the atoms, and it is complicated to extract dynamic information from this process. In contrast, since the intensity in our stimulated emission probe controls the rate of removal from the Rydberg state, it is quite easy to gain information about competing transfer rates in the system. Using this, our measurements indicate that the atoms are leaving the Rydberg state faster than would be expected from spontaneous decay or black-body transfer.

Finally I will discuss a model which we have created to help better understand the system. This model of the Rydberg population dynamics allows us to quantify the rate at which atoms leave the Rydberg state, and compare this to various explanations. We can then use both our experimental data and calculations using this model to make important conclusions about the possible mechanisms affecting the Rydberg state.

3.2 Rydberg Level Properties

Using the lasers and excitation scheme described in Chapter 2 we can effectively excite atoms to s and d Rydberg levels from n=28 to n=58. In order to decide which state

is most beneficial to excite, a number of factors must be considered. Essential to any blockade experiment is a strong atom-atom interaction. In the absence of an external field, the atoms have definite parity, and no permanent dipole moment. In this case the dominant long range interaction is the van der Waals, which normally scales as n^{11}. As a result, a higher principal quantum number makes a great difference in the interaction strenth.

Currently the temperature of the frequency doubling crystal (described in Chapter 2) sets a hard limit on the highest Rydberg state that can be reached. However, even without this, there are several reasons that a lower Rydberg state is desirable. These result from the fact that the matrix element coupling the $5p_{3/2}$ state to the Rydberg state is strongest for the lowest lying states.

To see the importance of this, we will now examine the rate of excitation to the Rydberg state. The coupling between two states is often given in terms of the Rabi frequency, defined by:

$$\epsilon = \frac{-eE_0}{\hbar} \langle e| r |g\rangle , \tag{3.1}$$

which depends critically on the matrix element $\langle e| r |g\rangle$. This is solved by using the Wigner-Eckart theorem to take the angular components into account. The radial component of the matrix element can be solved numerically, either by using quantum defect theory or by generating a pseudo potential that gives the correct energy levels. The full details of how this Rabi frequency is calculated for our Rydberg levels can be found in Appendix B. Since we use a two photon transition to the Rydberg state, the two photon Rabi frequency is:

$$\epsilon_2 = \frac{\epsilon_r \epsilon_b}{\Delta}, \tag{3.2}$$

where ϵ_r and ϵ_b are the single-photon Rabi frequencies for the 780 nm and 480 nm lasers, and Δ is the intermediate state detuning. When the transition linewidth Γ_w is

larger than the excitation Rabi frequency, the effective excitation rate will be reduced [Stenholm, 1984]. The effective excitation rate is then given by

$$R_2 = \frac{\epsilon_2^2}{\Gamma_w}. \tag{3.3}$$

As can be seen, the excitation rate varies as the square of the matrix element, decreasing by an order of magnitude from $|28d\rangle$ to $|58d\rangle$. In fact, this large variation has dual significance for our experiment. First, since we are limited in the amount of power deliverable, the rate of Rydberg atom creation decreases with principal quantum number. In addition to this, the rate at which the Rydberg atoms return to the 6p state is also reduced, inhibiting our ability to detect them. As a result of this fact, many proof of principle experiments or alignments are done at lower principal quantum number due to excellent signal, while experiments requiring strong interactions are done at higher principal quantum number.

It is also necessary to mention at this point that the Rydberg state 43d has very unique properties which often make it of particular interest for excitation. Two atoms at $43d_{5/2} + 43d_{5/2}$ have nearly identical energy to $41p_{3/2} + 45f_{7/2}$, differing only by 6 MHz. As a result of this near degeneracy, near resonant energy transfer leads to $\frac{1}{R^3}$ dipole-dipole interactions in the absence of an external field, instead of relying on $\frac{1}{R^6}$ van der Waals interactions. The fact that excitation to 43d actually results in higher interactions than higher principal quantum levels while still having higher matrix elements makes it an attractive candidate for many experiments. A more detailed discussion of this effect and consideration of several other methods for increasing the interaction strength will be discussed in Chapter 7.

Since we excite through the intermediate $5p_{3/2}$ state, we have several final Rydberg states allowed by dipole selection rules: $ns_{1/2}$, $nd_{3/2}$ and $nd_{5/2}$. Exciting to an s state allows investigation of states where the interatomic forces are weaker, and plasma

formation is significantly slowed due to the limited coupling to nearby states from the s levels [Li *et al.*, 2004]. While this is an interesting check on the importance of these forces, the oscillator strength to the $ns_{1/2}$ state is typically 10 times weaker than that to the $nd_{5/2}$ state, preventing effective excitation at high principal quantum numbers. Similarly, the oscillator strength to the $d_{3/2}$ state is 9 times weaker than the $d_{5/2}$ state, so almost all excitation in the experiments described here is done to the $nd_{5/2}$ state. It is also important to note that for our purposes the hyperfine splitting of the Rydberg state is negligible [Li *et al.*, 2004].

3.3 Linewidth Studies

Using the methods described in Chapter 2, we have both an effective means of observing Rydberg state population and precision control of the frequency of the excitation lasers. This makes it possible to slowly vary the frequency of an excitation laser across the Rydberg resonance, and observe its transition linewidth. Understanding the linewidth of the transition is essential to the eventual use of Rydberg atoms in a dipole blockade. As discussed in Chapter 7, the energy shift caused by the interaction must exceed the linewidth of the transition to effectively limit subsequent excitation. A minimal transition linewidth is then desired to make dipole blockade possible at smaller interaction strengths.

An example of the data taken as the 780 nm beam is scanned across the $28d_{5/2}$ resonance is shown in Figure 3.1. As can be seen, the transition linewidth is quite broad, with 8.4 MHz a typical representation of the linewidths observed. The linewidth of this transition does not show strong dependence on principal quantum number, and in all cases is significantly broader than expected. The natural transition linewidth is 6 kHz, and Doppler broadening would only result in $\sim$200 kHz linewidths. In order to

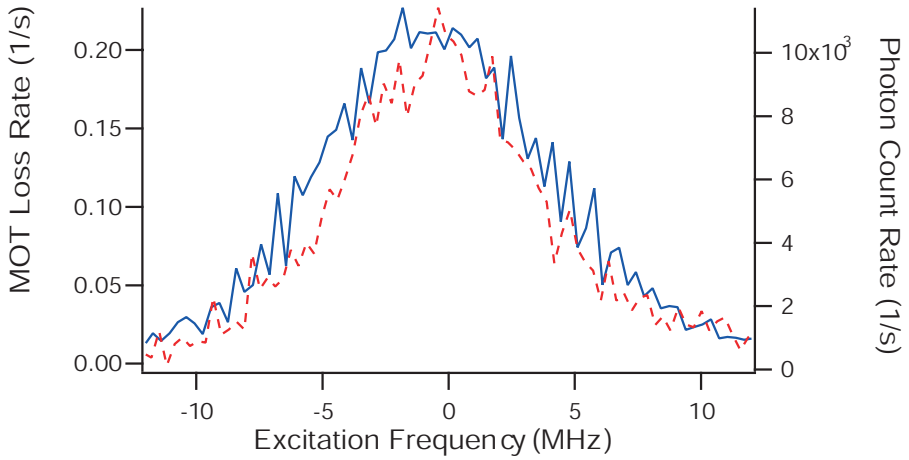

Fig. 3.1: Observed trap loss (dashed line) and photon count rate (solid line) as a function of the 780 nm laser excitation frequency at the 28d Rydberg resonance. The observed linewidth is significantly larger than expected at 8.4 MHz.

determine if this transition linewidth represented a fundamental physical limit it was important to investigate possible sources of broadening.

It is possible that either short-term laser linewidth or frequency locking instabilities would appear as an effective broadening of the transition. The short-term linewidth of external cavity diode lasers is usually excellent, with several hundred kHz being typical for integration times of $\sim \mu$s. However, this can depend on proper cavity alignment, mode selection, and diode quality. In order to measure and characterize the exact linewidth of the lasers used in our experiment, we have used a modified version of the self-homodyne technique [Ludvigsen *et al.*, 1998]. In this scheme frequency fluctuations are measured through the use of a Mach-Zehnder type interferometer, as shown in Figure 3.2. One branch of the interferometer contains a 1 km optical fiber, which results in a $\sim$3 μs delay of the laser light. The other branch contains an acousto-optic modulator that shifts the frequency up by 80 MHz. After combining the two paths onto a photodiode, fluctuations in the phase of the laser field are seen as intensity

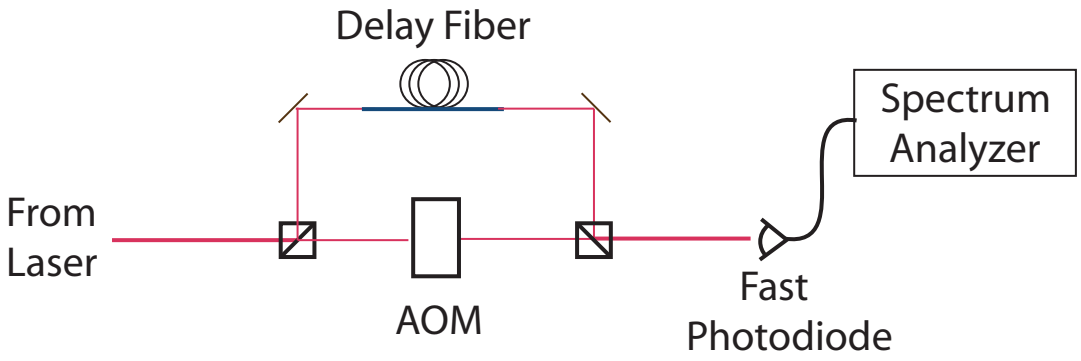

Fig. 3.2: Setup for delayed self-heterodyne interferometer. The laser field is combined with a delayed replica of itself on a fast photodiode. The laser linewidth is deduced from the interference power spectrum.

fluctuations centered around the AOM frequency, giving a means of observing the laser linewidth on the μs timescale.

This technique has been shown to be very successful in measuring the linewidth of our lasers. In fact, the commercial laser originally used in this experiment was determined to have $\sim$5 MHz linewidths, and this helped us identify and replace this laser (960 nm) with the homebuilt system described in Chapter 2. Since that replacement, we have verified that all of our lasers have linewidths less than 1 MHz over a $\sim$ μs timescale. Combined with the various locking mechanisms necessary and taking frequency doubling into account, we calculate that the total width that can be attributed to laser linewidth is 3.2 MHz. This was determined by examining the dither and locking stability in Fabry-Perot cavities.

Another possible contribution to our transition linewidth is due to different Zeeman shifts of the magnetic sublevels in the Rydberg state. Although the MOT is formed at a magnetic field zero, the gradient of the field is 20 Gauss/cm, and would result in the atoms at the edge of the cloud being at magnetic fields of $\sim$1 Gauss. For a $D_{5/2}$ level, this would be enough to produce a transition linewidth approaching that

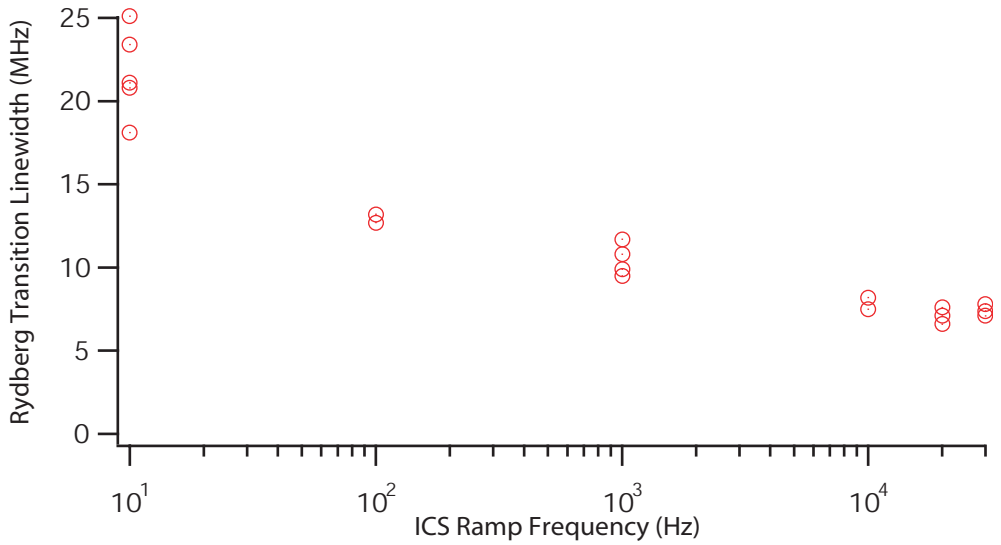

Fig. 3.3: Observed transition linewidth as a function of the rate of laser frequency ramping. The linewidth exceeds 6 MHz even for short timescales.

which we observe. However, this possibility was tested by both reducing and pulsing the confining magnetic field and no reduction in transition linewidth was observed, indicating this is not the limiting factor for the linewidth. Stray electric fields in the chamber could also broaden the transition through Stark shifts. However, these Stark shifts should have a strong dependence on the principal quantum number, resulting in variation of the transition broadening with principal quantum number. Since this is not the case, it appears stray electric fields are not the dominant mechanism either.

As a final investigation technique, we developed a means of determining if fast variation or frequency drift is present in the system. To do this, we applied a frequency ramp to the 780 nm excitation laser, scanning across the resonance in $\sim$100μs. In this case only a few photons are collected as the frequency crosses resonance. However, as the laser scans back and forth across the resonance, the arrival times of these photons are correlated. By triggering on a photon (most likely resulting when the laser is on resonance), and recording subsequent photons, we can measure the transition linewidth

immune to variations on a timescale faster than the frequency ramping period. This technique of Intensity Correlation Spectroscopy (ICS) is described in full elsewhere [Day, 2008], with the results shown in Fig. 3.3. Again, we were unable to observe transition linewidths under 6 MHz.

After all of our experiments, we are still unable to determine the cause of broad transition linewidths. However, several other groups [Teo *et al.*, 2003] [Singer *et al.*, 2004] have seen broad transitions consistent with our results. As a result of the many experimental observations of broad transition linewidths, there has been a recent theoretical simulation of linewidth broadening in Rydberg gases [Sun and Robicheaux, 2008]. This simulation examined two key features which could cause transition broadening: Fluctuations in the atomic spacing, and "diffusion" of the excitation pairs across a sample. Interestingly, it noted that the small number of atom pairs with small separation distances can make a large impact on the transition linewidth. It was calculated that the resulting linewidths could be 20-30 times bigger than those calculated assuming the average interaction strength. For a sample of $|43d\rangle$ atoms with a density of 10^8 /cm^3 the average interaction strength would be $\sim$100 kHz, as discussed in Chapter 7. Due to pair fluctuations, this could result in transition linewidths as high as 3 MHz, a significant contribution to the observed value.

However, there are still several features of the linewidths which are still not well understood. In particular, a noticeable change in the transition linewidth was not observed at different principal quantum numbers (and hence very different interactions strengths). While it is possible that the hypothesis of atomic distance fluctuations may explain some of our results, the full details of our broad transition linewidths are still not well understood. In all likelihood, this broad linewidth implies that even greater interaction strength will be needed for the demonstration of a successful blockade.

3.4 Trap-Loss and Cascade Fluorescence

In addition to gaining information about the transition linewidth, data such as that shown in Figure 3.1 also gives important information about the rate at which atoms are lost from the trap. This rate is deduced from the number of atoms remaining in the MOT as discussed in Section 2.5. In the case shown at $28d_{5/2}$, the loss rate induced by the excitation lasers was 0.2 s^{-1}, a rate much smaller than the 110 s^{-1} excitation rate. From this it is possible to infer that a very small percentage of the atoms excited to the Rydberg state actually leave the trap, in this case only 1:500. This percentage of atoms that leave the trap has been measured for several different Rydberg levels, with the results shown in Table 3.1.

There are several different processes which would result in loss from the trap following Rydberg excitation. Black-body ionization, photoionization by the applied lasers, and sufficiently ineslastic collisions between Rydberg atoms and ground-state atoms would either ionize the atoms or give the atoms sufficient (> 10 K) kinetic energy to leave the trap permanently even if they radiatively return to the ground state. It can be seen from Table 3.1 that the trap-loss probabilities are significantly higher at 43d and 58d as compared to 28d, which could be a result of higher inelastic collisions.

In order to investigate the possibility that inelastic collisions play an important role, we additionally studied the trap loss from 41d and compared it to 43d. As explained in Section 3.2, we expect anomalously large van der Waals interactions at 43d, and hence drastically different collisional properties than at 41d. However, no difference was found in the trap-loss probability between these two states. Combined with the very small fraction of atoms lost from the trap after excitation overall, we conclude that collisions do not cause significant trap loss.

To verify that these conclusions match with theory, we made a simple calculation

State	Fraction Lost	Count Ratio
$28D$	1 : 500	.55
$43D$	1 : 50	.6
$58D$	1 : 50	.6
$30S$	1 : 1000	.5

Tab. 3.1: Both the fraction of excited atoms that are lost from the trap and the ratio of observed to expected cascade counts are shown for various Rydberg levels. The small fraction of atoms lost from the trap following excitation indicate that collisions do not play a major role. However, the small fraction of observed to expected cascade counts indicates that some other transfer process removes atoms from the Rydberg state.

of the inelastic collision rate. The inelastic collision rate should be a capture rate multiplied by a probability of energy transfer. The capture rate will depend on the collisional cross section, given by:

$$\sigma = \pi R_0^2 \tag{3.4}$$

where

$$R_0^6 = \frac{C_6}{kT}. \tag{3.5}$$

The capture rate is then the Rydberg atom flux, ηv, times the cross section σ. For the 43d state at our typical Rydberg density of η=10^7 cm^{-3}, we calculate a capture rate of 200 s^{-1}. The inelastic collision rate is further reduced by the probability of energy transfer. For states such as 43d the van der Waals interactions are repulsive at long range. Since there are no thermally accessible curve crossings we expect the rate to be suppressed by at least a Boltzmann factor $e^{-\Delta E/kT}$, which is a minimum of $\sim 10^{-2}$ at 43d. Thus, we expect no more than a 2 s^{-1} inellastic collision rate, in agreement with the data suggesting these collisions are not a major factor in the dynamics of the

system. Instead, the loss from the trap is dominated almost exclusively by black-body ionization, and this only affects a very small fraction of the atoms excited. This will be explained more fully after the introduction of a model to our data in Chapter 4.

Since the atoms rarely leave the trap due to Rydberg-Rydberg collisions or ionization, they must primarily return to the ground state via emission of one or more photons. As explained in Section 2.5, we have an excellent complimentary method to trap-loss observation in the detection of cascade 420 nm decay photons. Looking at fig. 3.1, the cascade signal has a background of 250 s^{-1}, mainly from dark counts, and reaches a peak signal of about 10,000 s^{-1}. In order to gain a better understanding of the dynamics of the Rydberg atoms, we can compare these observed rates with the expected rates. In Equation 2.11 we developed a means of determining the number of Rydberg atoms from the cascade rate. In equilibrium conditions, this number should also be equal to the rate of Rydberg creation divided by the rate of Rydberg loss. If we assume only spontaneous emission and black-body radiation, the number of Rydberg atoms can be written as:

$$N_r = \frac{R_2 N_g}{A_r + A_{bb}} \tag{3.6}$$

where $R_2 N_g$ represents the rate of excitation of Rydberg atoms, A_r the spontaneous decay rate, and A_{bb} the rate of black-body radiation causing transitions to nearby Rydberg states.

It is assumed that only decay that goes directly to the 6p level will be seen by our detection system. To see why this is, we can examine the probability of a multi-step decay into the 6p. As a result of the ω^3 dependence of the decay rate, long wavelength transitions are disfavored, and p and f Rydberg states primarily decay to states lying below the 6p level: 5s, 6s, and 4d. Even if decay does occur into a state above 6p, the dominant decay channel is then again to states below the 6p. Thus the cascade

fluorescence is a reliable measurement of the s or d Rydberg populations, and insensitive to p or f populations. Since the first black-body transition would take the atoms to states that cannot be observed by our system, these will not result in detected cascade photons.

Using this assumption that only spontaneous decay and black-body radiation remove atoms from the Rydberg state, we can then combine eqns. 2.11 and 3.6 to predict the total detected photons.

$$C_o = R_2 N_g b_{6P} b_{5S} \eta \frac{\Theta}{4\pi} \frac{A_r}{A_r + A_{bb}} \tag{3.7}$$

For the data shown in Figure 3.1, this would predict 18,000 $\pm$ 4,000 s^{-1}, while only 10,000 s^{-1} are observed, 55% of this rate. While not a conclusive measurement, this suggests that our assumption that the only mechanisms responsible for atom transfer are spontaneous decay and black-body radiation may be false. Instead, it is possible that up to 50% of the Rydberg atoms are being transferred out of the excitation state by some other process. This ratio of expected-to-detected cascade counts was also calculated for the other excitation states. All these results are similar, as shown in Table 3.1. By the arguments given earlier, the explanation cannot be inelastic Rydberg-Rydberg collisions. Thus it appears possible that there is a mechanism for population transfer which does not result in trap-loss. In order to investigate this idea more thoroughly, in the next section I will introduce our final tool for Rydberg detection.

3.5 Stimulated Emission Probe

Since the evolution of the Rydberg state is of central importance to dipole blockade experiments, there is great benefit to obtaining a better understanding of the mechanisms for possible population transfer in this state. In addition, the particular

application of dipole blockade to single-atom and single-photon sources discussed in [Saffman and Walker, 2002] uses stimulated emission to couple the blockaded Rydberg state to an intermediate atomic level. Thus it is natural to pursue the development of a stimulated emission probe of Rydberg dynamics. As described in Sec. 2.3.3, we apply a tuneable diode laser to perform stimulated emission from the Rydberg state to the $6p_{3/2}$ state.

The maximum attainable stimulated emission rate out of the Rydberg state varies from 5×10^5 to 5×10^6 s^{-1}, depending on the principal quantum number. This rate is significantly faster than the spontaneous or black-body radiation rates, which are on the order of 1×10^4 s^{-1}. The natural decay of the $6p_{3/2}$ level of 9.2×10^6 s^{-1} is fast enough that population cannot accumulate there. While being less general than field ionization, this technique does have the potential to be applied to a number of different states, provided that the transition is allowed by dipole selection rules. In addition, the probe is nondestructive in that it returns the atoms to the ground state without loss, and has inherently high spectral resolution. Most importantly for our purposes here, the intensity dependence of the signals produced by the stimulated emission probe give additional information about the population dynamics of the Rydberg states.

When the stimulated emission probe is on resonance with the Rydberg state, two important effects can be seen. First, the rate of 420 nm photon detection increases greatly since the atoms are returned to the $6P_{3/2}$ state much more quickly than by only spontaneous emission. The second important effect is a reduction in the amount of trap loss. Quick removal of atoms from the Rydberg state reduces the trap loss as atoms do not stay excited long enough for ionization or collisions to remove them from the trap. Keeping the excitation beams on resonance with the two-photon excitation, we can scan the frequency of the stimulated emission probe to observe the $6P_{3/2}$ hyperfine manifold. Such a scan is shown in Figure 3.4.

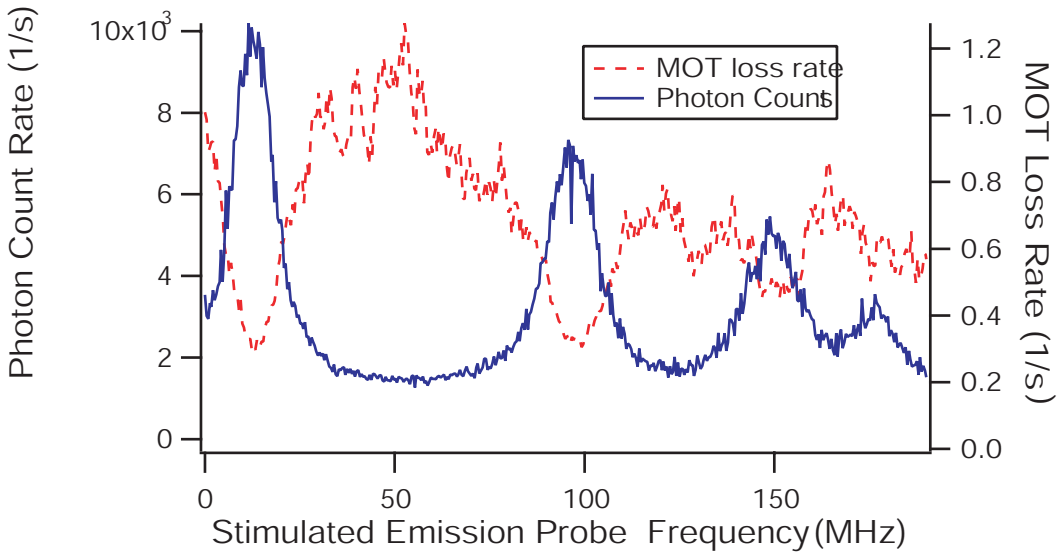

Fig. 3.4: Observed trap loss (dashed line) and photon count rate (solid line) as a function of stimulated emission probe frequency across the 28d-6p$_{3/2}$ manifold. The background cascade count rate is around 1000/s. The decreased trap loss rates which are coincident with 6p-hyperfine-manifold resonances imply that the atoms do not spend enough time in the Rydberg state to undergo loss when the probe beam is on resonance with the 6p state.

One method of measuring the effect of the state probe laser is by detecting the rate of $6p_{3/2}$ decay photons as a function of the stimulated emission rate from the Rydberg state. An example of the count rate data, scaled by the number of ground state atoms, is shown in Figure 3.5 for 28d. This figure demonstrates that for sufficiently high stimulated emission rates the count rate can be saturated, implying that the rate of stimulated emission has overcome any competing mechanisms which remove the population to states other than $6p_{3/2}$. Surprisingly, the necessary stimulated emission rates are much higher than expected, with the counts saturating at $1 \times 10^5\ s^{-1}$ for 28d. This allows us to make an estimate of the rate at which population is transferred out of the Rydberg state, γ. If the only population transfer mechanisms competing with the stimulated emission were spontaneous decay or black-body transfer (rates of $4 \times 10^4\ s^{-1}$ and $2 \times 10^4\ s^{-1}$, respectively) [Gallagher, 1994], this transfer rate would be much slower. Instead, our measurements imply an effective 28d lifetime of $\sim$7 μs.

As an additional measure of the tranfer rates, we can similarly observe the reduction in trap-loss as a function of stimulated emission rate, as seen in Figure 3.6. Again, the figure demonstrates that by using sufficient stimulated-emission probe intensity the atoms can be removed from the Rydberg state before the dominant loss mechanism removes them from the trap. This process thus reduces the total loss rate of the MOT. As with the data obtained from the count rate, we again see a faster than expected loss from the Rydberg state, with the population transfer being about $1.3 \times 10^5\ s^{-1}$.

As can be seen from Fig. 3.6, there is a non-zero loss rate at high probe intensities where the stimulated emission laser should fully deplete the original excitation state. There are several possible explanations for this. If there were a loss mechanism that was being enhanced by the stimulated emission probe, this would produce such a behavior. However, processes such as photoionization caused by the stimulated emission probe or light-induced 6p-5s collisions can be estimated to be far too weak to account for this

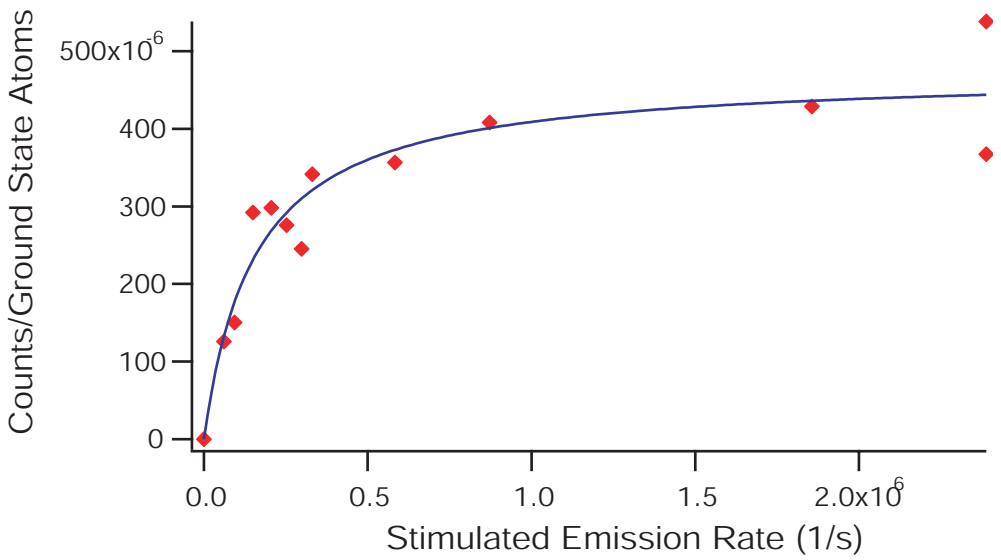

Fig. 3.5: Dependence of $6P_{3/2}$ decay counts on stimulated emission probe intensity for the 28D state, showing short residence times for the Rydberg state produced by two-photon excitation. The line is a fit to Eq. 3.13 as explained in Section 3.6. For this data $\gamma = 1.2 \pm 0.4 \times 10^5/s$.

effect.

Another possibility has to do with Zeeman precession in the nD states causing population to accumulate in inaccessible magnetic sublevels. The magnetic field gradient used to confine the MOT atoms sets up a magnetic field of 1 G at the edges of the MOT, enough that precession between magnetic sublevels of the Rydberg atoms at the edges of the MOT occurs at a rate of several MHz, which is on the order of the stimulated emission rate. This rate of precession can be estimated by considering the strength of the Zeeman shift on the atoms of 2.8 MHz/Gauss. The rate of precession ω_B for a particular atom is then proportional to the magnetic field strength at the position of the atom multiplied by the Zeeman energy level shift. This means that for atoms on the edge of the MOT, $\omega_b \sim 1$ G $\times 2\pi \times (2.8 \times 10^6$ Hz/G$) = 1.8 \times 10^7$ s^{-1}. The result of this precession is that a fraction of the atoms (up to 1/3) move to a state that

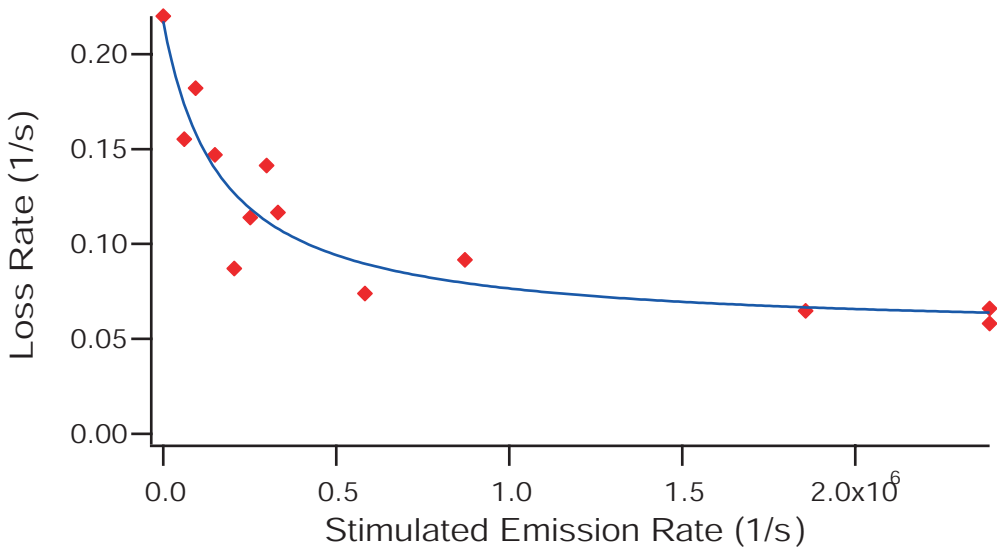

Fig. 3.6: Loss rate dependence on stimulated emission probe intensity for the 28D state. High probe intensities cause a reduction in the trap loss rate. The line is a fit to Eq. 3.12 as explained in Section 3.6. For this data $\gamma = 1.3 \pm 0.7 \times 10^5/s$, which is in close agreement with the result in Fig. 3.5 and serves as a check on the consistency of the model.

is inaccessible to the state-probe laser because of the dipole selection rules determined by the polarization of the state-probe laser. Linearly polarized state-probe light, for example, cannot transfer $m_J = \pm 5/2$ Zeeman levels from an $nd_{5/2}$ Rydberg state to the $6p_{3/2}$ state. This is because the $6p_{3/2}$ state contains only $m_J = \pm 3/2, \pm 1/2$ states and dipole selection rules require that $\Delta m_J = 0$ for transitions induced by linearly polarized light. Thus population that accumulates in these levels cannot be de-excited by the state-probe laser.

This effect was verified by repeating the experiment with the MOT magnetic field being switched off for 10 ms intervals and only switching on the Rydberg excitation lasers during the times the field was off. This data, shown in Fig. 3.7 for $n = 28$ shows that Rydberg populations at high state probe intensities are markedly reduced as com-

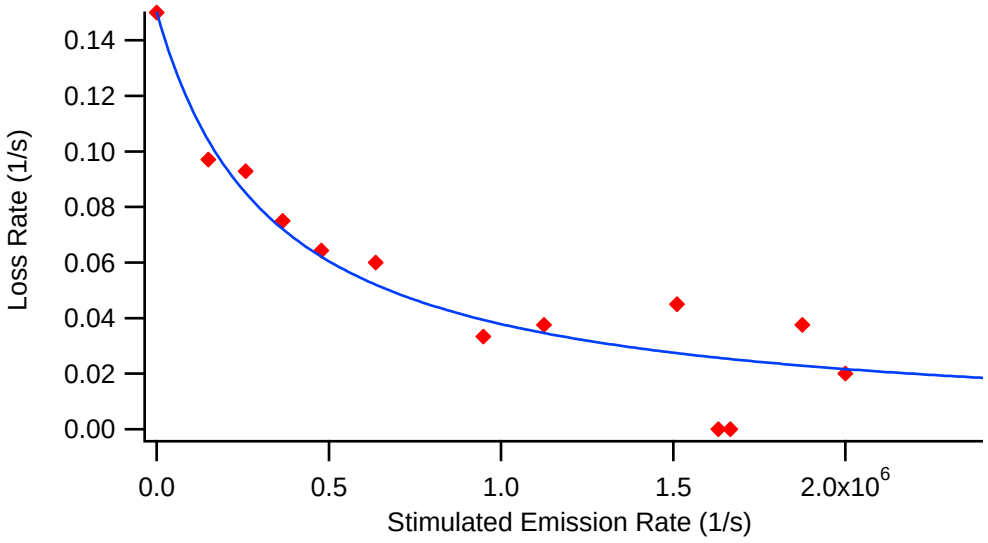

Fig. 3.7: Loss rate dependence on stimulated emission probe intensity with the MOT magnetic field switched off during excitation. The line is a fit to Eq. 3.12 as explained in Section 3.6. The data implies that the loss rate goes to zero at high probe intensities under these conditions.

pared to when the magnetic field is on. The reduced signal-to-noise for this experiment made it possible to do this only for $n = 28$, but this verified our understanding of the transfer rate measurements.

As an additional means of verifying that a transfer rate besides black-body radiation was occurring, we investigated the dependence of the transfer rate on excitation rate. The results are shown in Fig. 3.8, and shows that there is a dependence of the transfer rate on excitation rate. Thus it appears that the rate of transfer out of the Rydberg state depends on the population of that state. This confirms that some transfer process besides back-body radiation is occurring.

Studies of the dependence of the trap-loss and decay photons as a function of stimulated emission rate was done at 28D, 43D, 58D, and 30S. In all cases, the data implied that the population is being transferred out of the initial Rydberg state faster

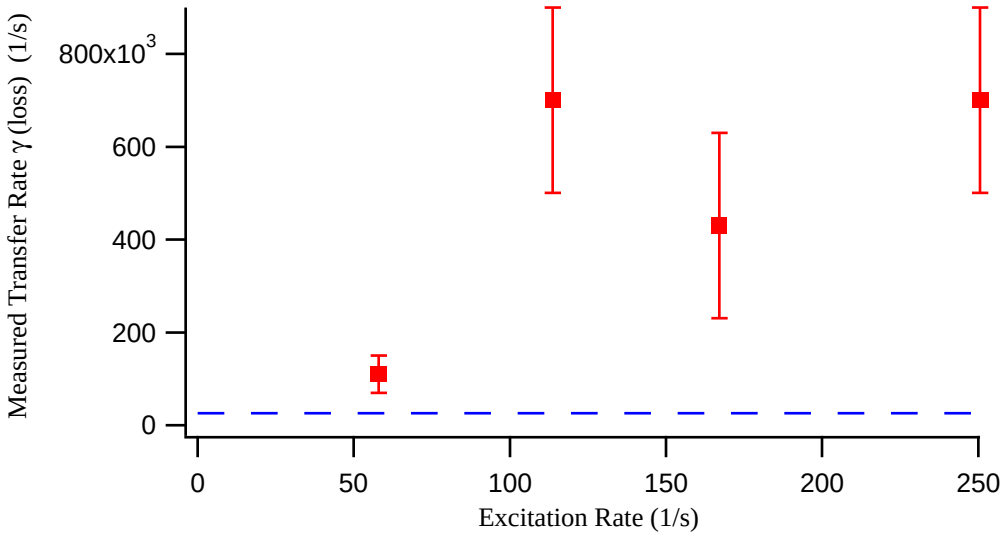

Fig. 3.8: Dependence of the measured Rydberg state transfer rate, γ(loss), on the excitation rate for the $28D$ state. The increase of the transfer rate with increasing excitation rate suggests the transfer rate depends on the population in the Rydberg state. Thus, black-body transfer is not the cause of the state transfer out of the excitation Rydberg state. The dotted line represents the rate of transfer due to black-body radiation (2.6×10^4 s^{-1}), which should be the transfer rate in the limit of small Rydberg populations.

than can be accounted for by spontaneous decay and black-body radiation. In order to obtain quantitative detail about this transfer rate, we developed a model of the system.

3.6 Model of Rydberg Population Dynamics

In the preceding section, we observed that transfer from the Rydberg state happened on a faster timescale than expected. In order to obtain a more quantitative understanding of the dynamics, it was necessary to develop a model of the system. In this section I will describe our simplified model of Rydberg dynamics, and how it can be used to extract the important parameters of transfer rate and loss rate from the data.

The processes included in the model are illustrated in Fig. 3.9. We describe the system with a three state model: A ground state $|g\rangle$ with N_g atoms, the excitation Rydberg state $|r\rangle$ with N_r atoms, and an additional effective Rydberg state $|s\rangle$ that accounts for other states that are populated from state $|r\rangle$.

The dynamics of the excitation state $|r\rangle$ depend on laser excitation and de-excitation, spontaneous and black-body radiation, and transfer to the other Rydberg states $|s\rangle$. Population enters $|r\rangle$ by excitation from the ground state at a rate $R_2 N_g$ where R_2 is the effective excitation rate calculated as described in Section 3.2. Spontaneous decay to low-lying levels occurs at a rate $A_r N_r$. Black-body radiation and other potential processes that transfer atoms to other Rydberg states occur at a rate γN_r. There is also the possibility of trap loss (through ionization, for example) at a rate Γ_r directly from state $|r\rangle$. Finally, de-excitation from the state-probe laser occurs at a rate $R_3 N_r$. Thus

$$\frac{dN_r}{dt} = R_2 N_g - A_r N_r - R_3 N_r - \gamma N_r - \Gamma_r N_r \tag{3.8}$$

is the rate equation for the excitation state population.

The other Rydberg states are produced by collisional or radiative transfer from state $|r\rangle$ at the rate γN_r and have an effective radiative lifetime A_s. If an atom in one of these Rydberg states represented by the state $|s\rangle$ is transferred to a different Rydberg state (also represented by $|s\rangle$), for the purposes of the model this atom will have remained in state $|s\rangle$. We also assume that these states can cause trap loss at a rate Γ_s due to black-body ionization and other collisional processes. Thus they obey

$$\frac{dN_s}{dt} = \gamma N_r - \Gamma_s N_s - A_s N_s \tag{3.9}$$

We are assuming that transfer from $|s\rangle$ back to $|r\rangle$ is unlikely.

In addition to the radiative de-excitation and excitation processes with the Rydberg levels, the ground state population N_g is affected by MOT loading (L) and loss (Γ_0)

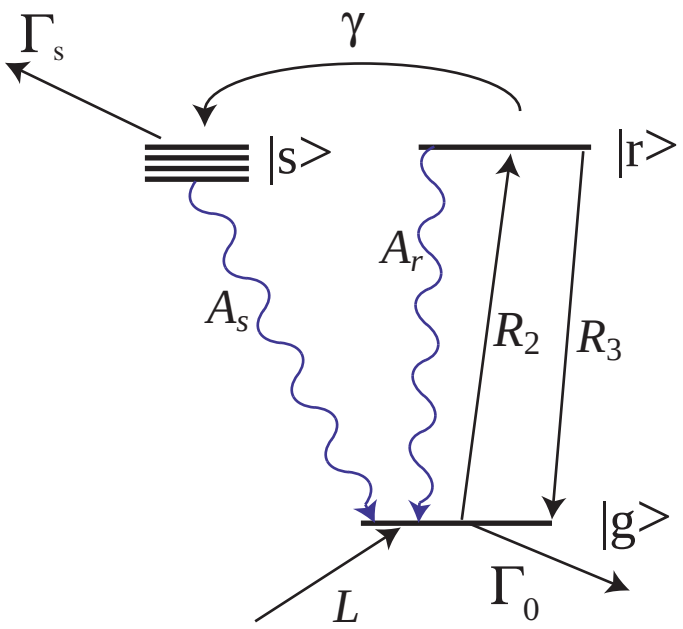

Fig. 3.9: Diagram of the simplified model of Rydberg population dynamics used to extract the parameters for transfer rate and trap loss rate.

processes (as discussed in Section 2.5.1) that we assume are not materially changed when the Rydberg excitation lasers are on. The resulting rate equation for the ground state population is

$$\frac{dN_g}{dt} = L - \Gamma_0 N_g - R_2 N_g + (A_r + R_3) N_r + A_s N_s. \tag{3.10}$$

We now wish to determine the loss rate Γ from this model in order to compare with our experimental observations. Since the Rydberg populations adiabatically follow the slowly-varying ground-state population, we may plug in the steady-state solutions to Eqs. 3.8 and 3.9 to get

$$\frac{dN_g}{dt} = L - \Gamma_0 N_g - \Gamma N_g. \tag{3.11}$$

The loss-rate from the trap is increased by an amount

$$\Gamma \approx \frac{R_2 \gamma}{A_r + R_3 + \gamma} \left[\frac{\Gamma_s}{A_s} + \frac{\Gamma_r}{\gamma} \right], \tag{3.12}$$

where the $\approx$ sign is due to the assumption that all of the atoms that decay from the $|s\rangle$ state will eventually return to the trap. Since our observed trap loss rates are much smaller than our excitation rates, this is a decent approximation. The loss rate here is a product of two factors. The first essentially measures the excitation rate of Rydberg atoms, modified by the de-excitation due to the state-probe laser. The second factor is the probability that the excited Rydberg atoms experience trap loss as opposed to radiatively decaying back to the ground state. Eq. 3.12 is used to determine the transfer rate γ and the trap loss Γ_s. An example of the data and fit for 28D is shown in Fig. 3.6.

In addition to predicting the increase in trap loss, the model similarly predicts the count rate of 420 nm photons produced by the state-probe laser:

$$\frac{I_3}{N_g} = \frac{R_3 R_2 \Theta \eta b_{6P} b_{5S}/4\pi}{A_r + R_3 + \gamma} \tag{3.13}$$

Thus the state-probe-induced 420 nm count rate can also be used to determine the transfer rate γ, with the data and fit for 28D shown in Fig. 3.5.

The results of fitting our experimental data to this model are summarized in Table 3.2. We list there the deduced values of the transfer rate γ using both the trap loss and photon count rates. The extracted values for γ agree quite well, which is an important internal consistency check and further bolsters the credibility of the model. Also included are the input parameters A_r and A_s. The calculation of A_r is straightforward, however we must assume something about the distribution of atoms in our other Rydberg states $|s\rangle$ to produce a value for A_s. We calculated this distribution of states using the method described in Chapter 4, and used a value for A_s equal to the average of this state distribution.

In addition to the transfer rates, the deduced trap-loss rate Γ_s and the calculated black-body loss rate $\Gamma_{s\ calc}$ are also included in 3.2. The deduced trap-loss rates, Γ_s,

State	γ(counts)	γ(loss)	A_{BB}	A_r	A_s	Γ_s	$\Gamma_{s\ calc}$
28D	1.2×10^5	1.3×10^5	2.6×10^4	4.1×10^4	3.1×10^4	265	325
43D	7.4×10^4	7.2×10^4	1.1×10^4	1.1×10^4	2.0×10^4	602	877
58D	2.6×10^4	2.0×10^4	6.1×10^3	4.8×10^3	7.4×10^3	433	548
30S	3.9×10^5	5.0×10^5	2.3×10^4	4.4×10^4	3.3×10^4	83	266

Tab. 3.2: A summary of the information involved in Rydberg population dynamics. The transfer rate γ using both count rate and loss rate methods is given, along with the black-body transfer rate A_{BB}, spontaneous emission rate A_r, and the estimated mean spontaneous emission rate A_s from other Rydberg states. The deduced trap loss rate Γ_s is shown along with the calculated black-body loss rate $\Gamma_{s\ calc}$ are also shown. All rates are in units of s^{-1}.

are quite modest for the data, with typical rates of order 400 s^{-1} on a per Rydberg atom basis. In fact, this is quite close to what would be expected from black-body ionization. The black-body ionization rates were recently calculated for s, p, and d Rydberg states in Rubidium by [Beterov *et al.* (2007)], and additional private communication gave further information of f states. In order to compare our deduced loss rate with these calculations, it was again necessary to have a better understanding of the final distribution of population among various Rydberg states $|s\rangle$, as there is a strong dependence of the ionization rate on the angular momentum of the state. Again assuming the distribution of states $|s\rangle$ calculated as described in Chapter 4, and assuming black-body ionization, we calculated the expected trap-loss rate $\Gamma_{s\ calc}$. For the d states, there is reasonable agreement between our deduced experimental rates and the theoretical calculation. This suggests that black-body ionization probably composes a large portion of the total loss from the trap. For the s state, the calculated loss rate is greater than our experimental observation by a factor of 3, for which we have no

explanation.

3.7 Conclusion

The combination of the information that can be obtained by trap-loss observations, detection of 420 nm decay photons, and the application of a stimulated emission probe provides an excellent means of understanding the Rydberg state dynamics. Using the evidence obtained using these tools, we are able to make several important conclusions about the population dynamics in the Rydberg states. The primary results then are these:

- The atoms transfer out of the excitation Rydberg state at a rate γ that is substantially faster than spontaneous decay or black-body transfer rates.
- The mechanism for population transfer, to an excellent approximation, does not directly cause trap loss.
- The rate for population transfer depends upon the population of the Rydberg state.
- The population transfer rate decreases slowly with increasing principal quantum number, as opposed to the expected rapid increase if near-resonant energy transfer collisions were the relevant mechanism.
- The probability of trap loss is very small; most Rydberg excitations result in radiative repopulation of the ground state without trap loss.

These conclusions are consistent with our experimental data and simplified analysis, and give insight into the probable transfer mechanism. One possibility that fits the

conclusions drawn here is superradiant emission from the Rydberg state. An in depth study of this possibility will be pursued in the next chapter.

4. SUPERRADIANCE

4.1 Introduction

In Chapter 3 I discussed our observations of fast transfer of Rydberg populations. In considering the features of the mechanism for this transfer, it appears that a radiant transition is occuring on a timescale faster than spontaneous or black-body radiation could occur. Recently, [Wang *et al.*, 2007] observed superradiant transfer of atomic populations in Rydberg atoms. In this chapter, I will build on these observations, arguing that the evidence strongly suggests superradiance to be the transfer mechanism for our atoms.

I will begin with an introduction to the basic principles of superradiance as developed by [Dicke, 1954]. Since the Rydberg level energy spacing is so small, cooperative effects can become important in this regime. A simplified calculation can be used to show that the superradiant decay rate will be on the order of the transfer rates seen in Chapter 3.

To advance our understanding of the exact effects of superradiance and compare them to our experiment, I have developed a simulation of superradiance in Rydberg states. In Section 4.3 I will describe the workings of this model. A sophisticated and complete theory was developed by [Yelin *et al.*, 2005], but the complexity of this theory made it difficult to apply to our experimental results. To obtain a better understanding of our results, I expand upon the theory developed by [Gross and Haroche, 1982] to

calculate the decay rate into nearby states. Since our system consists of a very large number of possible transitions, the model is expanded to include all Rydberg levels until further additions do not affect the final result.

It was important to verify that this model correctly reproduces the major features of superradiance. The initial inversion, maximum rate of transfer, and timescale of radiation were all tested and reproduced the key features expected. As an additional test, we have simulated the result of the experiment in ref. [Gounand *et al.*, 1979] (which was performed at very low lying Rydberg states) and our model reproduces the features of the data shown there.

Finally, I will discuss how this model simulates the results of our experiments. It can be used to extract an expected value for the transfer rate, as well as the resulting distribution of resulting Rydberg states. Typically these simulations result in an expected transfer rate of $2 \times 10^5\ s^{-1}$. Although there are no adjustable parameters in the model, it naturally predicts Rydberg-Rydberg transfer rates on the order seen in our experimental data, indicating that this is likely the transfer mechanism observed.

4.2 Superradiance Theory

The possible importance of coherence in spontaneous radiation processes was first demonstrated by Dicke in 1954. Since that time excellent summaries have been compiled [Rehler and Eberly, 1971], and more complicated models of this theory developed [Yelin *et al.*, 2005], but much can still be learned from the basic principles.

The most simple discussion of supperradiance begins with the assumption that the spatial dimension of a sample is small compared with the wavelength of emitted radiation. If this is true, there are several important effects upon the sample. The individual atoms in an atomic cloud of N atoms for example, would be indistinguishable

by this emitted light. Thus, instead of behaving as individual dipoles, the system can be considered a single quantum mechanical system. Once put into an excited state, the system would evolve in a state that is invariant to atom permutation. This evolution results in strong correlations between the atomic dipoles, or a spontaneous phase-locking of the dipoles. A global radiating dipole proportional to N develops as a result, such that the radiated intensity is proportional to N^2.

The reasons why our sample of Rydberg atoms fulfills the conditions for superradiance can be seen from simple arguments. The size of our atomic cloud is on the order of $\sim$1 mm. For the atomic transitions discussed previously in the production and manipulation of Rydberg atoms, the wavelengths are on the order of 1 μm. These transitions clearly have a wavelength much smaller than the spatial extent of the sample, and would not be enhanced by superradiance, as expected.

However, it is important to consider the close spacing of the Rydberg energy levels. For example, the transition from 58D to 59P has a wavelength of 2.8 cm. This transition then clearly falls in the regime where the sample is small compared to the transition wavelength. Although this transition has a very low spontaneous decay rate due to the small frequency involved, superradiant transfer will then occur on this transition. The emission rate will be proportional to N^2, or enhanced by a factor of N on a per-atom basis. If further complications of superradiant emission are ignored, the superradiant decay rate will be on the order of

$$\frac{2\omega^3 N d^2}{3\hbar c^3} \sim \frac{4N\alpha^3 Ry}{3n^5\hbar}. \tag{4.1}$$

For our experiment, with N = 10^4 $n = 50$ Rydberg atoms, this is equal to 3×10^5 s^{-1}. The low spontaneous decay rate is compensated for by the large number of cooperatively radiating atoms. Since this expected superradiant decay rate is very similar to the

transfer rates seen in Chapter 3, it seems like this is an excellent candidate for the transfer mechanism observed.

4.3 Rydberg Superradiance Simulation

In order to further explore the possibility of superradiant transfer, there was a need for a more detailed model of how superradiance would occur in Rydberg states. In the development of Equation 4.1, a very simplistic view of superradiance was given. Though the general principle of superradiance appears with relative simplicity, it remains an active theoretical area due to underlying complexity.

There are several complex aspects of superradiance which we have ignored up until now. First, superradiance has a sharp dependence on the transition wavelength in the regime where this wavelength is on the order of the confinement size. Second, the introduction of multiple channels of superradiant decay could result in competition or interference between nearby energy levels. Third, superradiant light propagates through an inverted medium, and exhibits strong nonlinear propagation and diffraction characteristics which can compete against the interatomic correlation. Finally, we have ignored atom-atom interactions, and in particular the competition between superradiance and dipole-dipole dephasing.

Taking all of these aspects into a model of superradiance poses a significant theoretical challenge and demands large numerical computational power. There have been several attempts to understand superradiance at this level of complexity, including the recent model created for superradiance in Rydberg states [Yelin *et al.*, 2005]. Unfortunately, the level of complexity necessary in these attempts can inhibit the easy extraction of simple parameters.

As an alternative to this complex modeling, we have developed a simplified version

which still includes the basic properties of superradiance. Here we allow for transitions to all nearby Rydberg states, and also incorporate the importance of the relative size of the wavelength. Clearly this will not result in exact solutions, but it does allow an excellent test of the experimental observations.

The model is expanded upon that developed by [Gross and Haroche, 1982] which considers superradiant decay of an initial state $|e\rangle$ to a lower energy state $|l\rangle$. In this case, as in Dicke's original work, the effective collective spin state of the system is defined as $|JM\rangle$, with $N_e = J + M$ atoms in the state $|e\rangle$ and $N_l = J - M$ atoms in the state $|l\rangle$. The radiation rate is then $\gamma_{el}(J(J+1) - M(M-1)) = \gamma_{el}N_e(N_l + 1)$, where γ_{el} is the spontaneous radiation rate from $|e\rangle$ to $|l\rangle$.

To generalize this two-level model to our system requires expansion of this general rate equation to incorporate all possible superradiant decay channels both into and out of a particular state $|e\rangle$. This results in a set of rate equations

$$\frac{dN_e}{dt} = -\sum_{l<e} \gamma_{el} N_e(N_l + 1) + \sum_{l'>e} \gamma_{l'e} N_{l'}(N_e + 1). \tag{4.2}$$

To fully simulate superradiance in the Rydberg levels, we must incorporate all levels below the excitation state that population could eventually transfer into. In addition, we must take into account the other known processes which will also play an important role in population transfer, particularly spontaneous decay to the ground states (A_n), black-body radiation (A_{bb}), and stimulated emission from the Rydberg State Probe (R_3). Because of the abundance of possible superradiant channels, especially at high principle quantum number, this can become complicated quite quickly. An example showing the equations to be solved for the case of excitation to 28d can be seen below in Equations 4.4 - 4.8:

$$\begin{aligned}
\frac{dN_g}{dt} &= L - \Gamma_0 N_g - R_2 N_g + R_3 N_{28d} \\
&\quad + A_{28d}N_{28d} + A_{29p}N_{29p} + A_{26f}N_{26f} + A_{29s}N_{29s} + A_{27d}N_{27d} \qquad (4.3)\\
\frac{dN_{28d}}{dt} &= R_2 N_g - R_3 N_{28d} - A_{28d}N_{28d} - A_{bb}N_{28d} + \frac{A_{bb}}{5}(N_{29p} + N_{26f}) \\
&\quad - \gamma_{28d\ 29p} N_{28d} N_{29p+1} - \gamma_{28d\ 26f} N_{28d} N_{26f+1} \qquad (4.4)\\
\frac{dN_{29p}}{dt} &= -A_{29p}N_{29p} - A_{bb}N_{29p} + \frac{A_{bb}}{5}(N_{28d} + N_{29s} + N_{27d}) \\
&\quad + \gamma_{28d\ 29p} N_{28d} N_{29p+1} - \gamma_{29p\ 29s} N_{29p} N_{29s+1} - \gamma_{29p\ 27d} N_{29p} N_{27d+1} \qquad (4.5)\\
\frac{dN_{26f}}{dt} &= -A_{26f}N_{26f} - A_{bb}N_{26f} + \frac{A_{bb}}{5}(N_{28d} + N_{27d}) \\
&\quad + \gamma_{28d\ 26f} N_{28d} N_{26f+1} - \gamma_{26f\ 27d} N_{26f} N_{27d+1} \qquad (4.6)\\
\frac{dN_{27d}}{dt} &= -A_{27d}N_{27d} - A_{bb}N_{27d} + \frac{A_{bb}}{5}(N_{29p} + N_{26f}) \\
&\quad + \gamma_{29p\ 27d} N_{29p} N_{27d+1} + \gamma_{26f\ 27d} N_{26f} N_{27d+1} \qquad (4.7)\\
\frac{dN_{29s}}{dt} &= -A_{29s}N_{29s} - A_{bb}N_{29s} + \gamma_{29p\ 29s} N_{29p} N_{29s+1} + \frac{A_{bb}}{5} N_{29p} \qquad (4.8)
\end{aligned}$$

Here, for simplicity of view, only five Rydberg levels are included. So far we have not discussed the extent to which superradiant transfer continues and how many levels are necessary to include in any simulation. The exact extent to which collective behavior occurs for wavelengths near the size of the MOT requires careful examination, as superradiance will begin to occur at a reduced rate as wavelengths decrease. This is taken into account by the introduction of a cooperativity parameter C_{el}, which can reduce the effective spontaneous decay rate for small wavelengths. The cooperative decay rates used in eqs. 4.4 - 4.8 are then the spontaneous emission rate multiplied by a cooperativity parameter C_{el},

$$\gamma_{el} = C_{el} \frac{2e^2\omega_{el}^3}{mc^3} \frac{(2J_l + 1)}{(2J_e + 1)} f_{el} \qquad (4.9)$$

where the f_{el} are the calculated absorption oscillator strengths. Following Ref. [Rehler and Eberly, 1971], the cooperativity parameter for a uniform density system of

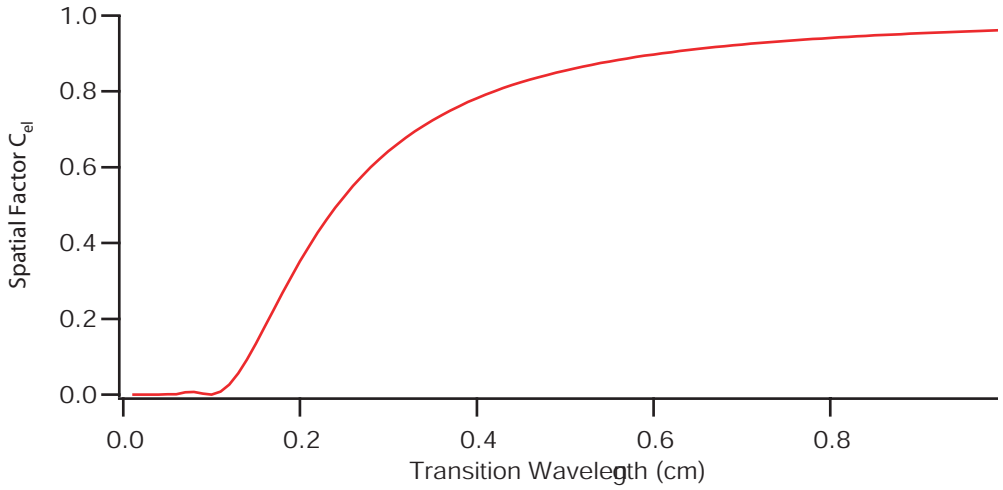

Fig. 4.1: Variation of the cooperativity parameter with wavelength. The parameter is effectively zero for wavelengths much smaller than the MOT size, and unity for wavelengths much greater.

N atoms in a volume V radiating in direction $\hat{k}$ is (in the $N \gg 1$ limit)

$$C_{el} = \frac{1}{V^2}\int d^3x \int d^3x'\, e^{i(\vec{k}-\vec{k}_1)\cdot(\vec{x}-\vec{x}')} \tag{4.10}$$

$$= \frac{9(\sin(k_{el}R) - k_{el}R\cos(k_{el}R))^2}{(k_{el}R)^6}, \tag{4.11}$$

for a spherical uniform density cloud, where kR is the product of the wavenumber and the radius of the atomic sample. The cooperativity parameter is 1 for $R \ll \lambda$ and decreases to 0 for $R \gg \lambda$. Figure 4.1 shows how the cooperativity parameter C_{el} varies with the transition wavelength for atoms in the MOT.

The wavelength of the transition to the nearest lower lying Rydberg state varies from 2.8 cm for the 58D-59P to 0.17 cm for 30S-29P transition. As a result, superradiance is reduced at lower wavelengths, serving to balance the very strong n^{-5} dependence expected from eq. 4.1 and make the relative effects of superradiance and spontaneous decay approximately constant for the Rydberg levels used in our experiments. Though reduced by the cooperativity parameter, at least one superradiant channel would occur

down to n∼21, and all states until this point should be included for fullness. However, at each lower level along the descent of Rydberg states, superradiance again competes with spontaneous emission and black-body decay.

In order to solve the series of differential equations and determine how many levels are necessary to include, I have written a program in Igor which numerically integrates these equations and displays the population in the various states as a function of time following excitation. To determine the number of Rydberg states necessary to include, I have simply continued adding states until further additions did not appreciably change the steady-state population in the original excitation state. In general, this requires approximately eight Rydberg levels included in the simulation.

4.4 Tests of the Simulation

Before attempting to draw conclusions about the Rydberg state dynamics, it was necessary to verify that the simulation is working as expected. These comparisons are made slightly more complex due to the fact that we are the first group to consider superradiance in a steady-state scenario. Both previous theory development and previous experiments have been done studying the decay following a brief excitation pulse.

Thus, in order compare our simulation with these expectations, we slightly adjusted the program. Instead of having continuous excitation from the ground state, the excitation laser was removed from the simulation, and instead the simulation began with a given population in the uppermost Rydberg state. The results of this simulation did in fact reproduce the key features of superradiance. The large initial Rydberg population radiates at the natural emission rate Γ_{el} at first, then gradually accelerates to a maximum rate $N\Gamma_{el}/4$. The time at which this emission rate maximum occurs at depends upon the number of atoms initially in the Rydberg state, occuring at a time

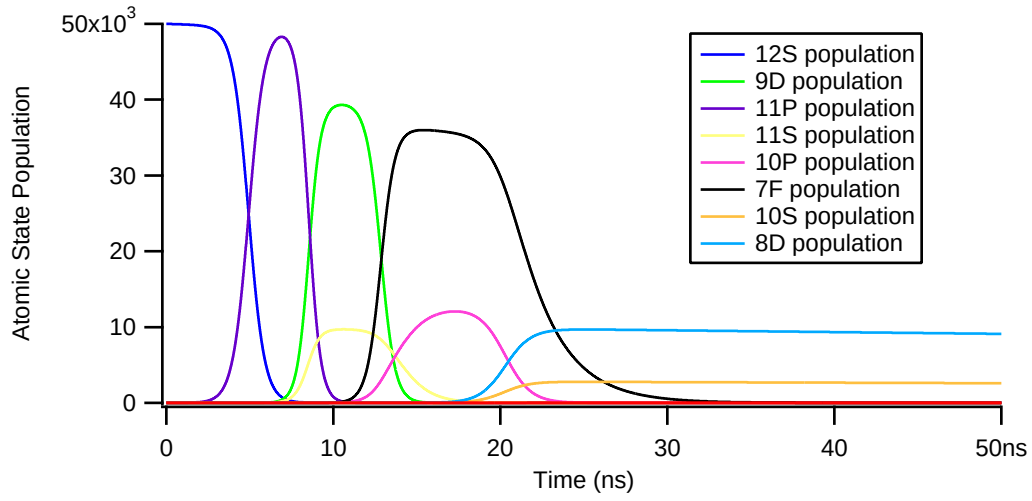

Fig. 4.2: Model simulation of the experiment by Gounand *et al.*, [Gounand *et al.*, 1979]. In the experiment, Rb atoms were excited to the $12s$ Rydberg level and superradiant cascade to lower levels was observed. Our model predicts superradiant population transfer on timescales similar to Fig. 2 in the reference.

$(\ln N)/(\Gamma_{el}N)$, much faster than $1/\Gamma_{el}$. Thus, all of the main properties of superradiance [Rehler and Eberly, 1971] are correctly simulated.

As a further test for the program, we simulated the experiment performed by [Gounand *et al.*, 1979]. In the first experimental observation of superradiance, Gounand *et. al.* excited atoms to the 12S state of Rubidium, and observed fluorescent decay from the various levels with a grating monochromator. While this experiment was done with hot atoms at very high densities and low principal quantum numbers, it can still provide a good test of our simulation. The result of our simulation is shown in fig. 4.2. Although the absence of several experimental parameters made it impossible to exactly simulate their conditions, the dominant features of the experiment are reproduced correctly. The decay from the 12S state occurs on the order of 5 ns, with population cascading through the 11P and 9D state before accumulating in the 7F state.

The fact that our simulation correctly generates the key features of superradiance

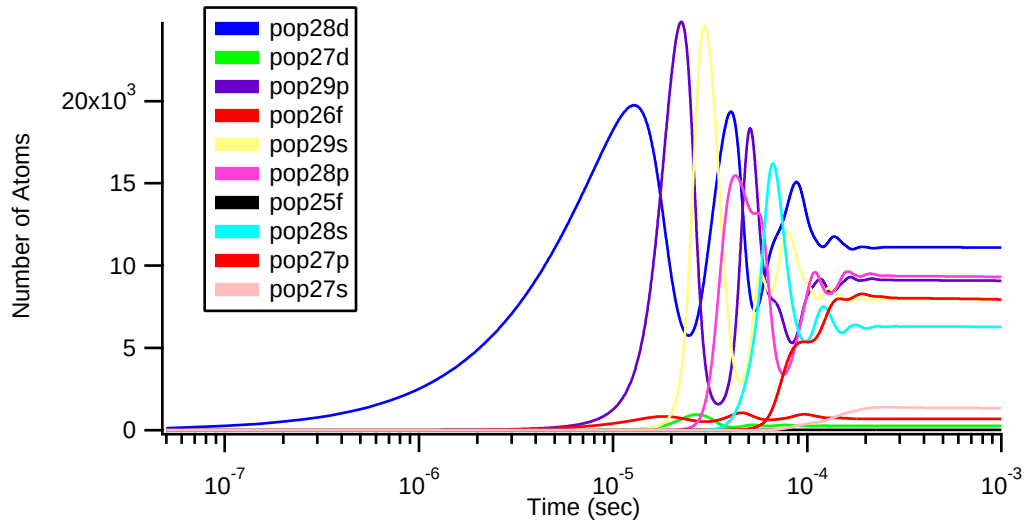

Fig. 4.3: The simulation results for excitation to the 28d Rydberg state. Fast superradiant transfer to lower states can be seen, resulting in large equilibrium populations in lower lying P and S states.

and duplicates the results seen experimentally gives strong evidence for its validity. When moving forward to the steady-state conditions used in our experiment, there are no direct known comparisons. Despite this, the resulting population dynamics reveal population buildup followed by radiation at an enhanced rate, and minor population oscillations resulting. All of these features agree with the superradiant picture, indicating the program is running successfully.

4.5 Simulation Results and Discussion

With confidence that the program is correctly simulating the known aspects of superradiant decay, we can simulate the various Rydberg excitations performed in Chapter 3. The results of this simulation for 28d are shown in Fig. 4.3, and for 58d in Fig. 4.4.

The simulation gives a prediction for the steady state population in the Rydberg levels near the excitation state. For the case of excitation to 30s and 28d the majority

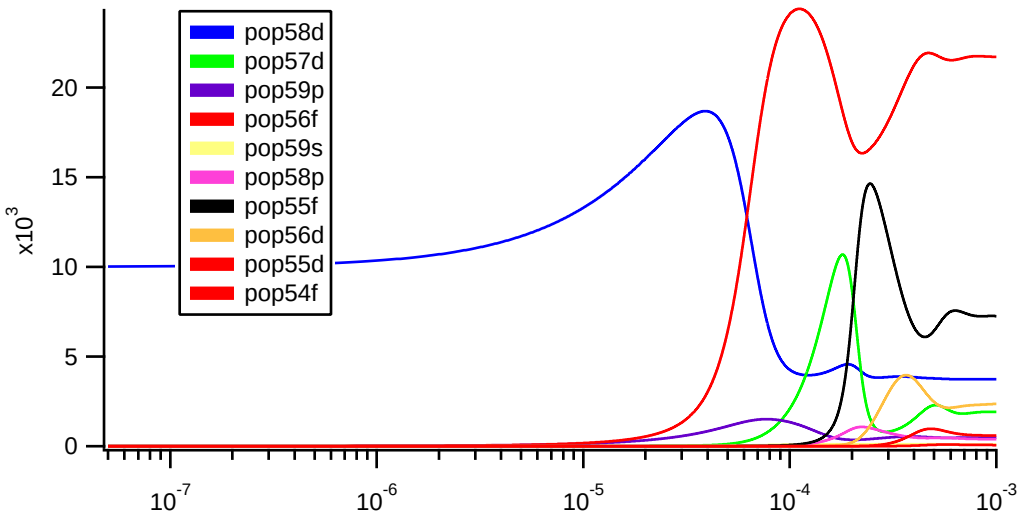

Fig. 4.4: The simulation results for excitation to the 58d Rydberg state. Fast superradiant transfer to lower states can be seen, resulting in large equilibrium populations in lower lying F and D states.

of population cascades through p and s states, while the 43d and 58d the majority of population cascades through d and f states. The population distributions obtained from the simulations were used to determine the effective A_s and $\Gamma_{s\ calc}$ as described in Section 3.6.

To understand the population distributions, we must consider the balance between the natural decay rate and the cooperativity parameter. The natural decay rate from $|nd\rangle$ to $|nf\rangle$ is faster than that from $|nd\rangle$ to $|np\rangle$ due to its shorter wavelength. However, this shorter wavelength also results in a decreased cooperativity parameter. At small principal quantum numbers where the wavelength is smaller than the size of the MOT, the sharp cooperativity parameter dependence dominates, and the long wavelength transition to P states is favored. Higher principal quantum numbers represent the opposite scenario. Here the wavelength becomes larger than the MOT even for $|nd\rangle$ to $|nf\rangle$ transitions, and the cooperativity parameter is close to unity for either transition.

As a result, the transitions to f states are favored at high principal quantum numbers due to their larger spontaneous decay rate, and transitions to P states are favored at low principal quantum numbers due to their larger cooperativity parameter. This transfer to f states at higher principal quantum numbers could explain the higher total loss rate from the trap for these levels.

State	γ(calculated)	γ(expt)
28d	1.7×10^5	1.3×10^5
43d	2.4×10^5	7.4×10^4
58d	1.2×10^5	2.0×10^4
30s	2.2×10^5	5.0×10^5

Tab. 4.1: A comparison of the experimental Rydberg-Rydberg transfer rates deduced using the model of Section 3.6 with those predicted by the superradiance simulation. As noted in the text, the simulation accounts for radiative lifetimes as well as blackbody induced l-changing transitions. All units are s^{-1}.

Important for comparison to our experiment is the deduction of a transfer rate from the simulation. By looking at the steady state number of atoms remaining in the original excitation state, and knowing the excitation rate, the effective transfer rate can be determined. We can compare this to the experimental measurements of the transfer rate γ from Section 3.6. Table 4.1 shows this comparison for the Rydberg levels excited in our experiment, indicating excellent agreement with the experimental results. It is worth noting that there are no adjustable parameters in the superradiance simulation. Despite this, it does an excellent job of predicting both the order of magnitude of the Rydberg transfer rates, and the dependence on quantum numbers. While a superradiance model including all pertinent effects might better explain the variation from experiment seen here, our simulation provides a good general understanding of the

system, revealing the essential properties of the superradiant decay channels involved.

Some attempt was made to directly observe population in lower lying Rydberg levels after excitation, as this is a key prediction of superradiant transfer. After excitation to 28d, the Rydberg State Probe was tuned to the $27d \rightarrow 6p$ transition. Unfortunately, we were not able to observe population in this state. To consider why this might be, remember that superradiance depends upon population in both states, as seen in eq. 4.2. Since the stimulated emission probe would remove population from the 27d state very quickly, it would effectively shut off the superradiant decay into this state. Attempting to observe these populations via a different means has not yet been attempted, but population is expected to be present.

Before the experiment of [Wang *et al.*, 2007] the effects of superradiance were not appreciated for the population dynamics of high density ultracold Rydberg atoms. Superradiance can happen on very rapid time scales, especially under strong Rydberg excitation as achieved in a number of previous experiments. In fact, superradiance can easily occur on sub-microsecond time scales. A key consequence of superradiance is that it populates Rydberg states lying energetically below the state being excited by the laser. Indeed, in the experiments of Ref. [Walz-Flannigan *et al.*, 2004] and Ref. [Li *et al.*, 2004], population clearly moves to lower lying Rydberg levels on a fast time scale, consistent with the hypothesis of superradiant transfer.

An additional consequence of fast superradiant population transfer is that it provides a mechanism for rapid population of states of neighboring orbital angular momentum l from the excitation state. Pairs of atoms with $\delta l = \pm 1$ interact at long range via the R^{-3} resonant dipole-dipole interaction, not the usual R^{-6} van der Waals interaction. The much stronger collision interactions between these atoms may explain the very rapid time scales for plasma formation in a number of experiments where resonant dipole-dipole interactions were not purposely produced using external fields.

The effects of superradiance are thus an essential aspect of Rydberg state dynamics, and necessary to take into account in many experimental situations.

5. FOUR-WAVE MIXING

5.1 Introduction

Having now gathered a large amount of information about Rydberg atom production and dynamics, we turn our attention to more direct application of their manipulation. An intriguing consequence of mesoscopic blockade would be the collective emission of single photons. This phenomenon could be used to produce a directional single-photon source [Saffman and Walker, 2002] or for fast quantum-state detection or transmission [Saffman and Walker, 2005]. The development of our stimulated emission Rydberg state probe allows for fast population of the $6P$ state, and the generation of 420 nm photons which could be the source of single-photons.

Assuming successful mesoscopic blockade, this scheme has an additional challenge to address in collection efficiency. Since the 420 nm photon in this scheme would be spontaneously generated, it would have an equal probability of emission in any direction in 4π. In an ideal single-photon source a photon could be obtained on demand, without some probability of not obtaining a photon. However, this spontaneous scheme would be limited by the fractional solid angle collection of a lens system, at best currently around 2% of the photons for our vacuum chamber. In order to make this scheme appealing, a means of increasing this collection efficiency beyond this limit must be developed.

In Section 5.2 I introduce the nonlinear process of four-wave mixing. This process

results in the 420 nm decay photons being emitted into a diffraction limited solid angle, providing the possibility of near unity collection efficiency. The theory behind four-wave mixing will be discussed, including two helpful physical interpretations of this effect.

The first step in the development of this technique was to confirm our understanding of the phenomenon involved. Theory predicts several strong dependencies which can be easily examined experimentally. I will discuss our methods of verifying the appearance of four-wave mixing and its predicted dependence in Section 5.3. Without further optimization, the efficiency of the process was limited to about 20% of the light being emitted into the desired direction.

To go beyond simply understanding the basic behavior of four-wave mixing, it was necessary to make a more detailed model of the system. To this end, a density matrix model was developed which simulates the populations and conditions of our experiment. This model is described in full in Section 5.4 and its implications explored. The model allows better understanding of the details of the process, and in addition gives insight into how to improve the efficiency of the four-wave mixing process.

Having already observed some of the important effects that can occur in the Rydberg state in Chapters 3 and 4, we can suppose that other processes may compete against the coherent process of four-wave mixing. In combination with the predictions of our model, this knowledge led us to explore the means of optimizing the four-wave mixing process. In Section 5.5 we show that excitation which is detuned from the Rydberg state results in increased four-wave mixing efficiency. Up to 50% of the light was seen emitted into a diffraction limited solid angle in this configuration, showing excellent promise for a single-photon source.

5.2 Four-Wave Mixing Theory

The field of four-wave mixing is now well developed within the nonlinear optics community [Bloembergen, 1996] [Yariv, 1971], and has been used in a number of applications including phase-conjugate mirrors [Cronin *et al.*, 1982] and generation of coherent VUV or IR sources [Sorokin *et al.*, 1973]. This process can be understood by considering a material's response to an electric field. The traditional way of modeling a material's response is to examine the induced polarization as a power series in the electric field strength:

$$\vec{P} = \chi^{(1)} \cdot \vec{E} + \chi^{(2)} \cdot \vec{E}\vec{E} + \chi^{(3)} \cdot \vec{E}\vec{E}\vec{E} + ... \tag{5.1}$$

where $\chi^{(n)}$ are the nonlinear susceptibilities of the material. The lowest order nonlinear susceptibility $\chi^{(2)}$ is essential to frequency doubling [Day, 2008], but vanishes for materials with inversions symmetry, such as our ultracold gas. The third order nonlinear susceptibility $\chi^{(3)}$ is responsible for four-wave mixing, and in our case is dependent upon the electric dipole matrix elements coupling the four states and the transition detunings and linewidths. This susceptibility results in a polarization induced in the atomic gas, which can be considered to result in a spatial phasing of the atomic dipole moments as a result of the three driving fields:

$$\langle \vec{d_i} \rangle = \langle \vec{d_0}(\vec{r_i}) \rangle e^{i(\vec{k}_1 + \vec{k}_2 - \vec{k}_3) \cdot \vec{r}_i}, \tag{5.2}$$

where $\vec{d_i}$ is the dipole moment of the ith atom and d_0 its magnitude as a function of atomic position $\vec{r_i}$.

If this induced dipole moment is used as a driving term in Maxwell's Equations, a set of four coupled wave equations will result for the fields. At this point, we assume that the loss of power from the input lasers is negligible, resulting in a simple equation for the gain in the fourth spontaneously generated field. If absorption from the medium

is ignored, gain is proportional to $\mathrm{sinc}^2(\frac{\Delta kL}{2})$, where

$$\Delta k = (\vec{k}_1 + \vec{k}_2 - \vec{k}_3 - \vec{k}_4). \tag{5.3}$$

Setting $\Delta k = 0$ in Equation 5.3 is known as the phase matching condition, with the system being phase-matched when $\Delta k = 0$. This is the essential condition for four-wave mixing to occur, and its importance can be seen in a number of ways. Perhaps the simplest is to consider the energy and momentum of the system. If $\omega_4 = \omega_1 + \omega_2 - \omega_3$ and $\vec{k}_4 = \vec{k}_1 + \vec{k}_2 - \vec{k}_3$ both energy and momentum are conserved in the process, and there will be efficient coupling between the four fields. Since we are returning to the ground state, energy is necessarily conserved, and the correct laser orientation will result in momentum conservation. That is, if the incoming laser fields are oriented geometrically such that the fourth field can be emitted in a direction that conserves momentum, this process will be highly favored over the random emission of photons.

Another equivalent way of understanding the phase matching condition is to consider the atomic dipoles as an antennae. If all four waves maintain a constant phase relationship to each other the fields will interfere constructively in the phase matched direction. If the phase matching condition is met, this will result in an electric field at a large distance R away of

$$E(\phi) = \frac{n\langle d_0\rangle k_4^2 e^{ik_4 R}}{R}\left(\frac{\pi w^2}{2}\right)^{3/2} e^{-\frac{\pi^2 w^2}{\lambda^2}\phi^2}. \tag{5.4}$$

We have assumed that the dipole moment is oriented perpendicular to the plane of the lasers, and that the effective spatial distribution of the dipoles is Gaussian with standard deviation $w/2$ and peak density n. The angle ϕ is measured with respect to the phase-matched direction.

The expected power emitted into the phase-matched direction can then be obtained by integrating the intensity deduced in Eq. 5.4 over the angular distribution

$$P_{pm} = N_e^2 2c\langle d_0\rangle^2 k_4^2/w^2. \tag{5.5}$$

This can be compared to the spontaneously radiated power from the 6P state

$$P_0 = N_e \hbar c k_4 \Gamma_p \rho_p. \tag{5.6}$$

From this, it can be seen that the ratio of power emitted in the phase-matched direction to the power emitted in all other directions should be:

$$\frac{P_{pm}}{P_o} \propto \frac{N_e |\sigma_{gp}|^2}{w^2 \rho_p}, \tag{5.7}$$

where $N_e = n(\pi w^2/2)^{3/2}$ is the effective number of participating atoms, ρ_p is the population of atoms in the $6P$ state, and σ_{gp} is the $6P$-$5S$ optical coherence density matrix element. Thus, with the correct orientation of the input lasers, and a high density sample, we expect that a large portion of light should be emitted into a diffraction limited direction.

In addition to the phase-matched four-wave mixing, there are several other important nonlinear effects which we have considered. Stimulated hyper-Raman scattering [Cotter *et al.*, 1977][Sorokin *et al.*, 1973] and parametric four-wave mixing [Wunderlich *et al.*, 1990] have been experimentally demonstrated and known for quite some time. If present, these effects would compete with the desired directional photon emission. However, they are predicted to be relatively negligible due to the small Rydberg matrix elements and thin optical depth. The dominant process should be phase-matched four-wave mixing, resulting in directional emission of the photons, and present a necessary step in developing a single photon source.

5.3 Experimental Observations of Four-Wave Mixing

In order to establish the presence of four-wave mixing in our experiment, it was necessary to orient the three input laser beams in directions which would satisfy the phase matching condition of Eq. 5.3. In principle, a wide variety of possible geometries can

be chosen that satisfy this condition, but there are several constraints which were taken into account. Most importantly, it is desirable for future blockade and single photon experiments to have a small excitation volume. In order to establish this, it is desirable to have a large angle between $\vec{k}_2$ and $\vec{k}_1$, allowing for the possibility of a small spatial overlap volume. Unfortunately, we are also limited by the accessible angles in our vacuum chamber windows. Certain geometries are either completely incompatible, or conflict with our trapping beams or observation.

The direction of the laser beams eventually selected as optimal given our limitations is shown in Fig. 5.1. A 39° angle separates $\vec{k}_2$ and $\vec{k}_1$, allowing a small overlap volume. This results in a phase-matched direction for the exiting 420 nm photons ($\vec{k}_4$) which is 3° from $\vec{k}_2$. While still satisfying the phase-matching condition, the direction of $\vec{k}_4$ is very insensitive to the direction of $\vec{k}_1$.

This orientation of lasers created some challenge in experimental implementation due to the required angles involved in the phase matching process. The vacuum chamber used in our experiment has windows in the necessary locations, but several of those ports were previously used for other optics, most importantly the trapping and cooling beam. While it is possible to overlap the trapping beams with the four-wave mixing lasers, this puts limitations on available focusing parameters and polarizations. To avoid this, we have instead changed the standard six beam MOT into a five beam MOT. Here the essential physics is the same, with the intensities altered to preserve a balanced force while simultaneously allowing the ideal phase-matching geometry.

In order to confirm the presence of four-wave mixing, we now use two Hamamtsu photon counters. One is placed along the the anticipated phase-matched direction (on-axis), while a second is placed along an arbitrary direction (off-axis). Initially $\vec{k}_1$ was moved far off of the phase-matched direction, and nearly equal 420 nm detection rates were confirmed in the on- and off-axis directions. Then as $\vec{k}_1$ was rotated into the

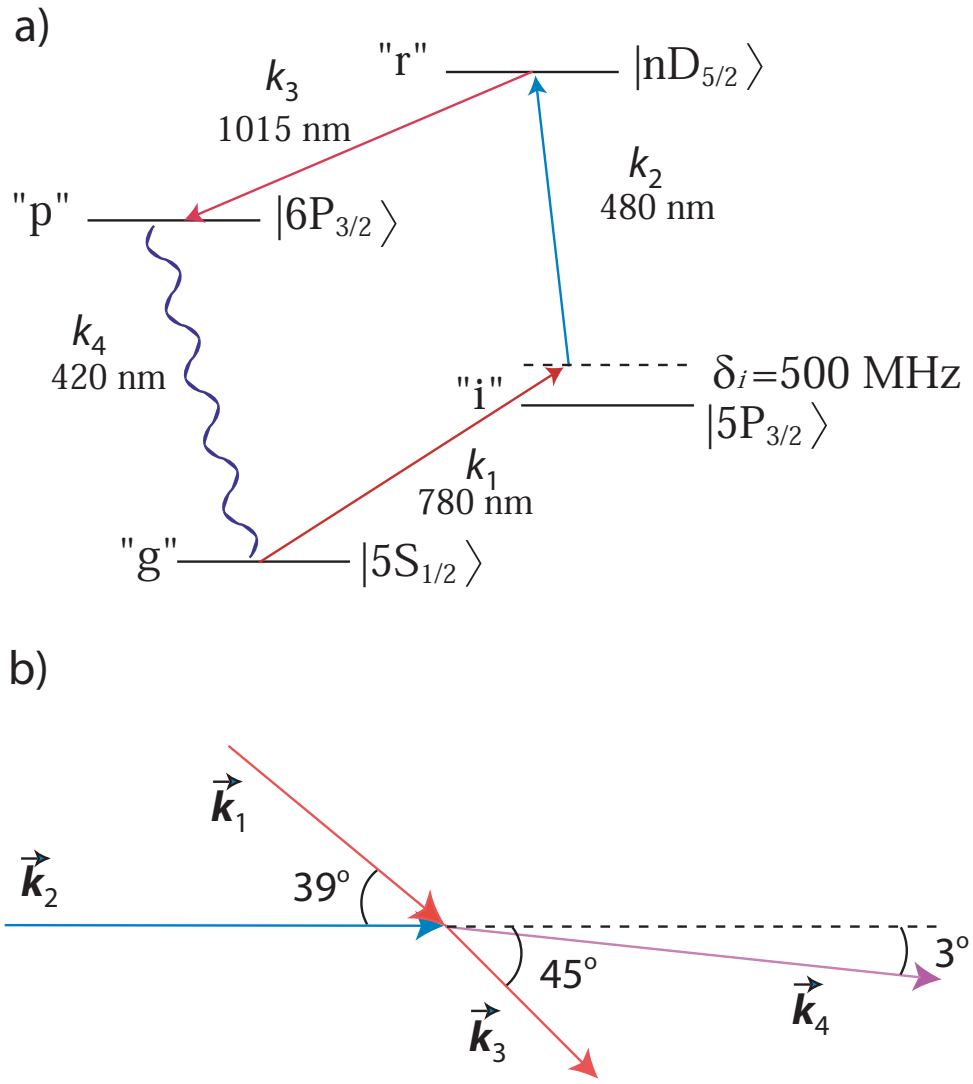

Fig. 5.1: a) Energy levels for four-wave mixing. The k_1 and k_2 photons produce two-photon excitation to an nD Rydberg level. The k_3 laser couples the Rydberg level to the $6P$ state. Atoms in the 6P radiate coherently to the ground state to complete the four-wave-mixing process. b) Phase-matching geometry.

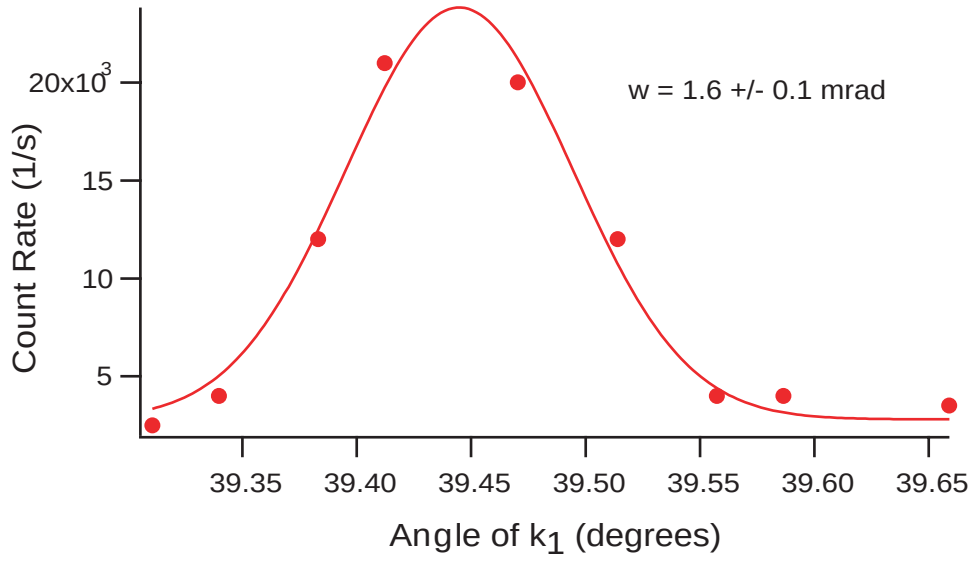

Fig. 5.2: The on-axis, or phase-matched, count rate is recorded while $\vec{k}_1$ is rotated through the phase-matching geometry. A large gain is seen while phase-matched, while no gain is seen on the off-axis counter.

phase-matched direction a factor of 10 jump in the count rate on the on-axis detector was observed, with no change in the off-axis count rate. As seen in fig. 5.2, the width of acceptance for phase matching when the angle of $\vec{k}_1$ was rotated was found to be $\delta\Theta_1 = 1.6 \pm .2$ mrad. The expected width can be found from examining the intensity, which is proportional to $\int_{-\infty}^{\infty} dx e^{i\Delta kx} n(x)$. Using the known distribution of atoms, we expect an acceptance width of 1.2 mrad, only slightly smaller than the observed value.

When exciting to a different n-level Rydberg state, different frequencies are involved, so the phase-matched geometry will vary slightly. In fact, a change of only a few n levels at fixed laser beam angles is enough to move the phase-matching condition outside the angular bandwidth. After changing from $28d_{5/2}$ to $58d_{5/2}$, $\vec{k}_1$ was rotated until phase matching was again attained, and the rotation angle was found to be 4.4 ± 0.3 mrad. This is consistent with the theoretical value of 4.1 mrad, calculated using the k-vectors

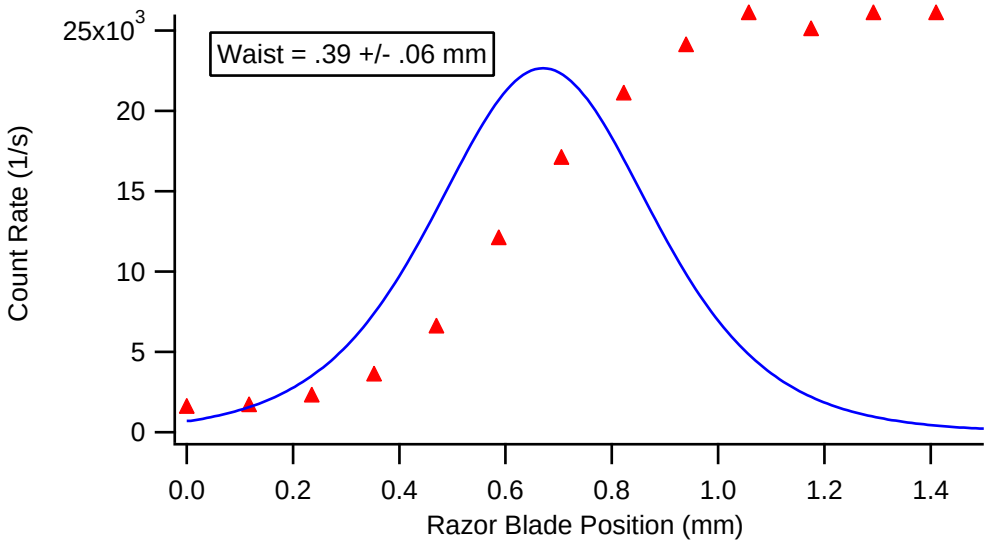

Fig. 5.3: The Count Rate in the on-axis direction as a razor blade is moved across the detection area. We have calculated the waist at the atoms by using Gaussian propagation through the imaging system before this razor blade. The observed .39 ± .06 mm waist is consistent with a diffraction limited beam.

involved.

In order to determine if the four-wave mixing process in fact resulted in a diffraction limited beam of 420 nm photons, we scanned a razor blade across the phase-matched output and recorded the count rate as a function of position. The results of this scan are seen in Fig. 5.3. The waist measured is consistent with a diffraction limited beam with a waist of 0.39 ± .06 mm at the atoms. An iris can be placed in front of the phase-matched detector to reduce the solid angle of the on-axis counter by a factor of 11 while changing the count rate by only 9%. As this allows for examination of only the phase-matched signal and a reduction of background noise, the further data in this section is taken with this iris in place.

From Equation 5.7 we expect the phase-matched fraction to depend linearly on the number of atoms involved in the process. As an additional means of verifying

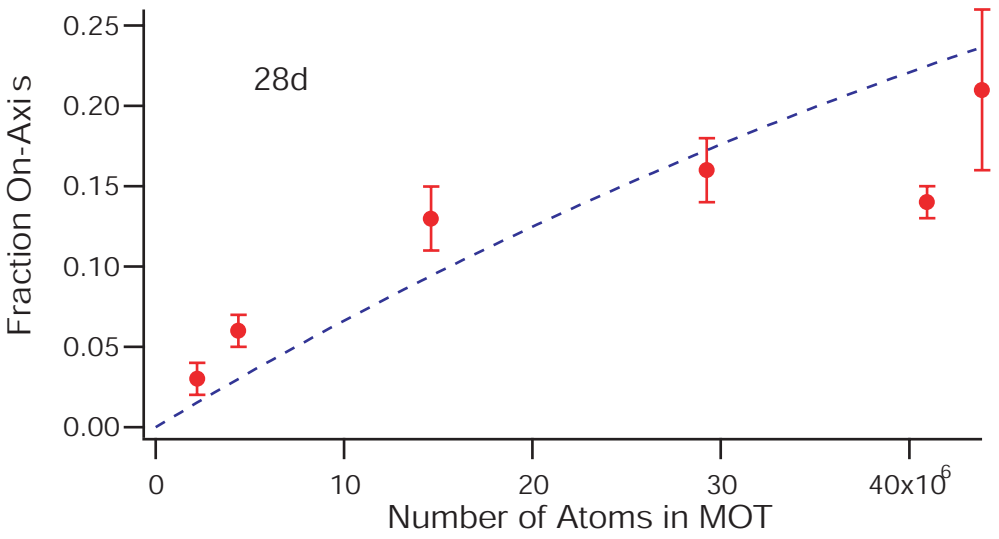

Fig. 5.4: The fraction of light emitted in the on-axis direction increases with the number of atoms in the MOT, as expected from the nonlinear character of four-wave mixing. The dashed line shows the model prediction, taking rescattering at large optical depths into account.

the predicted four-wave mixing behavior, we examined the efficiency of the four-wave mixing process as a function of the number of atoms in the MOT. Figure 5.4 shows the results of this measurement in terms of the fraction on-axis. To calculate this fraction, the filters and efficiencies of the two counters were taken into account, and the signal off-axis divided by the fractional solid angle to incorporate the total expected spontaneous radiation. The expected nonlinear response of the four-wave mixing can be seen as a linear increase in the phase-matched fraction with the number of atoms at small atom numbers, but deviates from this linear increase at high atom numbers.

Up until this point, we have assumed negligible absorption of the 420 nm photons from the MOT. However, in reality this is not a good assumption, as the optical depth of the MOT for photons at this wavelength is $\sim$0.3 at large N. As a result of this increasing optical thickness, the phase-matched light is partially scattered due to the

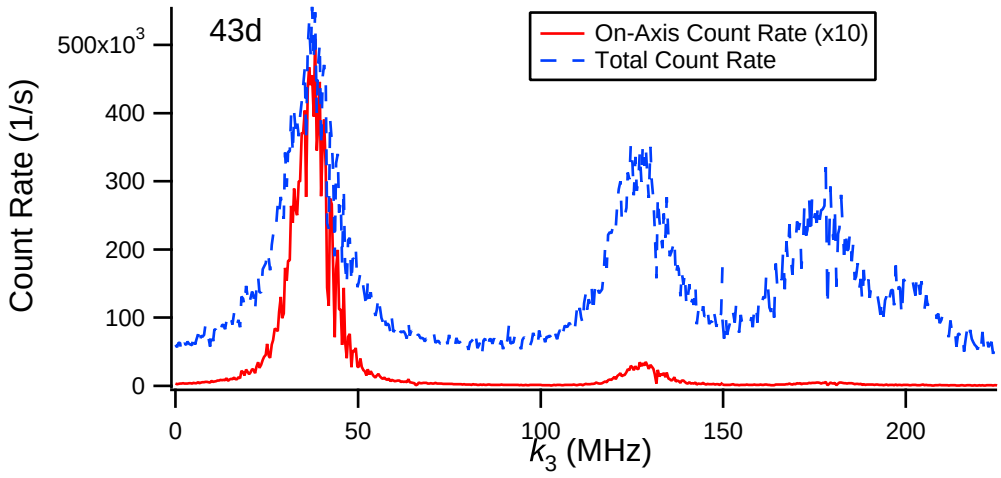

Fig. 5.5: Count rates as a function of k_3, showing the hyperfine manifold of the $6p_{3/2}$ state. The F′=3 produces strikingly more on-axis light than the other hyperfine levels due to its stronger coupling to the Rydberg state and the higher branching ratio into the F=2 ground state.

linear susceptibility of the atoms. This scattered component, up to 24% for large N, is then observed as additional off-axis light. This results in a limitation on the fraction seen on-axis, and can be seen in the saturation in Fig. 5.4. Our analysis takes this effect into account by multiplying the percent phase matched by the average transmission of $5s_{1/2} \rightarrow 6p_{3/2}$ photons given the optical depth of our sample. This results in a slight modification to Equation 5.7 which can be seen in the model prediction in fig. 5.4.

To begin to gain a more detailed understanding of the four-wave mixing process, we can examine the full hyperfine manifold of the $6p_{3/2}$ state. To do this, we again scan the frequency of the k_3 laser while recording the on- and off-axis count rates, as shown in fig. 5.5. For off-axis light, the F′=3 count rate is slightly higher than the other F′ levels, with the F′=2 count rate being 65% of the F′=3 rate. The on-axis light, on the other hand, has an observed 10:1 ratio for the two states, suggesting that the four-wave mixing process is strikingly stronger for the F′=3 level than the others. In

order to understand this difference and the total amount of four-wave mixing possible, it was necessary to develop a rigorous model of the system.

5.4 Four-Wave Mixing Model

Four-wave mixing is a coherent process, depending not only on the populations, but also the coherences of the various states as seen from Equation 5.7. Thus, in order to obtain a better understanding of the system, and be able to calculate the expected fraction emitted into the phase-matched direction, it is necessary to develop a density matrix model of the system. To do this, we use the model shown in Fig. 5.6. Here we have adiabatically eliminated the intermediate $5p_{3/2}$ state and characterized the system as a three level problem, with ground state $|g\rangle$, the Rydberg state $|r\rangle$, and the $6p_{3/2}$ state $|p\rangle$.

Solving for the coherence and population using this three-level density matrix approach results in the following set of differential equations:

$$i\dot{\rho}_r = \frac{\epsilon_2}{2}\sigma_{gr} - \frac{\epsilon_2}{2}\sigma_{rg} + \frac{\epsilon_3}{2}\sigma_{pr} - \frac{\epsilon_3}{2}\sigma_{rp} - \frac{i\rho_r}{\tau_r} \tag{5.8}$$

$$i\dot{\rho}_g = \frac{\epsilon_2}{2}\sigma_{rg} - \frac{\epsilon_2}{2}\sigma_{gr} + \frac{i\rho_r}{\tau_r} + \frac{i\rho_p}{\tau_p} \tag{5.9}$$

$$i\dot{\rho}_p = \frac{\epsilon_3}{2}\sigma_{rp} - \frac{\epsilon_3}{2}\sigma_{pr} - \frac{i\rho_p}{\tau_p} \tag{5.10}$$

$$i\dot{\sigma}_{rg} = -(\delta_2 + \frac{i\gamma_r}{2})\sigma_{rg} + \frac{\epsilon_2}{2}(\rho_g - \rho_r) + \frac{\epsilon_3}{2}\sigma_{pg} \tag{5.11}$$

$$i\dot{\sigma}_{pr} = (\delta_3 + \frac{i\gamma_{pr}}{2})\sigma_{pr} + \frac{\epsilon_3}{2}(\rho_r - \rho_p) - \frac{\epsilon_2}{2}\sigma_{pg} \tag{5.12}$$

$$i\dot{\sigma}_{pg} = -(\delta_t + \frac{i\gamma_p}{2})\sigma_{pg} - \frac{\epsilon_2}{2}\sigma_{pr} + \frac{\epsilon_3}{2}\sigma_{rg} \tag{5.13}$$

The 5s state "g" and the Rydberg state "r" are coupled by an effective two-photon Rabi frequency $\epsilon_2 = \epsilon_1\epsilon_2/\Delta$ ($\sim$ 4 kHz) obtained by adiabatic elimination of the $5p_{3/2}$ state. The Rydberg state is then coupled to the $6p_{3/2}$ state "p" with Rabi frequency

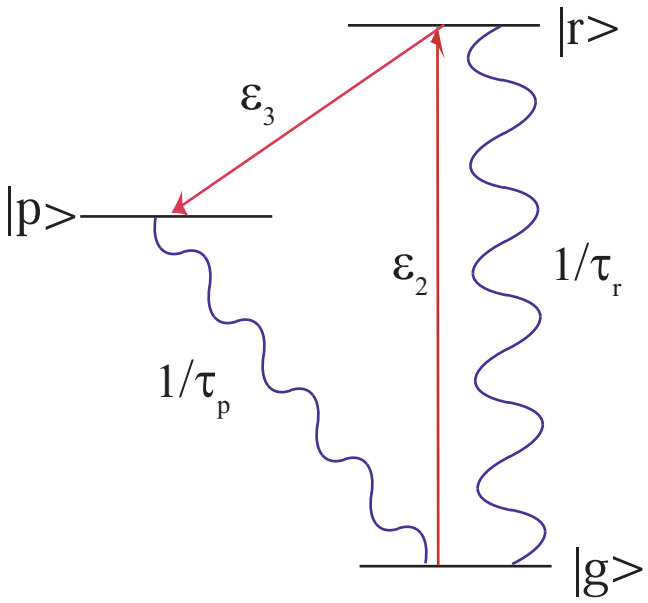

Fig. 5.6: Three level system used to model the four-wave mixing process. The various excitation and spontaneous decay rates are included, with an additional decoherence mechanism allowed. This decoherence mechanism is adjusted to match the experimentally observed transition broadening.

$\epsilon_3 \sim 1$ MHz. In order to simulate the effects of the substantial linewidths of the lasers used (1-3 MHz), plus other possible additional broadening mechanisms, we gave the σ_{rg} and σ_{rp} coherences effective homogeneous broadening factors of $\gamma_r = 6$ MHz, $\gamma_{rp} = 2$ MHz. These were chosen to reproduce the observed linewidths for two-photon excitation and non-phase-matched four-wave mixing, respectively. In addition, the Rydberg state was assumed to have a shortened lifetime (τ_r=8 to 40 μs depending on n-level) due to the effects of superradiance [Day, 2008], and the 6P state was assumed to decay at its spontaneous rate ($\tau_p = 121$ ns).

Since the hyperfine coupling in the Rydberg state is negligible [Li *et al.*, 2003], the effects of nuclear spin were accounted for by calculating effective Rabi frequencies assuming nuclear spin conservation in the Rydberg state. Calculating the branching ratios in the $5s \rightarrow 5p \rightarrow nd \rightarrow 6p$ three-photon process allows for the calculation of the populations in the various hyperfine levels of the $6p_{3/2}$ state. The details of this calculation are shown in [Day, 2008], and show that the fraction of atoms in each of the hyperfine levels of the $6p$ hyperfine manifold (F=3, 2, 1, 0) is 0.498, 0.224, 0.201, and 0.074, respectively. This calculation also shows that the effective de-excitation rate into the $F = 2$ level is 48% of the $F = 3$ rate.

Given measured intensities and atom numbers, the model then makes absolute predictions of the on- and off-axis count rates observed, and is typically within a factor of 3 of the observations, limited mainly by uncertainty in the absolute atom number and effective excitation rate. By examining the ratio of the on- and off-axis counters information can be gathered which is less sensitive to these uncertainties.

With this model now at our disposal, we can do a more careful analysis of the data revealed in Fig. 5.5. The random off-axis light in this case shows a slight dependence on F level, with the F′=2 count rate being 65% of the F′=3 rate. The model predicts that it be 48%. This reasonable agreement is most likely limited by the estimates

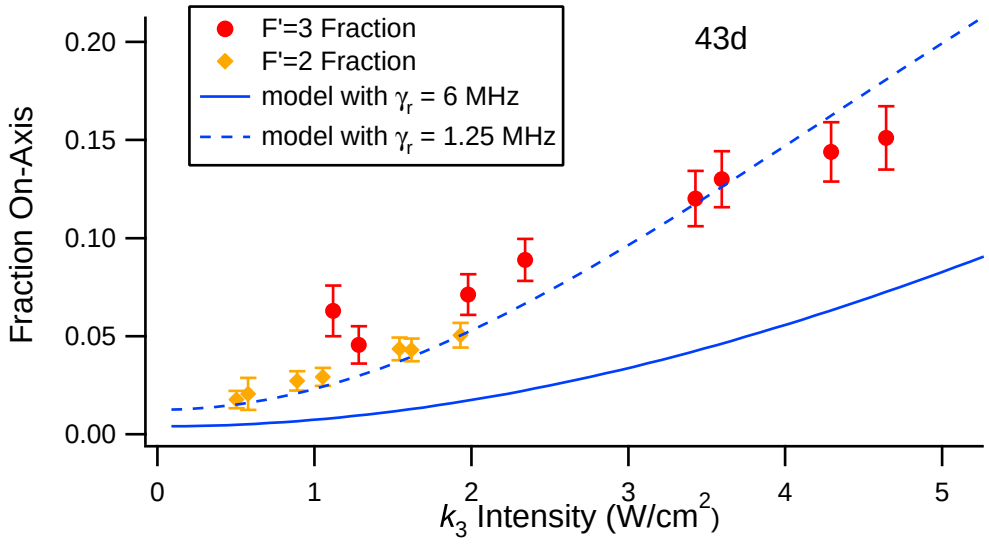

Fig. 5.7: Fraction of on-axis light as a function of intensity, with model predictions. The intensities and on-axis fractions for F′=2 data are scaled to reflect the reduced dipole matrix elements. The increased on-axis efficiency at higher intensity indicates the competition between four-wave mixing and decoherence processes.

made of the decoherent processes in the Rydberg state. The on-axis light in this figure has an observed 10:1 ratio for these two F levels. This is partly explained by a factor of $\sqrt{2}$ greater dipole matrix element for the $6p_{3/2}(\mathrm{F}' = 3) \rightarrow 5s_{1/2}(\mathrm{F}{=}2)$ transition as compared to the corresponding matrix element from the F′=2 state. Further accentuating this difference is the reduced deexcitation rate into the F′=2 state. There is a competition between the coherent deexcitation from the Rydberg state and the various decoherence processes that occur in the Rydberg state, and this further favors the larger Rabi coupling to the F′=3 state. From the combination of these effects the model predicts a ratio of 7.7, in reasonable agreement with the observations.

The large difference in phase-matched light on the $6p_{3/2}$ hyperfine peaks suggests there should be a strong dependence on the intensity of k_3. Figure 5.7 shows the on-axis fraction of the emitted light as the intensity of the k_3 laser is varied, for two

different hyperfine levels of the $6p$ state. The different dipole matrix elements for the two hyperfine levels are accounted for by scaling the F′=2 intensities by a factor of 0.48 and the on-axis fraction by 2. The fraction of light emitted into the phase-matched direction increases with increasing intensity, reaching a maximum of around 15% for $n = 43d$ and the intensities attainable here. This also shows that the four-wave mixing process is competing with decoherence, suggesting at higher k_3 powers the atoms are removed from the Rydberg state before they can undergo any decoherent process.

Included in Fig. 5.7 are two different model predictions. One for the observed transition broadening of $\gamma_{rp} = 6$ MHz, the other for a narrower broadening of $\gamma_{rp} = 1.25$ MHz. Clearly the model prediction is quite sensitive to the assumed broadening of the $r - p$ coherence, and in fact favors a narrower linewidth than was deduced from the off-axis spectroscopy. This discrepancy could suggest a narrower transition linewidth than observed, a larger number of atoms or smaller interaction region than calculated, or a fault of the model in its treatment of the broadening mechanisms. Despite this discrepancy, the model is shown to reproduce the key features of the four-wave mixing process. Additionally, the development and testing of this model has given us additional insight into how the four-wave mixing process can be optimized.

5.5 Detuned Four-Wave Mixing

Both our model of the four-wave process and our examination of the effectiveness of four-wave mixing suggest that decoherence processes in the Rydberg state are an essential factor in the system evolution. The coherent process of four-wave mixing must be competing against some decoherence mechanisms present in the Rydberg state. It follows that the reduction of these mechanisms in the Rydberg state should result in an increased amount of the light being emitted into the phase-matched direction.

One means of attempting to reduce the decoherence is by lowering the population in the Rydberg state. There are several decoherence processes, such as superradiance or atom-atom interactions, whose rate would vary with the population of the Rydberg state. Thus, reducing the population of the Rydberg state should effectively limit decoherence and increase the efficiency of the four-wave mixing process.

In order to test this hypothesis, we reduced the Rydberg population by detuning the excitation from the Rydberg state. A process that is on resonance with the three-photon transition to the $6p_{3/2}$ state while detuned from the Rydberg state should reduce the decoherence while maintaining the four-wave mixing process. Fig. 5.8 shows the results from our experimental procedure used to investigate the dependence on Rydberg state detuning. Here the stimulated emission probe k_3 was detuned 32 MHz above the $28d_{5/2}$-$6p_{3/2}$ F$'$=3 transition and stabilized at a constant frequency. Then the k_2 frequency is varied across the Rydberg state.

This process results in two seperate resonant processes. The first, labeled A, occurs when the excitation lasers are on resonance with the Rydberg state, giving significant Rydberg populations. In this case the Rydberg atoms are transferred off-resonantly to the $6p_{3/2}$ state at a slow rate. A large amount of off-axis light is produced in this process, but very little phase-matched light. The second case, labeled B and examined further in the inset, occurs when the excitation lasers are detuned from the Rydberg state, but a three-photon process is on resonance to the $6p_{3/2}$ state. Here there is very little Rydberg population, and hence only a small amount of off-axis light, while the fraction of phase-matched light increases dramatically. The laser frequencies and detunings involved in these two processes are also illustrated in Fig. 5.9.

For the case of 32 MHz detuning, as shown in fig. 5.8, the fraction of phase matched light reaches 50% of the total $6p-5s$ emission. This experiment was repeated for various two-photon excitation detunings, always adjusting the frequency of the deexcitation

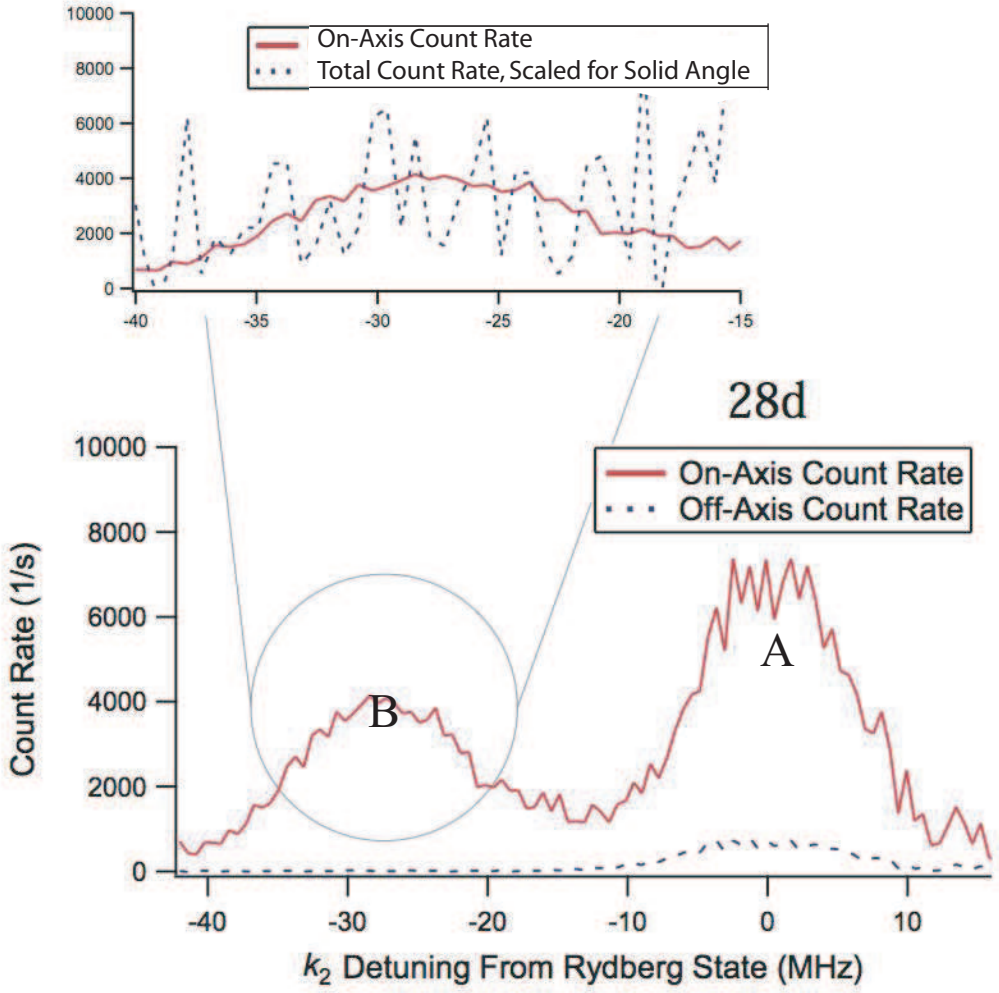

Fig. 5.8: Count rates in on- and off-axis counters as a function of the excitation frequency, showing both the non-resonant 5s-nd excitation (left peak and inset) and resonant Rydberg state excitation with off-resonant deexcitation to the 6p state. The k_3 laser was held 32 MHz above the Rydberg-6p transition. The inset scales the off-axis count rate by the solid angle to show the total amount of light emitted. In this case the amount of on-axis light is approximately equal to the total amount of light in all other directions.

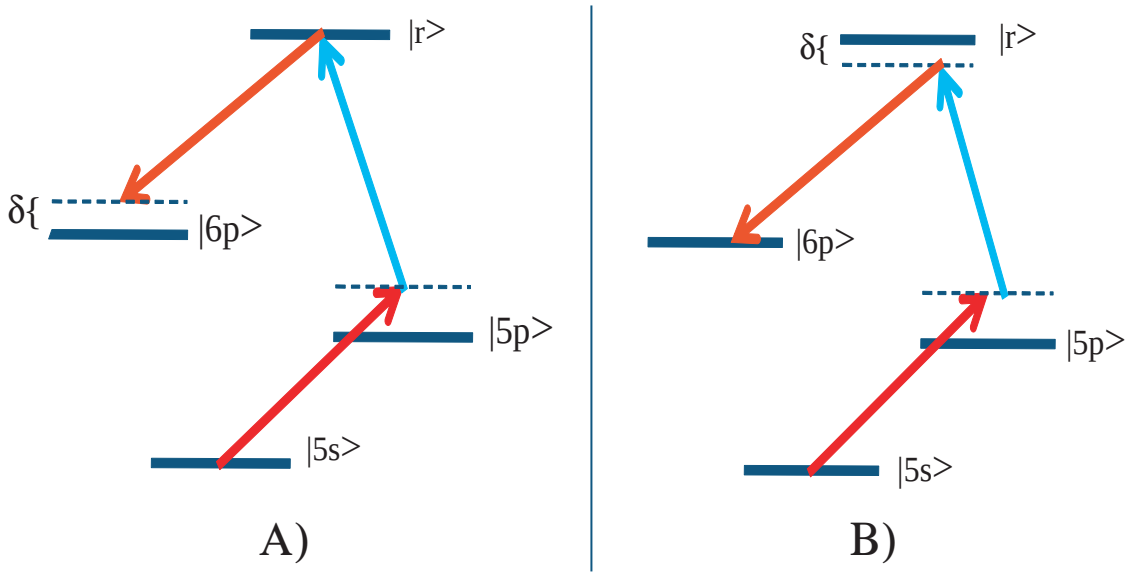

Fig. 5.9: Illustration of the two excitation processes resulting from our detuned four-wave mixing scheme. The frequency of the deexcitation laser is kept constant while the excitation frequency is varied. In A) the excitation lasers are on resonance to the Rydberg state, creating a large Rydberg population, while the deexcitation laser is detuned. in B) the excitation lasers are detuned, but the three-photon process is on resonance to the $6p_{3/2}$ state.

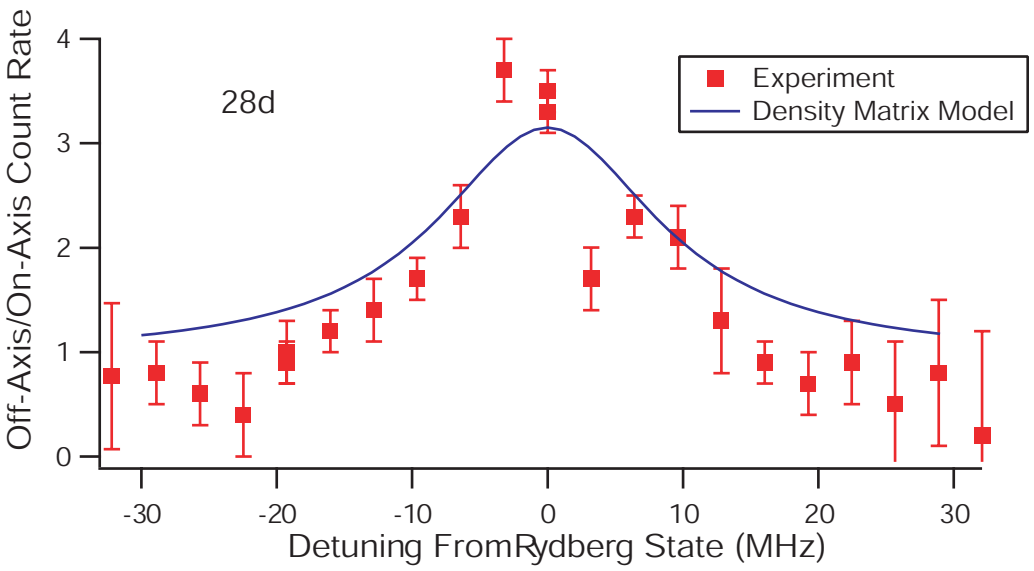

Fig. 5.10: The ratio of off-axis counts to on-axis count rate measured as a function of detuning from the Rydberg state. Zero on this plot corresponds to perfect phase matching. The efficiency of the phase-matching process is optimized when detuned from the Rydberg state.

laser to maintain three-photon resonance. The resulting ratio of off-axis light to on-axis light is shown in Fig. 5.10. When near resonance with the Rydberg state, the fraction of light emitted into the phase-matched direction is about 20%, while detuning from the resonance increases this fraction to up to 50% of the total light. This trend is matched well by the model, as shown in the figure.

5.6 Discussion

We have demonstrated continuous wave phase-matched four-wave mixing using Rydberg states. The directional emission is promising for studying novel quantum effects in blockaded atom clouds. The dependence of the phase-matched light on geometry, power, and detuning is well explained by a simple density matrix model, demonstrating

a good understanding of the system. With the process of four-wave mixing having been shown to be experimentally realizable, it represents an excellent means to generate a single photon source.

In order to generate an ideal single photon source, there are still several considerations that need to be addressed. As was observed in the experimental data and the model, there is a decoherence in our system that limits the effectiveness of the four-wave mixing process. This was improved upon by detuning from the Rydberg state, but it remains unclear what this mechanism is. The data presented here was all obtained under weak excitation conditions where Rydberg-Rydberg effects should be minimal. While it has been shown in Chapter 4 that superradiance will cause additional decoherence, this still does not provide the amount of decoherence we have observed, indicating there is an additional source of decoherence which we do not fully understand.

Effective Rydberg blockade requires the excitation to be on-resonant with the Rydberg state. This would prevent the possibility of using our detuned scheme to optimize the efficiency of the process. However, this efficiency problem should be eliminated when single atom excitation is achieved. Under blockade conditions Rydberg-Rydberg and superradiant decoherence mechanisms are predicted to be virtually eliminated. Thus efficient four-wave mixing should be possible even while resonantly driving the excitation process.

Finally, using phase-matched four-wave mixing as a single photon source will eventually require efficiency while exciting a very small region. In order to observe the phase-matched process in a small volume, we have focused the 480 nm and 1015 nm beams to 12 μm. This results in a effective volume of $\sim 10^{-8}$ cm^3, which could be blockaded for reasonable n-levels [Walker and Saffman, 2008]. When using the focused beams, phase-matching was again achieved for the various n-levels, with the same de-

pendence on F′ level, k_3 intensity, and detuning from the Rydberg state. The maximum percentage of light achieved in the phase-matched direction was reduced to below 1%, as expected from Eq. 5.7 since the relevant factor N_e/w^2 was reduced by a factor of 40. In the future, this could be improved by increasing the density of the sample [Sebby-Strabley *et al.*, 2005], allowing efficient phase-matching while also making possible a full dipole blockade, leading to a single photon source.

6. EXPERIMENTAL TECHNIQUES

6.1 Introduction

One of the most interesting properties of Rydberg atoms is their very large atom-atom interactions leading to the concept of blockade. In order to understand and explore the effect of these interactions on optical excitation of Rydberg atoms, it was necessary to develop a number of new experimental techniques. In order to help the reader follow the important results presented in the next two chapters without digressions, I will first present here the necessary background information on the methods used. This chapter can be thought of as a "toolbox", containing descriptions of the important tools which will be used in Chapters 7 and 8.

The first tool is the application of microwaves to the Rydberg atoms, which I will discuss in Section 6.2. These microwaves are used to excite Rydberg atoms from their initial state to a nearby state. Verification and optimization of the microwave coupling can be accomplished by examining the resulting Autler-Townes splitting of the Rydberg state. We typically see microwave Rabi frequencies of ∼25 MHz, completely mixing the Rydberg states. With this technique we can allow first order dipole-dipole interactions, the importance of which we will see in Chapter 7.

Section 6.3 will discuss our method for limiting the volume of Rydberg excitation to a very small size. By crossing the excitation beams we can potentially limit our excitation volume down to $\sim 8 \cdot 10^3$ μm^3. This volume is nearly small enough to enable

a complete blockade (as discussed in Chapter 7), though we currently work with larger volumes for better signal to noise. With the reduction of the excitation beam sizes the Rabi frequencies are drastically increased. Included here is the importance of this effect as a spatially selective ac Stark shift.

Essential to any attempt to investigate the effects of atom-atom interactions on Rydberg excitation is an accurate measurement of the number of Rydberg atoms and their excitation rate. Section 6.4 describes our technique of pulsed Rydberg excitation. This pulsed scheme gives us an experimental measure of the excitation and stimulated emission rates, with the photon count rate proportional to the number of Rydberg atoms. In addition, the pulsed excitation allows investigation into the importance of collisional and ionization effects. Ionization is observed to be a significant problem for $|nd\rangle$ states, motivating the use of $|ns\rangle$ states for further investigations.

6.2 Microwave Coupling

Microwave coupling between Rydberg states is an emerging tool in ultracold atomic physics. Microwaves have recently been used to induce resonant energy transfer through the ac Stark shift [Bohlouli-Zanjani *et al.*, 2007], and directly couple nearby Rydberg states [Afrousheh *et al.*, 2004] [Han and Gallagher, 2009]. Rydberg atoms have very large oscillator strengths for nearest neighbor transitions ($\sim$ -10 to 10 for the principal quantum numbers accessible in our lab), and hence are very sensitive to microwaves. Since microwaves are stable and easily attained, they have become an excellent possibility for the enhancement of Rydberg-Rydberg interactions.

In our lab we make use of an HP 83640A synthesized sweeper, which can output microwave frequencies up to 40 GHz. Since the spacing between adjacent Rydberg levels increases at smaller principal quantum number, this frequency sets a lower limit

on the Rydberg levels which can be coupled using our microwave source. The energy spacing from an ns state to an np state is larger than from nd to $(n-1)f$, so the lowest levels which we can couple are the $47s \rightarrow 47p$, or the $40d \rightarrow 39f$. The approximate frequencies necessary can be determined from the Rydberg level energies (described in Appendix A), and optimized by maximizing the Autler-Townes splitting as described later in this section.

The microwave generator is able to output up to 5 mW of power, but it is complicated to determine what fraction of that power reaches the atoms. The microwaves are transmitted to a horn which is pointed at the vacuum chamber. A large loss in power results from the microwaves being unable to enter the vacuum chamber, as there is significant attenuation due to the comparable size of the vacuum chamber windows (5 cm) and the incident microwave wavelength (1-4 cm). Since the exact loss in power is difficult to determine, the most accurate measure of how much power actually reaches the atoms can be obtained from the observed Autler-Townes splitting, as discussed below. The wavelength and oscillator strength for the transition are well known, so the intensity of the microwaves can be determined from the observed Rabi frequency. Estimating the waist to be the radius of the entrance window, the Autler-Townes splitting would correspond to only $\sim$0.1 mW of power reaching the atoms. From the geometry and the propagation of the microwaves from the horn to the chamber, we could expect as much as 1 mW of power to reach the atoms. This has not been a concern due to the small amount of power needed, but could most likely be improved with a different transmission cable and more careful alignment of the emission horn.

If the microwave frequency is set very close to an atomic transition with a Rabi frequency very large compared to the detuning, an Autler-Townes splitting can be observed. This process has been well described elsewhere [Autler and Townes, 1955], and only an overview is given here. At high intensities, it is most appropriate to consider

the atom and microwaves in a dressed picture. When the coupling is very large, this results in the appearance of two states which are superpositions of the initial states:

$$|\Psi\rangle = \frac{|s\rangle \pm |p\rangle\, e^{-i\omega t}}{\sqrt{2}}. \tag{6.1}$$

These states are separated in energy by twice the microwave Rabi frequency, $2\epsilon_\mu$. This process is depicted in Fig. 6.1 for the case of $ns \rightarrow np$. Since both of the new coupled states $|\Psi\rangle = |s\rangle \pm |p\rangle\, e^{-i\omega t}$ (labeled $|s+p\rangle$ and $|s-p\rangle$) have some component of the $|s\rangle$ state, they can be excited by light from the intermediate $|5p\rangle$ state.

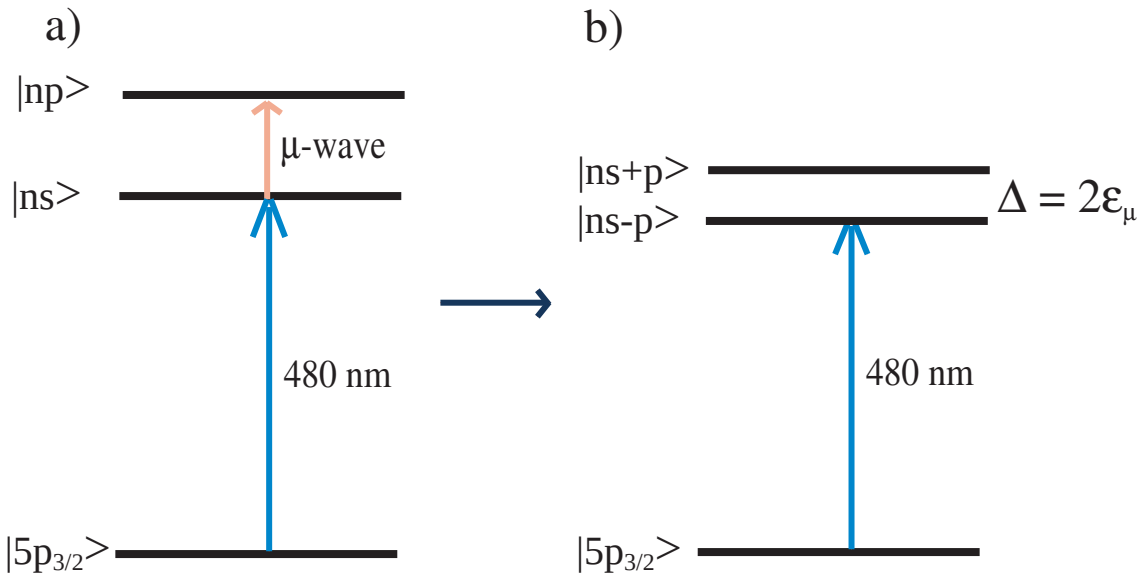

Fig. 6.1: a) Microwaves are applied on resonance from the ns Rydberg state to the np state. b) Showing the dressed states after coupling, where now the states $|s+p\rangle$ and $|s-p\rangle$ are split by twice the microwave Rabi frequency, ϵ_μ.

Tuning of the microwaves into resonance can be done by maximizing the splitting of the two states, and is accurate to within a few MHz using this technique. Figure 6.2 shows a typical scan of the excitation frequency across the Rydberg resonance at $60d$ for several microwave power levels. The splitting between the two peaks of $|d+f\rangle$ and

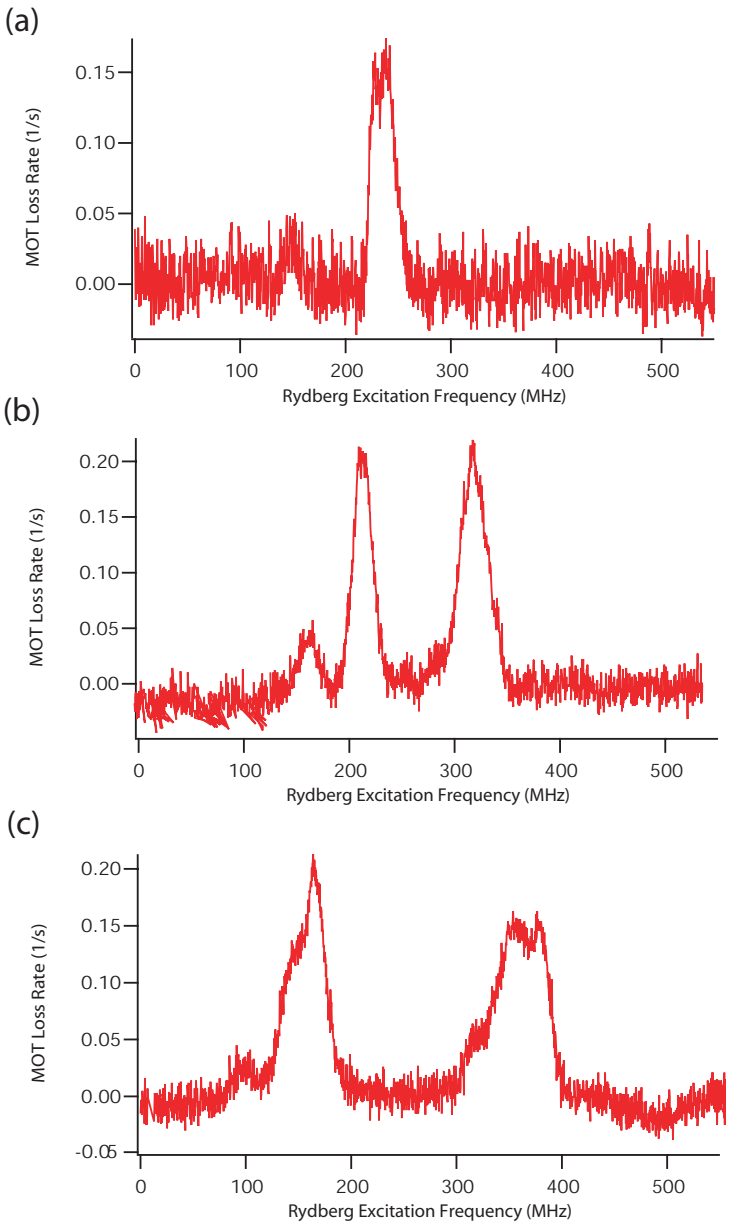

Fig. 6.2: The experimental observation of the Autler-Townes splitting for microwaves on resonant from the $|60d\rangle$ to $|59f\rangle$ levels with a) no microwaves, b)weak microwaves, and c) full microwave power. Here the two states $|d+f\rangle$ and $|d-f\rangle$ are split by the microwave Rabi frequency of up to 200 MHz. The fine structure of the $|d\rangle$ state can just be observed.

$|d - f\rangle$ can be easily measured, giving an excellent measurement of the microwave Rabi frequency. In this case the Rabi frequency was 100 MHz for the highest power level. This splitting decreases at lower principal quantum numbers, as the coupling strength between these levels goes down as $\sim n^2$ and the power is more heavily attenuated by our apparatus. For the data shown in Chapter 8, the microwaves were resonant with $47s \rightarrow 47p$. This resulted in a $\sim$25 MHz splitting, which is still excellent coupling of the Rydberg states.

The use of microwaves to couple Rydberg atoms is fairly simple in both theory and implementation. As we will see in Chapter 7, this provides a way to adjust the strength of atom-atom interactions over a large range, giving us an excellent means by which to observe any effect that these interactions may have upon Rydberg excitation.

6.3 Small Volume Excitation

The atom-atom interaction energy discussed in Chapter 7 will decrease with the separation of the atoms. In light of this, if all atoms involved in the excitation process are to see a significant interaction from any one atom excited, they must exist in a tightly confined spatial region. The simplest way to achieve small excitation volume is to orient the two excitation lasers perpendicular to each other with very small waists. Unfortunately, this scheme is not compatible with four-wave mixing as phase-matching is not possible. However, in order to make the proof of principle experiment, we have temporarily switched to this geometry, as shown in Fig. 6.3. In the future, we can return to a four-wave mixing geometry and still accomplish blockade.

In the geometry used here, the 480 nm beam can be focused to as small as 13 μm, and the 780 nm beam to as small as 12 μm. In order to align these two beams optimally, there are three important steps. First, the blue beam is centered on the

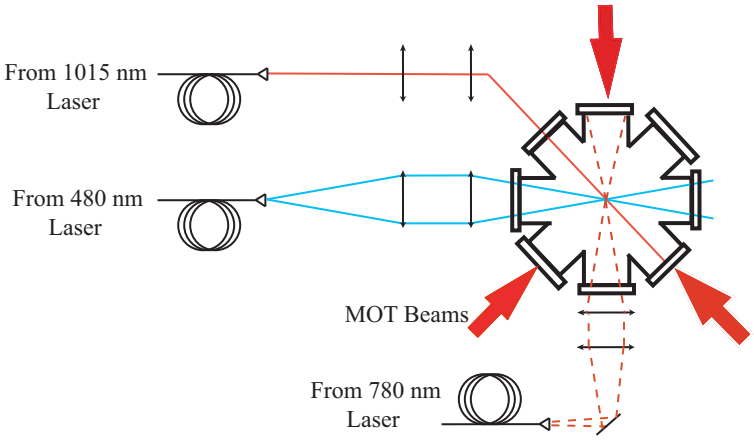

Fig. 6.3: The experimental setup used to establish very small volumes of excitation. The 480 nm and 780 nm excitation beams are temporarily oriented perpendicular to each other, and can be focused as tightly as 12 μm waists, allowing an excitation volume as small as $7.8 \cdot 10^{-9}$ cm^3, though typically larger volumes are used for increased signal to noise.

MOT cloud, and the position is imaged directly with a CCD camera. Next, the 780 nm beam is aligned onto the blue beam to maximize the photon count rate, optimizing their overlap. Finally, the position of the focusing lens for the two beams is scanned using a micrometer, and the counts minimized, making the overlap region at the focus of the two beams. This should allow an excitation volume as small as $7.8 \cdot 10^3$ μm^3, calculated simply by $\frac{4\pi}{3}\omega_{780}^2\omega_{480}$. This is approaching a size that could be blockaded for the interaction strengths discussed in Chapter 7 assuming a transition linewidth of 5 MHz. For the purpose of increasing signal to noise during the proof of principle experiments, we have moved the focusing lens in the 780 nm laser optical train to overlap the 480 nm beam at a larger waist of $\sim$50 μm.

With the beams focused to small waists, the Rabi frequencies are large, and calculated to be $\epsilon_{480} \sim 10$ MHz and $\epsilon_{780} = 550$ MHz at the waists used with the maximum powers available. A consequence of the large Rabi frequencies of the focused beams is that the ac Stark shift caused by the 780 nm beam becomes significant. The 780 nm beam is still locked Δ=470 MHz above the $5s_{1/2}F = 2$ to $5p_{3/2}F = 3$ transition, so the ac Stark shift, given by $\Delta_{AC} = \frac{\epsilon^2}{\Delta}$ can reach hundreds of MHz.

For atoms in the F=2 ground state the 780 nm laser is 470 MHz blue detuned, and the atoms see a spatial distribution of very large ac Stark shifts and a repulsive potential. We also have the ability to put atoms into the F=1 ground state through the use of a spatial Dark SPOT MOT, as described in [Sebby-Strabley, 2004]. Atoms in the F=1 ground state are 6.3 GHz red detuned, and have a much smaller ac Stark shift and an attractive potential. We have the ability to create Rydberg atoms from either of these ground states, and do so based on the desired excitation rates and ac Stark shifts.

For excitation to a $|d\rangle$ Rydberg state, we excite from the dark F=1 ground state, and thus have a low scattering rate and an attractive potential. Here we use the

full power available in the 780 nm beam, giving a 550 MHz Rabi frequency. The maximum ac Stark shift is then 48 MHz, and the two-photon Rydberg Rabi frequency $\epsilon_2 = \frac{\epsilon_{480}\epsilon_{780}}{\Delta} \sim 1$ MHz. However, as will be discussed in Section 6.4, excitation to $|d\rangle$ Rydberg states results in high collision and ionization rates, which makes understanding the system more difficult. As a result, we have focused our attention on the $|s\rangle$ states. Unfortunately, these states have $|5p\rangle \rightarrow |ns\rangle$ oscillator strengths almost an order of magnitude lower than the $|d\rangle$ states. In order to keep our two-photon Rabi frequency close to 1 MHz, we instead excite out of the F=2 ground state, with a highly attenuated 780 nm laser power.

Here, we have measured that ϵ_{480}=600 kHz and ϵ_{780}=183 MHz by observation of the ac stark shift of 71 MHz and a two-photon Rabi frequency of 225 kHz (see Section 6.4). Using the measured powers, the waist of the beams can then be extracted, giving 50 μm for the 780 nm beam and 75 μm for the 480 nm beam. The 780 waist is quite close to the expected value, but the 480 waist is significantly larger than expected. Further work will be needed to assure this waist size through external measurement, and a new optics train is being designed. Using the values for the waists estimated here, this would give an interaction volume of $2\pi\omega_{780}^2\omega_{480} = 1.9 \cdot 10^5$ μm^3.

Using the F=2 ground state creates two sources of possible concern. The first is the large scattering rate Γ_s of the $5p_{3/2}$ state. This scattering rate is approximately given by:

$$\Gamma_s = \frac{\epsilon_{780}^2}{\Delta^2}\Gamma_{6p}, \tag{6.2}$$

where Γ_{6p} is the natural linewidth of the 6p state. With our Rabi frequency and detuning, this scattering is $\sim 6 \cdot 10^6$ /s. While this is a high scattering rate, it would still not dominate the decoherence of the system, with measured transition widths of $\sim$5 MHz. This fast scattering does optically pump the ground state atoms out of the

F=2 ground state. To make this optical pumping negligible, we have overlapped a repumping beam on the 780 nm optical train which scatters from the F=1 state at $\sim 1 \cdot 10^7$ /s.

The second concern is the large repulsive potential created by the 780 nm beam, as this could decrease the density of atoms inside the excitation volume. This effect is reduced by pulsing the 780 nm beam with low duty cycles. For the pulse lengths of $\sim$20 μs used in our experiment, the maximum movement of the atoms is calculated to be only $\sim 2\ \mu m$ during a pulse. This is followed by 500 μs without the potential, and so the excitation region should not be significantly depopulated. As we will see later in this section, there are other important benefits of pulsed excitation.

One important advantage of the ac Stark shift is that it can be used as an additional spatial selection for the atoms, similar to the recent proposal of [Yavuz *et al.*, 2009]. A typical scan for excitation from the F=2 ground state to the 47s state (with and without microwave coupling) as the 480 nm laser frequency is varied is shown in Fig. 6.4. In this case the ground state energy is shifted up by the ac Stark shift, and so a lower frequency is needed to excite Rydberg atoms in the most intense portion of the beam. Due to the distribution of intensities across the Gaussian profile of the 780 nm beam, atom frequencies are shifted based upon their location in the beam. Thus, choosing a particular frequency of excitation gives spatial selection inside the 780 nm beam. For example, selection from the area labeled "Deep" would excite only those atoms with an ac Stark shift greater than $\sim$60 MHz assuming a 5 MHz transition linewidth. This corresponds to selecting only the middle $\sim$20 μm from a 50 μm waist. This will allow an even smaller excitation volume for dipole blockade in the future if the waist of the 780 nm beam is further reduced.

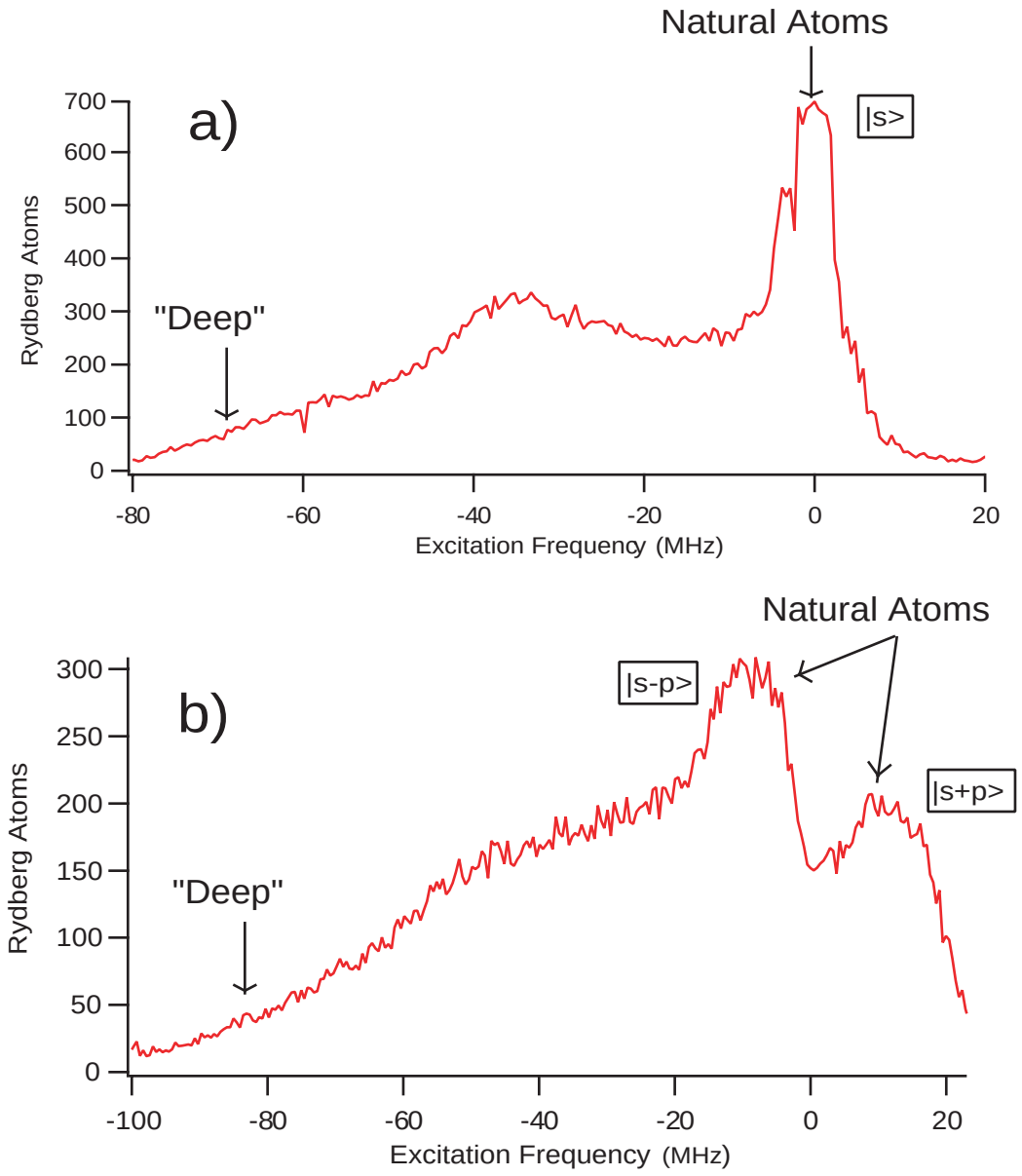

Fig. 6.4: Rydberg atoms are created over a large range of 480 nm frequencies due to the spatial variation of the ac Stark shift from the 780 nm beam. This gives extra spatial selection by choosing the largest shift, and hence the most intense part of the 780 nm beam. This effect is seen a) without microwaves, and b)with microwave coupling.

6.4 Pulsed Excitation Technique

I now turn our attention to the means by which we calculate the excitation rate and the number of Rydberg atoms created. In order to experimentally determine these parameters, we turn to a pulsed excitation scheme. Here the 780 nm excitation laser is pulsed at a 2 kHz repetition rate with a variable duty cycle by control of an AOM. The photon counter is triggered with the start of each pulse with excellent timing stability, and so the counts collected from many of these pulses can be averaged together. The result of averaging 300,000 such scans at $|47s\rangle$ is seen in Fig. 6.5.

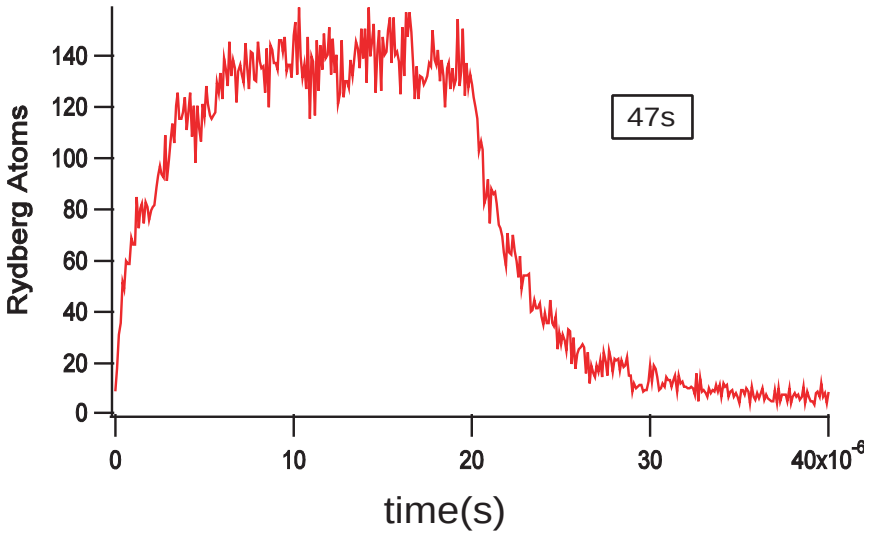

Fig. 6.5: The photon count rate is recorded vs the time after the start of the excitation pulse, and averaged for many cycles. The number of Rydberg atoms is proportional to the equilibrium count rate, and the rise/fall times of the signal are experimental measures of the excitation and stimulated emission rates.

The rise and fall time of the photon count rate gives an experimental measure of the excitation and stimulated emission rates. In the absence of blockade, the three level system can be described by:

$$\begin{aligned}
\frac{dN_g}{dt} &= R_2(N_r - N_g) + \Gamma N_{6p} \\
\frac{dN_r}{dt} &= R_2(N_g - N_r) - R_3(N_r - N_{6p}) \\
\frac{dN_{6p}}{dt} &= R_3(N_r - N_{6p}) - \Gamma N_{6p}, \qquad (6.3)
\end{aligned}$$

and can be simplified since the decay rate from the $|6p\rangle$ state is much faster than R_3. Solving the resulting two level system results gives:

$$N_r = \frac{R_2}{R_3}(1 - e^{-(2R_2+R_3)t}). \qquad (6.4)$$

The observed rise time is then equal to $\frac{1}{2R_2+R_3}$ and fall time (in the absence of excitation light) is equal to $\frac{1}{R_3}$. This model is accurate in the absence of blockade, so low densities of ground state atoms are used. We have examined these rates both with and without microwave coupling, and seen that the microwave coupling reduces the effective rates by $\sim$2, consistent with our expectations. The stimulated emission Rabi frequency can be determined from the rate and the transition linewidth, and agrees reasonably well with the calculated value. However, the excitation Rabi frequency is more than a factor of three lower than calculated. Since the 780 nm Rabi frequency can be verified by the ac Stark shift observed, the Rabi frequency of the 480 nm transition is lower than expected. This could be due to poor spatial alignment of the beams, or a larger waist than expected in the overlap region. Further work will be needed in the future to verify the waist size and spatial overlap.

The number of Rydberg atoms created can be determined from the observed photon count rate using the solid angle, collection efficiency, and stimulated emission rate. The 420 nm photon count rate is proportional to the number of Rydberg atoms created, giving excellent means to observe blockade effects. However, there are two main concerns

which could affect our ability to easily understand the resulting data: superradiance and collision induced ionization.

We have already seen from Chapter 4 that superradiance can be an important effect in considering Rydberg atom systems. We have now significantly altered the excitation volume and Rydberg atom number, and so we must investigate anew the possibility of superradiance under these conditions. The reduced size of the excitation region will greatly increase the spatial factor shown in Eqn. 4.11, as the condition for the wavelength to be much larger than the sample size is satisfied for wavelengths as small as $\sim$30 μm. This would allow superradiance down to principal quantum numbers of n$\sim$16, and could allow superradiance to play a critical role. However, the superradiant rate is enhanced by the number of atoms involved, as seen from Eqn. 4.2. In the small excitation volume used here, only $\sim$500 atoms are excited, as opposed to the $\sim 10^5$ atoms in the excitation scheme used in Chapters 3 to 5. As a result, superradiant rates are predicted to be an order of magnitude slower than spontaneous decay and black-body, which would not greatly effect the system.

Collision induced ionization and subsequent electron trapping have been shown to greatly affect the Rydberg population in a number of experiments [Li *et al.*, 2004] [Walz-Flannigan *et al.*, 2004]. The effect of ionization is often difficult to differentiate from a blockade signal [Vogt *et al.*, 2007], and so it is important to look for this effect in our sample. For excitation to $|d\rangle$ states, the photon count rate decreases after an initial rise, as seen in Fig. 6.6. After verifying that depletion of the number of atoms in the MOT is not responsible, this suggests that the production of Rydberg atoms is being inhibited by another process at times greater than $\sim$2 μs.

One possible explanation for this decrease is the accumulation of ions in the excitation region. It is possible that there is sufficient ion production to cause an electron trap [Killian *et al.*, 1999], causing avalanche ionization and preventing further Rydberg

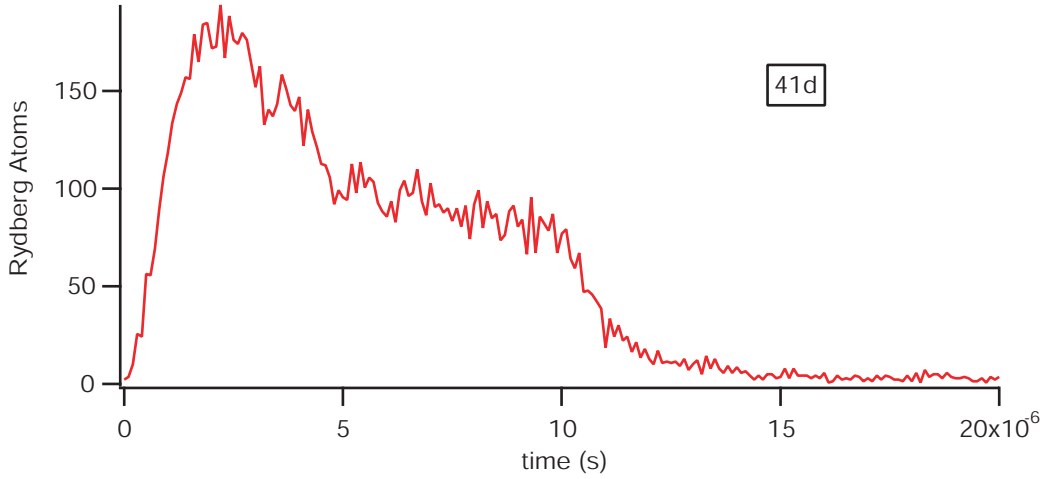

Fig. 6.6: The number of Rydberg atoms during the excitation pulse for the $|40d\rangle$ state. Here the number of Rydberg atoms declines from its initial value, an indication of ionization which is absent during excitation to the $|47s\rangle$ state.

excitation. In addition, it was recently shown that $|d\rangle$ states ionize on a significantly faster timescale than $|s\rangle$ states [Li *et al.*, 2005]. Thus, to further illuminate this effect, we compared the ionization signatures from the $|s\rangle$ and $|d\rangle$ states, and saw no sign of the inhibited Rydberg atom production at long times for the $|s\rangle$ states, which resulted in a steady state Rydberg level as seen in Fig. 6.5. Coupling the $|40d\rangle$ to $|39f\rangle$ with microwaves caused the effect of ionization to be even more pronounced, as shown in Fig. 6.7. The dropoff in Rydberg number for the $|d-f\rangle$ state is remarkable, most likely due to dipole interactions increasing the collisional ionization rate.

The effect of ion formation was further investigated by varying the time between excitation pulses. Free electrons are fairly fast moving, but would take ~ 100 μs to dissipate [Killian *et al.*, 1999]. Figure 6.8 shows the creation of $|d-f\rangle$ Rydberg atoms for several different dissipation times between excitation pulses. As can be seen, the initial Rydberg population decreases after an initial rise with a long dissipation time, while for small dissipation times the population is consistently lower. This gives further

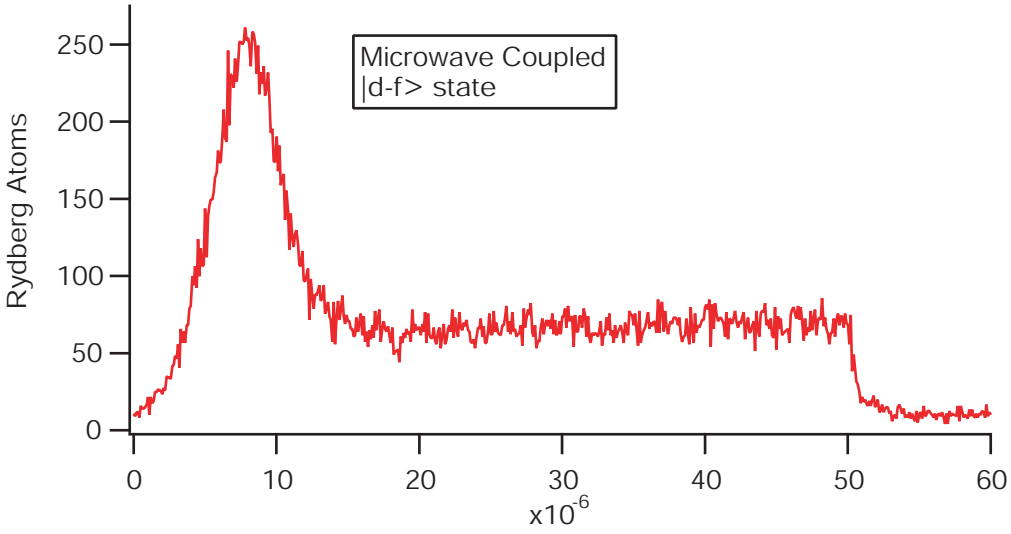

Fig. 6.7: The number of Rydberg atoms during the excitation pulse for the $|40d - 39f\rangle$ state. Here the number of Rydberg atoms declines dramatically after $\sim$10 μs, though the excitation pulse continues for 50 μs. This is most likely a result of increased ionization rates.

evidence that stray ions are prohibiting excitation, as the signal is permanently reduced if there is insufficient time to allow ions to dissipate and neutral atoms to repopulate the excitation region.

To eliminate possible effects from ionization, we have chosen to perform excitation to the $|s\rangle$ Rydberg states, and limit our excitation time to 20 μs with a 480 μs between pulses. Under these conditions, we see no evidence of ionization effecting the number Rydberg atoms. A similar choice of the $|s\rangle$ states was made in a similar experiment at even higher densities to avoid ionization [Heidemann *et al.*, 2007].

Using the techniques described in this chapter, we now have the ability to microwave couple nearby Rydberg states, localize excitation to a small volume, and characterize the excitation rate and number of Rydberg atoms in the sample. All of these tools will be essential in examining the effects of atom-atom interactions in Chapter 8.

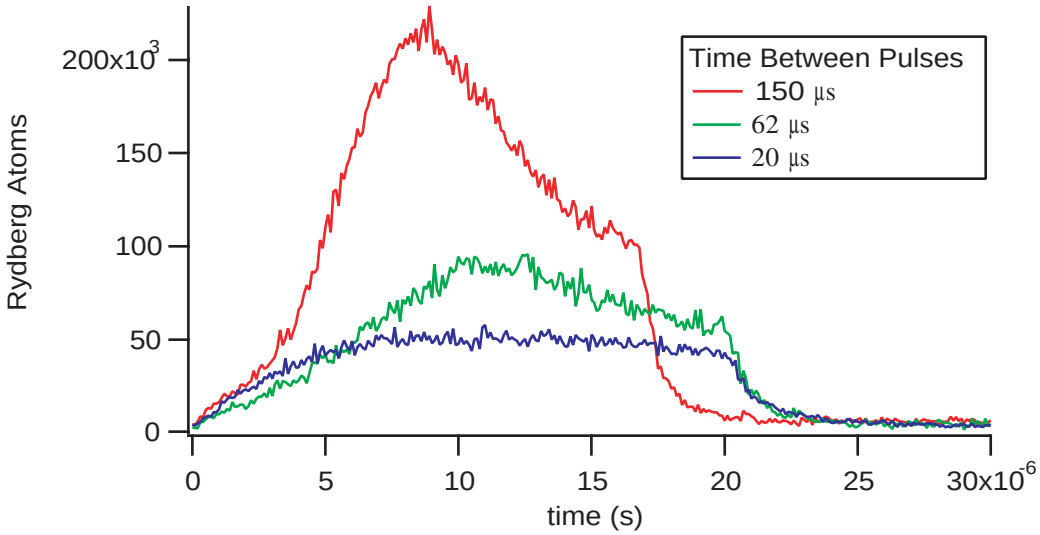

Fig. 6.8: After excitation to the $|d - f\rangle$ state, the time between excitation pulses is varied. For long delay times, a large initial Rydberg population is achieved, followed by a reduction. For smaller times between pulses, the overall Rydberg population becomes smaller and approximately level, indicating that ions formed have insufficient time to dissipate between excitation cycles.

7. ATOM-ATOM INTERACTIONS

7.1 Introduction

The presence of large dipole moments, and hence large atom-atom interactions represents one of the major motivations driving the study of Rydberg atoms. The concept of using the Rydberg dipole-dipole interaction to prevent subsequent excitation was first proposed by [Jaksch *et al.*, 2000]. The premise depends upon the idea that if the energy shift due to atom-atom interactions is larger than the excitation linewidth, the excitation of one atom will result in nearby atoms being too far off-resonant with the laser light to be excited. The basic physics of this idea is shown in Fig. 7.1, where the excitation of a second atom is detuned from resonance, and hence suppressed. This Chapter will give an overview of the subject of Rydberg blockade and investigate the particular expectations for excitation scaling and interaction strengths relevant to our experiment.

The distinction between the more general term "suppression" and the very specific "blockade" is an important one, and sometimes overlooked in the field. Even with a very large excitation volume, large atom-atom interactions and high atom densities will result in suppression. Let us assume that for a particular atom, there are other atoms whose spatial separation from the excited atom results in a large energy shift. However, there would also exist atoms far enough away from the initial atom that the shift in their excited energy would be quite small, allowing their excitation. As a result, the

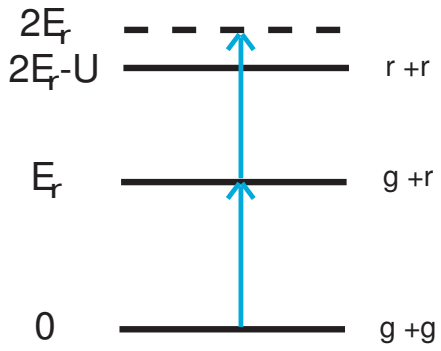

Fig. 7.1: The energy levels of two atoms being excited to Rydberg states are shown. Here the excitation of the first atom is on resonance, but excitation of the second atom is detuned by the interaction energy U_{dd}.

overall number of atoms excited would be fewer than in the absence of interactions, but many atoms could still be excited overall. By definition, the excitation of these atoms would be "suppressed", but the term "blockaded" is reserved for the regime where only one atom could be excited within the sample. In addition, it is possible to have interactions with certain "zeros", which would result in an ineffective blockade [Walker and Saffman, 2005]. This distinction is important because promising applications such as quantum computation or single photon sources would require "blockade", and not merely "suppression".

Related to the idea of blockade is the commonly used term "blockade radius". This refers to the distance away from an excited atom the second atom would need to be for the energy shift to become smaller than the transition linewidth. The excitation of atoms at distances closer than this radius would be greatly suppressed. Thus, a large sample with suppression can be thought of as a collection of individually blockaded spheres, each with a radius R_b. The number of atoms within this locally blockaded volume will determine the level of suppression in the sample as a whole.

Since the time of Lukin's proposal, this scheme has been investigated by sev-

eral groups, with many promising advances. In particular, suppression of excitation in a large Rydberg sample has been shown in several contexts [Singer *et al.*, 2004] [Tong *et al.*, 2004] [Cubel Liebisch *et al.*, 2005] [Vogt *et al.*, 2006] [Vogt *et al.*, 2007] [Heidemann *et al.*, 2007], and recently a genuine blockade between two nearby single atoms has been shown [Urban *et al.*, 2009], [Gaëtan *et al.*, 2009]. A complete blockade of a large number of atoms in a single site remains to be observed, but several promising realizations of this are being pursued, including the future work of this experiment, as discussed in Chapter 9.

As the work presented in Chapter 8 will involve a regime where suppression, but not blockade, is expected, Section 7.2 will develop the expectations for Rydberg atom excitation in this regime. The expected scaling of the Rydberg excitation in the limit of strong van der Waals blockade and large samples has recently been investigated by [Löw *et al.*, 2009]. I expand upon these universal scaling ideas, and generalize them the unique regime of our experiment covering where the atom-atom interactions first becomes significant. Our general theory allows a quantitative understanding of the interaction strength, which had not previously been considered.

The theory of atom-atom interactions will be explored in detail in Section 7.3. Since only a single Rydberg state is typically excited in our experiments, the dipole-dipole interaction is zero to first order. However, due to the large dipole moments and small energy defects, the Van der Waals interaction can still produce large interaction strengths. I will discuss the expected van der Waals interactions in our sample, and the expected blockade parameters for our experiment. Since these are often smaller than desired, I will also discuss a technique for creating larger atom-atom interactions using microwaves: resonantly coupling the initially excited state to a nearby state. This coupling to nearby Rydberg states enables a first order dipole-dipole interaction, and so increases our atom-atom interactions.

7.2 Scaling Laws

Understanding the expected scaling of Rydberg atom production under conditions of a strongly interacting, large volume gas is more complicated than it may appear upon initial consideration. The work of [Löw *et al.*, 2009] has recently described the expectations for a universal scaling law in this regime. Here I will clarify and expand upon these ideas for the case of microwave coupled states, where the atom-atom interactions are predicted to be large and will have a $\frac{1}{R^3}$ dependence. Additionally, the scaling law is generalized to be valid in the realm of weak interactions.

Essential to an understanding of the scaling laws in a strongly interacting gas is the idea of collective excitation [Heidemann *et al.*, 2007], where the effective Rabi frequency is enhanced by the number of atoms in a blockaded region according to

$$\epsilon_{2eff} = \sqrt{N_b}\epsilon_2 = \sqrt{\eta\frac{4\pi}{3}R_b^3}\epsilon_2 \tag{7.1}$$

where N_b is the number of atoms in the blockaded region, which is equal to the blockade radius R_b times the ground state density η.

In the strongly interacting gas described in [Löw *et al.*, 2009], it is assumed that a large number of atoms are inside a blockade sphere, resulting in power broadening dominating the linewidth of the transition. In this case, to be blockaded the atom-atom interactions must be equal to the effective Rabi frequency. For a three dimensional sample with resonant microwave coupling, this can be written:

$$\frac{C_3\beta}{R_b^3} = \sqrt{\eta\frac{4\pi}{3}R_b^3}\epsilon_2, \tag{7.2}$$

where β is a correction factor resulting from angular momentum degeneracies, as discussed in Section **??**. The important consequence of eqn. 7.2 is that the size of the blockaded volume in fact depends upon the density of ground state atoms and the

excitation rate according to

$$R_b = \left(\frac{C_3^2 \beta^2}{\epsilon_2^2 \eta \frac{4\pi}{3}} \right)^{1/9}. \tag{7.3}$$

Equation 7.3 shows that as the density or excitation rate is increased, the effective blockade radius will decrease, enabling more Rydberg atoms overall to be excited. This increase in Rydberg atom number does deviate significantly from a linear increase, with the number of Rydberg atoms produced equal to the number of blockade spheres within the excitation volume,

$$N_r = \frac{V}{\frac{4\pi}{3} R_b^3} = \frac{V \eta^{1/3} \epsilon_2^{2/3}}{(\frac{4\pi}{3})^{2/3} C_3^{2/3}}. \tag{7.4}$$

Unfortunately, we cannot currently attain high enough densities to verify this scaling over a large range, but this has been observed in a beautiful experiment by [Löw *et al.*, 2009]. However, several important aspects have been left out of consideration in that investigation. This scaling has been derived entirely with the assumption of a strongly interacting gas, and gives no insight into a gas with weak or zero negligible interactions. This is especially important to our experiment, which covers the very interesting transition between a weakly and strongly interacting gas. As we will see in Chapter 8, for low ground state densities the atom-atom interactions appear too small to noticeably suppress excitation. However, as the density is increased we transition into a regime where these interactions appear to suppress excitation. As such, the experiments conducted represent a "transition" regime between weak and strong interactions, and a more general scaling law which encompasses this transition regime is necessary.

Due to the large natural transition linewidth observed in our experiment and the relatively small number of atoms expected in a blockade volume (see Section 7.3), the minimum atom-atom interaction shift necessary for blockade in this case is not determined by the effective excitation Rabi frequency, but by the linewidth. When the

interaction strength between nearby atoms becomes larger than the effective linewidth of the transition, excitation will effectively cease. This would result in an increase in the number of Rydberg atoms with increasing density or excitation rate up to a certain maximum number (determined by the interaction strength), and then a steady state value regardless of further increases. In this case, the condition for blockade becomes:

$$\frac{C_3\beta}{R_b^3} = \Gamma, \tag{7.5}$$

where Γ is the transition linewidth.

Here the blockade volume, and hence the number of possible excitation sites, will be independent of the density or excitation frequency:

$$N_s = \frac{V}{\frac{4\pi}{3}R_b^3} = \frac{V\Gamma}{\frac{4\pi}{3}C_3\beta}, \tag{7.6}$$

where N_s is the number of excitation sites in the volume V. This equation will hold provided that the interaction strength is larger than the transition linewidth and the effective excitation Rabi frequency is not yet large enough to put us into the realm of a "strongly interacting" gas.

To generalize the idea of universal scaling laws for the transition between the realm where there is no blockade ($N_s \propto \eta$) and the onset of blockade (N_s constant), we use an interpolation for the number of excitation sites that is valid in the known extreme cases of negligible and strong blockade:

$$N_s = \frac{\eta V}{\sqrt{1 + (\frac{\eta\frac{4\pi}{3}C_3\beta}{\Gamma})^2}}. \tag{7.7}$$

It can be seen that this generalized equation for the Rydberg atom number obeys the correct scaling for the limits of the blockade. It is possible to find other interpolation functions that also agree with the known scaling at the limits. This particular function was chosen as a simple function which agreed well with the experimental data. Several

other functions with the appropriate limiting dependence have also been used, and resulted in less than a 20% change in the extracted parameters.

The relationship between the actual number of Rydberg atoms created and the number of available excitation sites depends upon the relative rates of the excitation and stimulated emission. This will be discussed in more detail in Section 8.3. The number of Rydberg atoms in this case is given by:

$$N_r = \frac{R_{2eff}}{2R_{2eff} + R_3} N_s. \tag{7.8}$$

The effective excitation rate R_{2eff} can similarly be generalized as

$$R_{2eff} = \sqrt{1 + \left(\frac{\eta \frac{4\pi}{3} C_3 \beta}{\Gamma}\right)^2} R_2, \tag{7.9}$$

so eqn. 7.8 can be simplified to:

$$N_r = \frac{R_2 V \eta}{2R_2 \sqrt{1 + \left(\frac{\eta \frac{4\pi}{3} C_3 \beta}{\Gamma}\right)^2} + R_3}. \tag{7.10}$$

We now have a generalized equation for the number of Rydberg atoms excited which is valid for for all regimes with the effective Rabi frequency less than the transition linewidth. The number of Rydberg atoms expected can be determined for a particular set of η, R_2, R_3, V, $C_3\beta$. This will give us a means to quantitatively examine the number of Rydberg atoms created as a function of several experimental parameters. Being able to vary several parameters provides an excellent check on our understanding which has been absent in many of the experiments to date. In Sections 8.2 and 8.3 the atomic density and excitation rate, respectively, are varied. As we will see, this allows the extraction of the expected interaction strength $C_3\beta$ given the stimulated emission rate.

It is also worthwhile to consider the scaling of the change in Rydberg atom number, $\frac{dN_r}{dt}$, at small times. Following the line of thought described above, we can write this

rate as

$$\frac{dN_r}{dt} = N_s R_{2eff}, \tag{7.11}$$

which in the most general case can be written

$$\frac{dN_r}{dt} = \frac{\eta V}{\sqrt{1+\left(\frac{\eta\frac{4\pi}{3}C_3\beta}{\Gamma}\right)^2}} \frac{\epsilon_{2eff}^2}{\sqrt{\Gamma^2+\epsilon_{2eff}^2}}, \tag{7.12}$$

where the linewidth of the determined by the larger of the transition linewidth or excitation rate. As already discussed, for the densities available in our experiment $\Gamma > \epsilon_{2eff}$. This results in the simplification of eqn. 7.12 to

$$\frac{dN_r}{dt} = \frac{\eta V \epsilon_2^2}{\Gamma}, \tag{7.13}$$

which would scale linearly in both the ground state density and the 480 nm power. If we were in the "strongly interacting" regime described earlier in this section, we would instead see a dependence that went as:

$$\frac{dN_r}{dt} = \frac{\eta V \epsilon_2^2}{\Gamma} \frac{1}{\sqrt{1+\frac{\eta^{2/3}(\frac{4\pi}{3})^{2/3}\epsilon_2^{4/3}(C_3\beta)^{2/3}}{\Gamma^2}}}. \tag{7.14}$$

Observing $\frac{dN_r}{dt}$ can verify the regime of atom-atom interactions, as we expect a linear scaling with both density and excitation intensity. An additional consistency check is provided by the excitation volume extracted from the linear fit.

The ability to perform a quantitative investigation of the interaction strengths represents an excellent advance in the experimental understanding of atom-atom interactions. This improvement beyond observing qualitative agreement with the scaling laws can serve as a further check on our understanding in a variety of systems.

7.3 Van der Waals Interactions

Now having an idea of the expected behavior of the atomic excitation, we wish to have a theoretical estimate of the atom-atom interactions with which to compare the results of

our data. The basic theory of two interacting dipoles has been well understood through classical theory for quite some time [Jackson, 1999]. These two dipoles interact and produce an energy shift of

$$U(R)_{dd} = \frac{\vec{p_1} \cdot \vec{p_2} - 3(\hat{n} \cdot \vec{p_1})(\hat{n} \cdot \vec{p_2})}{4\pi\epsilon_0 |R_1 - R_2|^3}, \tag{7.15}$$

where $\vec{p_i}$ is the dipole moment of atom i, $\hat{n}$ is the unit vector along the axis of atomic separation, and $|R_1 - R_2|$ is the separation of the atoms.

The first order dipole-dipole interaction requires states of opposite parity, which are absent in the case of excitation to a single Rydberg state. One way of mixing parity is by the application of an electric field [Gallagher, 1994]. Our current chamber is not equipped to apply electric fields at the atoms, and there are several other concerns which make implementing this scheme non-ideal. The introduction of electrodes near the atoms would make the presence of stray electric fields hard to eliminate and control. In addition, these dipole-dipole interactions still go to zero at an orientation angle of 54.7°, as seen from Eqn. 7.15.

An alternative to first order dipole-dipole interactions arises from the van der Waals interaction. These interactions can have comparable strength to the dipole-dipole interactions when there exists a pair of nearly degenerate two atom states. As seen in Fig. 7.2, the ns states of high lying Rydberg levels are close to symmetrically located between the np and $(n+1)p$ states. Similarly, the nd states lie between $(n-1)f$ and $(n+1)p$. The resonant energy transfer processes:

$$ns + ns \rightarrow np + (n-1)p, \tag{7.16}$$

$$nd + nd \rightarrow (n+1)p + (n-1)f \tag{7.17}$$

are characterized by a small energy defect, δ. This defect is defined by the energy levels

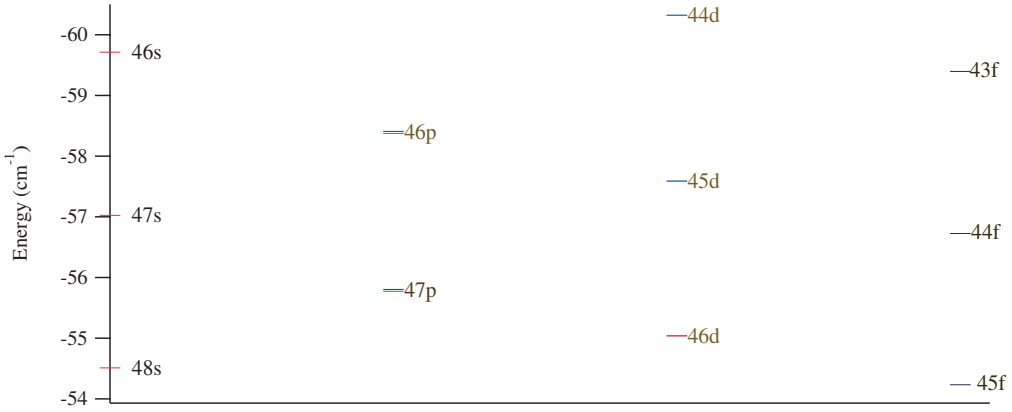

Fig. 7.2: Energy level spacing near n=47 Rydberg states. Pairs of atoms can be nearly degenerate with atoms in nearby states, resulting in large Van der Waals interactions.

of the initial and final states,

$$\delta = E_{f1} + E_{f2} - 2E_i \tag{7.18}$$

where E_{f1}, E_{f2}, and E_i are the energies of the two final states and the initial state.

If other possible channels are ignored, the Rydberg potential energy curves are then given by

$$U(R)_{vdW} = \frac{\delta}{2} + \sqrt{\frac{D_\phi C_3 C_3'}{R^6} + \frac{\delta^2}{4}}, \tag{7.19}$$

where $C_3 = e^4 < ns||r||np >^2$ $C_3' = e^4 < ns||r||(n-1)p >^2$ [Saffman and Walker, 2005].

The term D_ϕ in eqn. 7.19 is the factor correcting for the angular momentum properties of the interaction, about which a detailed analysis can be found elsewhere [Walker and Saffman, 2008]. While this factor is fairly straightforward for excitation to the $|s\rangle$ states, it becomes more complicated for $|d\rangle$ states. Here there exist particular sublevels with very small interactions. For a complete blockade, these would be the limiting factors where excitation would occur. In calculating an average interaction strength for quantifying the suppression, I have taken the average of the blockade radii for each excitation channel.

State	C_6(MHz μm^6)	R_b (μm)	N_b
30s	22.6	1.35	.2
47s	$3.81 \cdot 10^3$	3.17	2.6
60s	$1.2 \cdot 10^5$	5.63	15
28d	119	1.33	.2
43d	$5.4 \cdot 10^5$	5.44	13.5
58d	$3.2 \cdot 10^5$	5.86	16.9

Tab. 7.1: The van der Waals interaction strengths, blockade radius, and blockaded number for various Rydberg levels accessible to our experiment. The transition linewidth is assumed to be 5 MHz.

At large interatomic spacing, when $\frac{C_3 C_3'}{R^6} << \delta^2$, eqn. 7.19 can be simplified to

$$U(R)_{vdW} = \frac{C_6}{R^6}, \tag{7.20}$$

where $C_6 = \frac{D_\phi C_3 C_3'}{\delta}$.

The van der Waals shift is isotropic, which is advantageous for any attempt at blockade. The strength of this interaction depends upon the energy defect δ and the radial matrix elements $\langle r \rangle$. The strength of the Rydberg-Rydberg interactions can be seen to vary strongly with principal quantum number. The radial matrix element $\langle r \rangle$ scales as n^2, so C_6 scales as n^8. In addition, the energy defect δ scales as n^{-3}, so the van der Waals interactions $U(R)_{vdW}$ scale as n^{11}. As a result, increasing the principal quantum number can drastically affect the range of the Rydberg blockade. The details of how the energy defect, δ and the radial matrix elements $\langle r \rangle$ are calculated are discussed in Appendix A. The results of evaluating the strength of these interactions for the Rydberg levels accessible in our lab can be seen in Table 7.1.

To qualify how effective our blockade will be, we also define an effective blockade radius, R_b. Any atoms inside a blockade sphere would have atom-atom interactions

larger than the effective linewidth of excitation, Γ_L, and their excitation would be suppressed. The effective blockade radius can be found for Van der Waals interactions while taking the angular momentum properties into account by:

$$\Gamma_L = U(R)_{vdW} = \frac{C_6}{R_b^6}. \tag{7.21}$$

The calculated values for the effective blockade radius using our experimental linewidth of 5 MHz are shown in Table 7.1, along with N_b, the expected number of atoms within each blockaded region given our maximum ground state atomic densities.

7.4 Microwave Coupled Dipole-Dipole Interactions

While the interaction energy from van der Waals can be quite large for attainable Rydberg levels, it is still beneficial to consider alternative means of increasing the interaction energy. One mechanism which would accomplish this goal is resonant coupling from the initial Rydberg state to nearby Rydberg states of opposite parity using microwaves. This was described in Section 6.2, and results in a wavefunction:

$$|\Psi\rangle = \frac{|s\rangle + |p\rangle\, e^{-i\omega t}}{\sqrt{2}}. \tag{7.22}$$

In this case first order dipole-dipole interactions would be allowed, as the wavefunction contains a component of both the $|s\rangle$ and $|p\rangle$ states. For the simplified case of a single angular momentum state, averaging this interaction over time gives:

$$U(R)_{dd} = \frac{C_3}{R^3}\frac{1}{2}(3\cos^2\Theta - 1), \tag{7.23}$$

where $C_3 = e^2 < nl||r||n'l' >^2$ and Θ is the angle between the interatomic separation and the microwave field polarization.

An additional level of complexity occurs when there are degenerate angular momentum states available which modify the effective dipole-dipole interaction. In general,

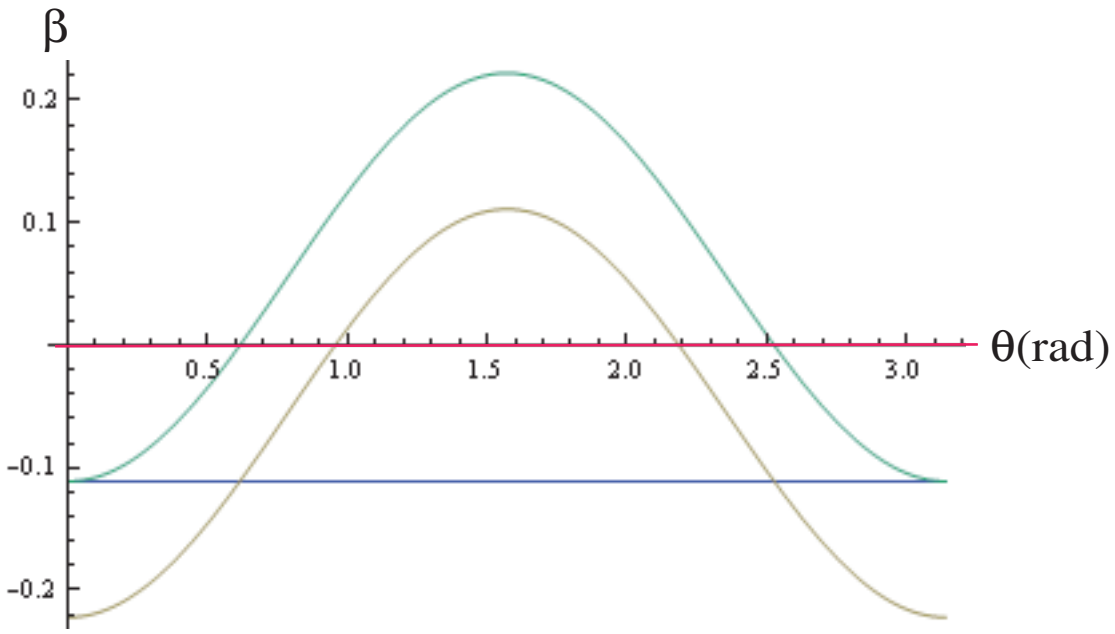

Fig. 7.3: The interaction energy as a function of the angle between the two dipoles for the possible angular momentum states for microwave coupling on $|s_{1/2}\rangle \rightarrow |p_{1/2}\rangle$. A state exists with zero interaction energy, which would prevent blockade to the single atom level, though multiple excitations would still be suppressed. The $|s_{1/2}\rangle \rightarrow |p_{3/2}\rangle$ coupling does not have this zero, and could be used in pursuit of a blockade.

these additional channels can be quantified by a correction factor β, which denotes the average interaction strength for the allowed channels over π. An example of the calculated correction factors for the eigenstates of the $|s_{1/2}\rangle \rightarrow |p_{1/2}\rangle$ interaction as a function of Θ are shown in fig. 7.3. The details of this calculation are left to Appendix B, but give an average value of $\beta = 0.076$.

Despite the reduced and anisotropic interactions of the various angular momentum states, microwave coupled interactions can still be quite large, as seen in Table 7.2 for the Rydberg levels accessible in our experiment. Since the interaction will now be anisotropic, the blockaded volume will be a more complex shape than a sphere, but a spatial average can be made to obtain an effective blockade radius. Included in the

State	C_3(MHz μm^3)	R_b (μm)	N_b
30s	684	2.3	1.0
47s	$4.75x10^3$	4.4	7.2
60s	$1.33x10^4$	6.2	20
28d	920	$\sim$2.5	$\sim$1.3
43d	$5.35x10^3$	$\sim$4.6	$\sim$8.1
58d	$1.81x10^4$	$\sim$6.9	$\sim$27.2

Tab. 7.2: The dipole-dipole interaction strengths, blockade radius, and blockaded number for various Rydberg levels accessible to our experiment using microwave coupling of adjacent Rydberg states. The transition linewidth is assumed to be 5 MHz.

table are this blockade radius and the expected number within a blockade sphere. The effective blockade radius is now defined where the average dipole-dipole interaction is equal to the effective linewidth

$$\Gamma_L = U(R)_{dd} = \frac{C_3\beta}{R_b^3}. \tag{7.24}$$

The $|d\rangle$ states should give suppression of excitation for the MOT densities available in our lab, but these states provide additional complication. It has been shown that $|d\rangle$ states ionize on a timescale much faster than the $|s\rangle$ states [Li *et al.*, 2005], and we have seen that this ionization causes difficulties in observing excitation suppression in Section 6.4. As a result of this complication, the $|d\rangle$ states are not suitable for the investigation of excitation suppression and are not used in the suppression experiments of the next chapter. In the absence of an experimental motivation, a full theoretical treatment of the microwave dipole-dipole interaction for $|d\rangle$ states has not yet been given. The numerical values in Table 7.2 are approximations assuming the same β factor as for $|s_{1/2}\rangle \rightarrow |p_{1/2}\rangle$.

Since with $|s\rangle$ states ionization should not be a problem, they represent an excellent means to investigate excitation suppression. For the $|47s\rangle$ state, we can change from van der Waals interactions where the suppression is expected to be minimal to resonant microwave coupling where we expect to see noticeable suppression. This will be explored in Chapter 8, and presents an excellent means to investigate suppression in light of the scaling laws presented in Section 7.2.

8. RYDBERG SUPPRESSION

8.1 Introduction

In this Chapter I will describe the experiments which make use of the experimental techniques described in Chapter 6 to investigate the effects of atom-atom interactions on Rydberg excitation. Here I will explore the dependence of Rydberg excitation under a variety of conditions. The theoretical predictions of Chapter 7 suggest that the observation of excitation suppression should be possible with the experimental parameters available in our lab.

The simplest way to investigate the presence of atom-atom interactions is to measure the number of Rydberg atoms created as a function of the density of atoms in the MOT. Section 8.2 will describe experiments which investigate this scaling at $|47s\rangle$, with and without applied microwave coupling. It can be seen that without microwave coupling the number of Rydberg atoms scales linearly with density, an indication that the interactions are not large enough to significantly suppress excitation. With microwave coupling to the $|47p\rangle$ state however, we see a distinct fall off from this linear scaling at high atom densities. This can be fit using the expected scaling discussed in Section 7.2 to obtain a measurement of the interaction strength, $C_3\beta = 270\pm120$ MHz μm^3 in reasonable agreement with theory. Additionally, we have observed the dependence of $\frac{dNr}{dt}$, which is in reasonable agreement with the linear dependence expected.

We have also investigated the dependence of the number of Rydberg atoms cre-

ated versus the power of the 480 nm laser, and hence the excitation rate, in Section 8.3. Similarly, at high excitation rate we would expect the number of Rydberg atoms to be suppressed. This effect is clearly absent from the Van der Waals interaction case. When the microwaves are applied, we again see evidence for suppression. This data is again fit to the expected scaling law, giving $C_3\beta = 300\pm120$ MHz μm^3. This value is in agreement with that obtained from the density dependence, suggesting good understanding of the interactions.

The Chapter concludes in Section 8.4 with a discussion of the importance of these results for the future. The correlation between successful demonstration of excitation of suppression and the ability to obtain single atom blockade is in fact not automatic, and this is a reality that is often misunderstood in the field. Microwave coupling provides an excellent example of the distinction between suppression and blockade, giving important insight for future applications.

8.2 Density Dependence

The analysis of Section 7.4 suggests that for the atomic densities present in our MOT, we should be able to create locally blockaded volumes with as many 20 atoms per blockade region using the $|60s\rangle$ state with microwave coupling. In order to increase the available Rabi frequencies and see a more dramatic effect from microwave coupling, we have chosen to perform proof of principle experiments at $|47s\rangle$. At this Rydberg state, we can still attain two-photon excitation frequencies of $\sim$ 500 kHz, and expect to see noticeable suppression of Rydberg excitation with the application of microwave coupling to at $|47p_{1/2}\rangle$.

Using the technique of pulsed excitation described in Section 6.4, we will now look directly for experimental evidence of suppression. As a first investigation, we will

vary the density of ground state atoms. We reduce this density from its maximum value by placing an iris in the MOT trapping beam before it is split. This technique enables variation of the number of atoms without significantly altering the volume of the MOT. An exact determination of the change in MOT volume is not available at the time of this dissertation. However, observation of the approximate MOT size on a CCD camera reveals no noticeable change. Previously the volume has been measured while the atom number was varied with this technique, and was seen to change less than 15% for reducing the number by an order of magnitude. For our current purposes the volume is assumed to stay constant over the reduction in atom number presented here. This will provide some uncertainty to the data, in addition to the standard factor of two uncertainty in the total number of atoms in the MOT.

At this point it is necessary to clarify a few complexities involved in the acquisition and analysis of our data. For a yet undetermined reason, the total number of Rydberg atoms created for a particular set of parameters (ground state density, excitation rate, stimulated emission rate, location in ac Stark shift) can vary by up to a factor of two. The timescale for this change appears irregular, but can happen on as little as a few minute timescale. Obviously, this is a problem for accurately comparing the number of Rydberg atoms created. In order to correct for this effect, we have developed a method of taking "control" points around surrounding each data point. The control points are taken with full density and laser powers, and the number of Rydberg atoms for a data point is scaled according to the control points on either side. While this still allows for errors resulting from an uneven rate of change, it greatly reduces the effect of this uncertainty. Currently, we are working on eliminating the source of drift. It is believed this comes from a few percent change in the intensity of the 780 nm laser. While the change in excitation rate is not significant, it also changes the ac Stark shift, and hence the depth of the shift compared to our excitation point. An intensity stabilizer

is currently being constructed to fix this issue, and hopefully eliminate the fluctuations in the future. For the present, our method of correcting for this problem still enables investigation of the Rydberg atom production.

If no microwaves are applied, theory suggests that only ∼2 atoms are present in the blockaded volume at maximum density. Hence, only a very small amount of suppression is expected, and this presents an excellent means of verifying our ability to control and understand the environment. Figure 8.1 shows a series of scans taken with various ground state atom densities, while the excitation and stimulated emission rates were maintained at their maximum value: ϵ_2 =200 kHz and ϵ_3 =225 kHz. This data was taken at what we call the "deep" portion of the ac Stark shift, exciting from ∼-65 MHz from the natural frequency, where the full depth is ∼-71 MHz. The number of Rydberg atoms is also plotted versus the ground state density in Fig. 8.1. A linear dependence is observed, supporting the estimate that atom-atom interactions do not effect the excitation in this regime.

The situation changes as microwaves are applied, as now ∼7 atoms are predicted to be within a blockaded volume at maximum density. Figure 8.2 again shows a series of scans taken with various ground state atom densities, while the excitation and stimulated emission rates were maintained at their maximum value, this time with microwaves on resonance to the $|47p_{1/2}\rangle$ state. At high ground state densities, the number of Rydberg atoms produced ceases to grow linearly, as can be seen in Fig. 8.2. This deviation from a linear dependence suggests that the increased interactions between atoms have started to suppress further Rydberg excitation as the density is increased.

We can further fit the data using Eqn. 7.10, showing good agreement with the expected scaling. From the fit to the density dependence, we obtain an excitation volume of $1.7 \pm .5 \cdot 10^5$ μm^3 and an effective interaction strength $C_3\beta$ of 270±120 MHz μm^3. The excitation volume is consistent with the estimate given from the laser

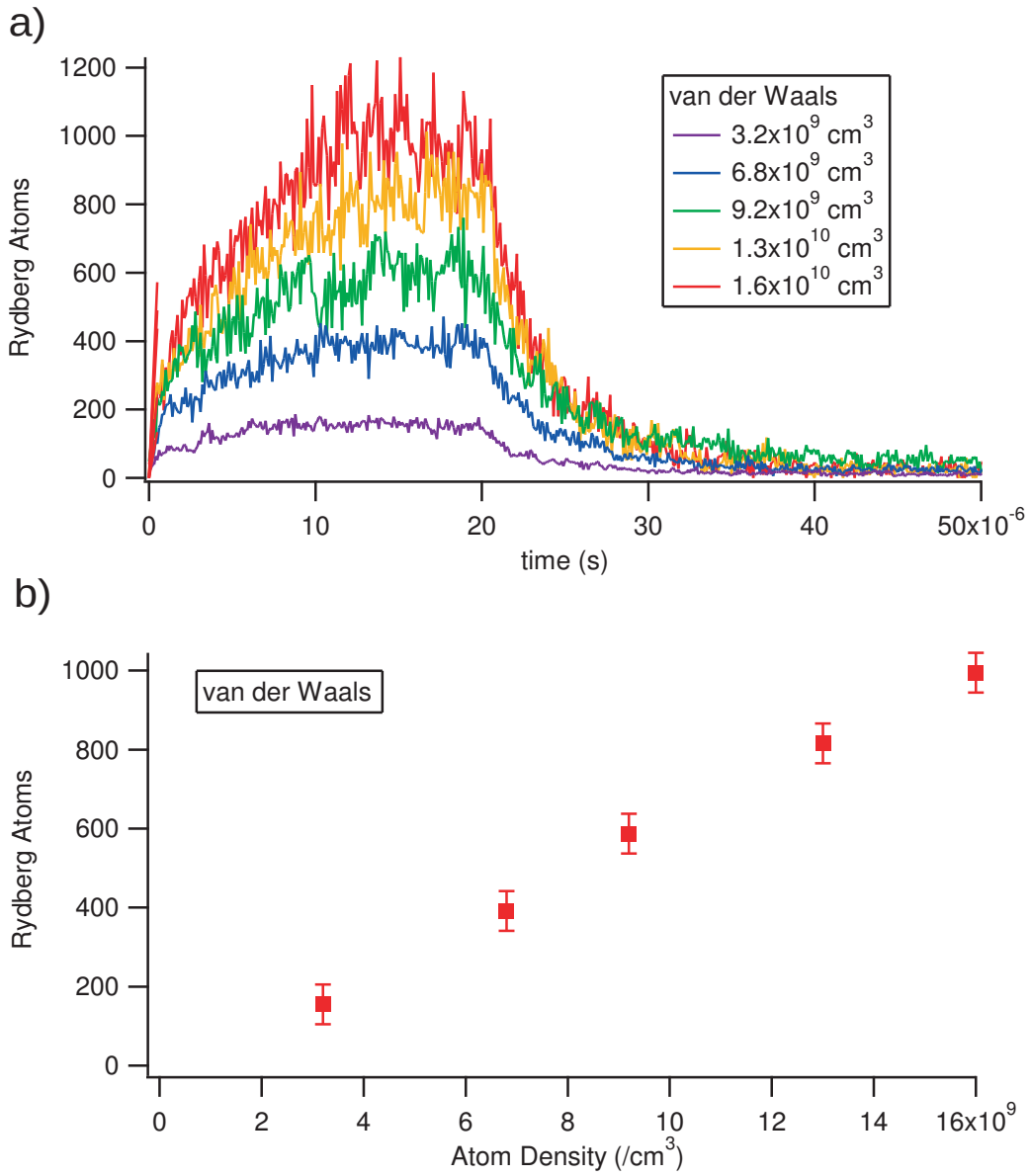

Fig. 8.1: An examination of the Rydberg production with only van der Waals interactions. a)The Rydberg atom population resulting from a pulsed excitation scheme at different ground state atom densities. b) A plot of Rydberg atom number versus ground state density shows a linear dependence, and indicates that atom-atom interactions do not limit excitation.

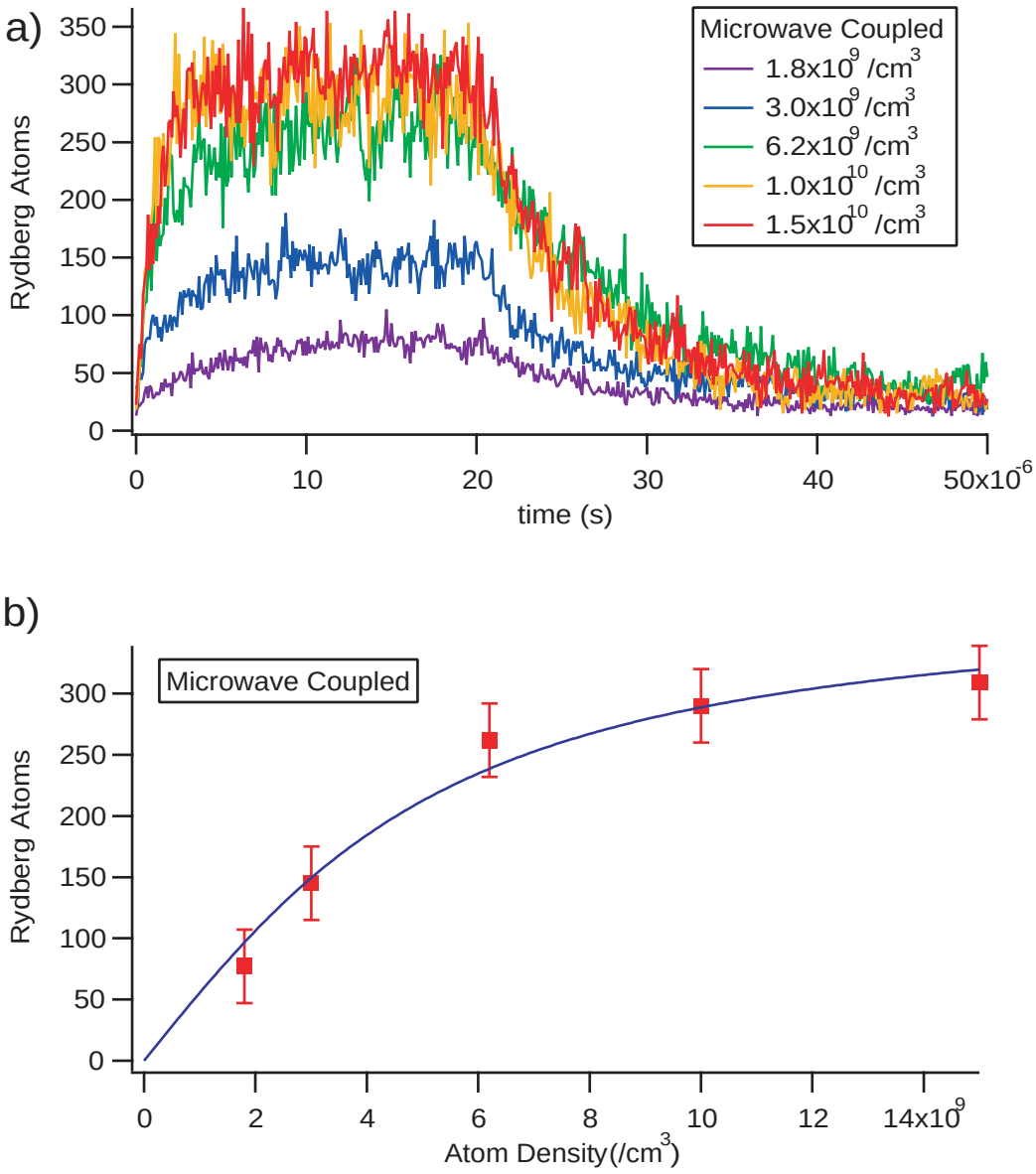

Fig. 8.2: An examination of the Rydberg production with microwaves coupling the $|47s\rangle$ and $|47p_{1/2}\rangle$ states. a)The Rydberg atom population resulting from a pulsed excitation scheme at different ground state atom densities. b) A plot of Rydberg atom number versus ground state density shows a clear deviation from linear dependence, and indicates that atom-atom interactions begin to suppress Rydberg atom excitation. The data is fit using Equation 7.10, giving $C_3\beta = 270\pm120$ MHz μm^3.

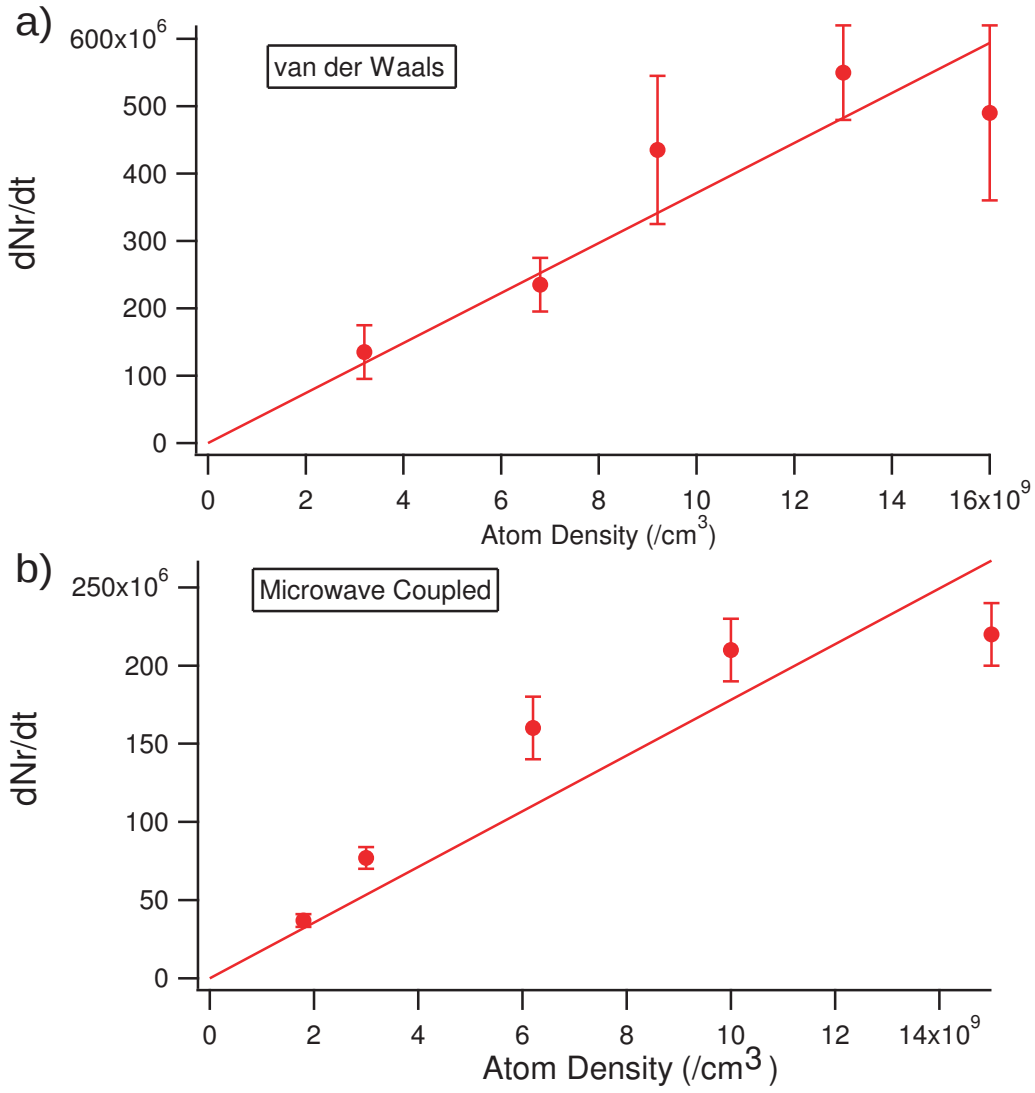

Fig. 8.3: An examination of the initial rate of Rydberg atom production with and without microwaves coupling the $|47s\rangle$ and $|47p_{1/2}\rangle$ states. a) A plot of Rydberg atom production rate versus ground state density with van der Waals interactions b) A plot of Rydberg atom production rate versus ground state density with microwave coupling. Here the expected dependence is linear in both cases.

beam waists of $1.9 \cdot 10^5$ μm^3, as discussed in section 6.3. The interaction strength indicates a β value of 0.056±0.026. This value is slightly lower than the theoretical value of .076, but reasonable considering the uncertainty of the measurement and the incomplete theoretical understanding of the system, especially the question of blockade radius when there are multiple potentials.

We can also gain information about the initial Rydberg atom production $\frac{dN_r}{dt}$. As discussed in Section 7.2, this is expected to have a linear dependence on the density in the regime where the transition linewidth is significantly larger than the effective excitation rate. Figure 8.3 shows this initial change in Rydberg number versus the ground state density for both the Van der Waals and microwave coupled case. The fit allows the extraction of the excitation volume, which gives $2.4\pm.4\cdot10^5$ μm^3 and $1.5\pm.3\cdot 10^5$ μm^3, respectively with and without microwave coupling. These values are consistent with the value determined from the fit to the number of Rydberg atoms. While this data is consistent with a linear dependence, it is possible that we are beginning to see the dependence of the strong interaction regime at high densities. If higher densities are achieved in the future, it will be interesting to further examine this transition.

8.3 Intensity Dependence

As an secondary means of examining the Rydberg atom excitation, it is possible to vary the Rydberg atom density by changing the excitation rate. This can be done through simple attenuation of the 480 nm laser power, and provides an additional means of investigating suppression. However, the effects from altering the excitation rate are slightly more complicated than simply adjusting the atomic density.

The equilibrium number of Rydberg atoms depends upon the ratio of the excitation rate compared to the other important rates in the system. If the excitation rate is

small compared to rates out of the Rydberg state (spontaneous decay, blackbody, or stimulated emission), the number of Rydberg atoms should grow linearly with the excitation rate. In contrast, in a sample where the excitation rate is much greater than the other rates in the system, the number of Rydberg atoms should simply go to half of the atoms in the excitation volume, and be independent of the excitation rate (aside from a slight growth due to the excitation volume expanding with saturation). The experiments described here were done in an intermediate regime where the excitation rate was approximately equal to the stimulated emission rate. For a region without blockade, this can be expressed as:

$$N_r = \frac{R_{2eff} N_{tot}}{2R_{2eff} + R_3}. \tag{8.1}$$

At this juncture it is worth discussing the balance of excitation and stimulated emission rates. In order to create the highest densities of Rydberg atoms, the highest possible excitation rate is desired, but the selection of the stimulated emission rate is more complicated. A very low stimulated emission rate lowers our photon detection rate, and can make signal to noise levels unacceptably low. Our current laser powers would allow for stimulated emission rates several orders of magnitude higher than the excitation rate if tightly focused beams were used. However, while this would result in the highest possible photon count rates, it would also "short-circuit" any blockade effect, as no equilibrium Rydberg population could be achieved. A planned experiment investigating this effect is discussed in Section 9.2. For now, we have chosen the intermediate regime, where good signal to noise is accomplished while still allowing blockade.

Having relatively balanced excitation and stimulated emission rates results in a slight, but non-linear dependence, on the excitation rate. A set of pulse sequences taken to investigate this dependence can be seen in Fig. 8.4, along with the the Rydberg

atom number plotted versus the 480 nm laser power. Here a simple fit using Eqn. 8.1 is included to demonstrate the expected behavior in the absence of interactions.

The effect of adding strong atom-atom interactions to this already non-linear dependence is slightly less obvious than a deviation from the clear linear scaling of Section 8.2. Nonetheless, it can still be qualitatively observed as a faster saturation in the number of Rydberg atoms. Figure 8.5 shows the excitation pulse data and dependence of the Rydberg excitation versus the power of the 480 nm laser for the case of microwave coupling between the $|47s\rangle$ and $|47p\rangle$ states. Included is the data and fit taken without microwave coupling for easy comparison.

The data is again fit using Equation 7.10, showing good qualitative agreement. From the fit we obtain an excitation volume of $1.9 \pm .6 \cdot 10^5$ μm^3 and an effective interaction strength $C_3\beta$ of 300$\pm$120 MHz μm^3. Both of these values are consistent with the results of the density dependence, giving further evidence of our understanding of the behavior. The dependence of $\frac{dN_r}{dt}$ on the 480 nm power is shown in Fig. 8.6, again showing a linear dependence. The data with and without microwave coupling gives gives a volume of $1.5 \pm .3 \cdot 10^5$ μm^3 and $2.0 \pm .3 \cdot 10^5$ μm^3, respectively. Again this is in reasonable agreement. The data presented here gives further support that the atom-atom interactions are increased by resonant microwave coupling.

8.4 Discussion

Despite fairly large systematic uncertainties in our system, we have been able to observe a distinct onset of suppression when microwaves are applied on resonance with the $|47s\rangle \rightarrow |47p\rangle$ transition. This is the first experiment to show evidence for suppression of excitation resulting from resonant microwave coupling. In addition, we are able to make quantitative evaluations of the strength of these interactions by examining the

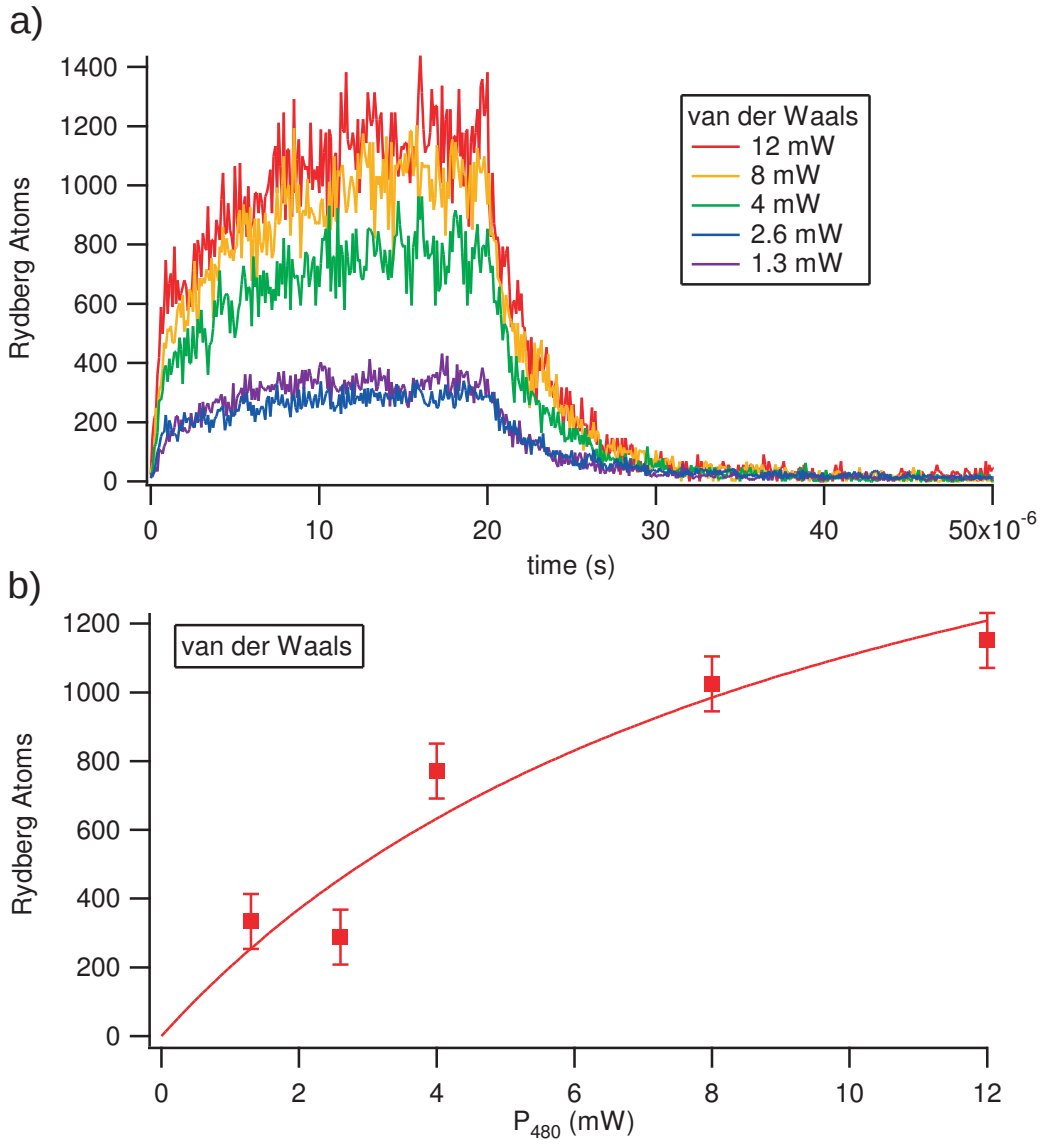

Fig. 8.4: An examination of the Rydberg atom population with only van der Waals interactions. a)The Rydberg atom population resulting from a pulsed excitation scheme at different 480 nm laser powers. b) A plot of Rydberg atom number versus 480 nm laser power. The fit uses the expected scaling without interactions, and shows agreement with the data.

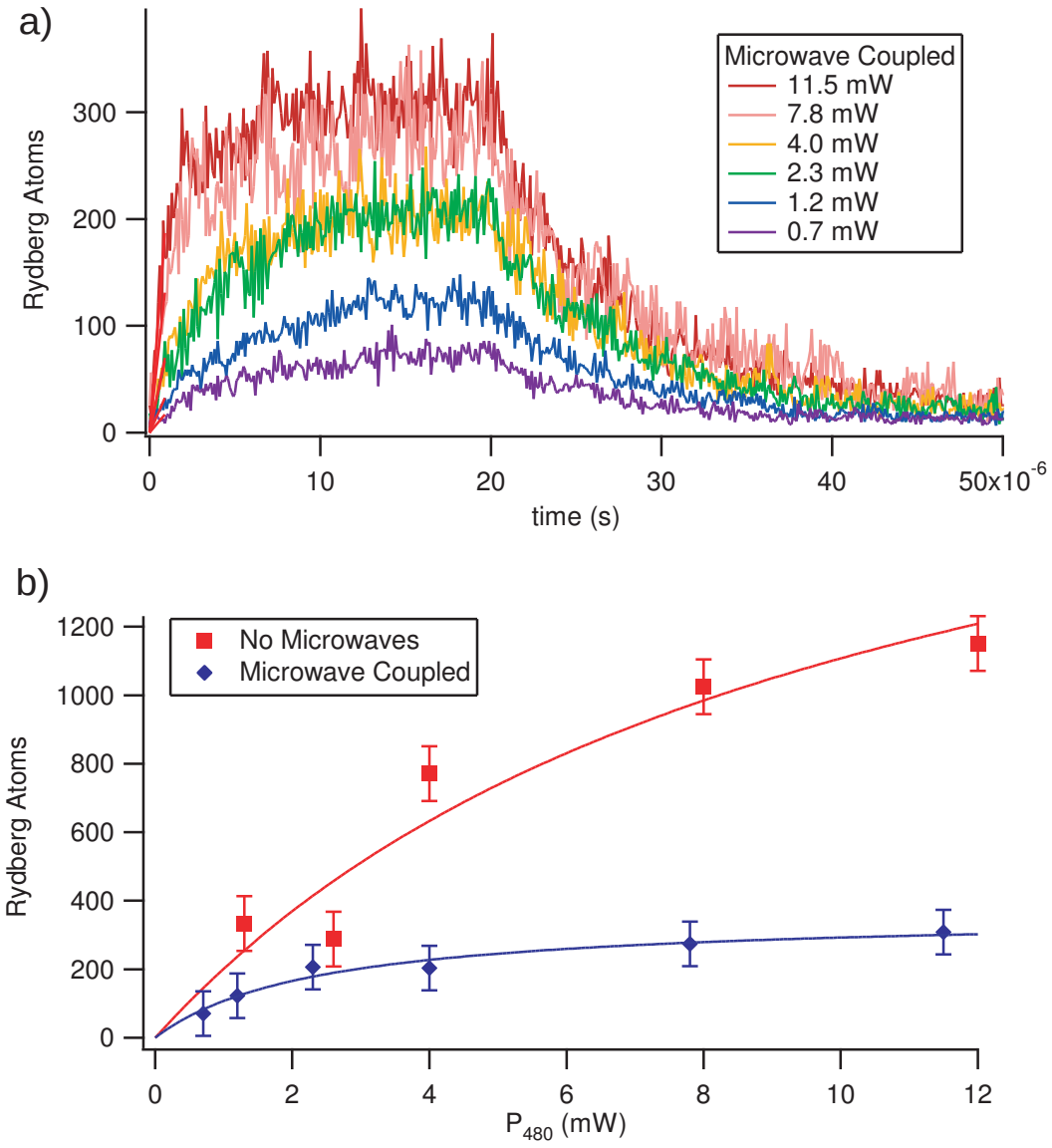

Fig. 8.5: An examination of the Rydberg atom population with microwaves coupling the $|47s\rangle$ and $|47p_{1/2}\rangle$ states. a)The Rydberg atom population resulting from a pulsed excitation scheme at different 480 nm laser powers. b) A plot of Rydberg atom number versus 480 nm laser power, both with and without microwaves to allow observation of the difference which increased interactions provide. The microwave coupled data is fit using Equation 7.10, giving $C_3\beta = 300\pm120$ MHz μm^3.

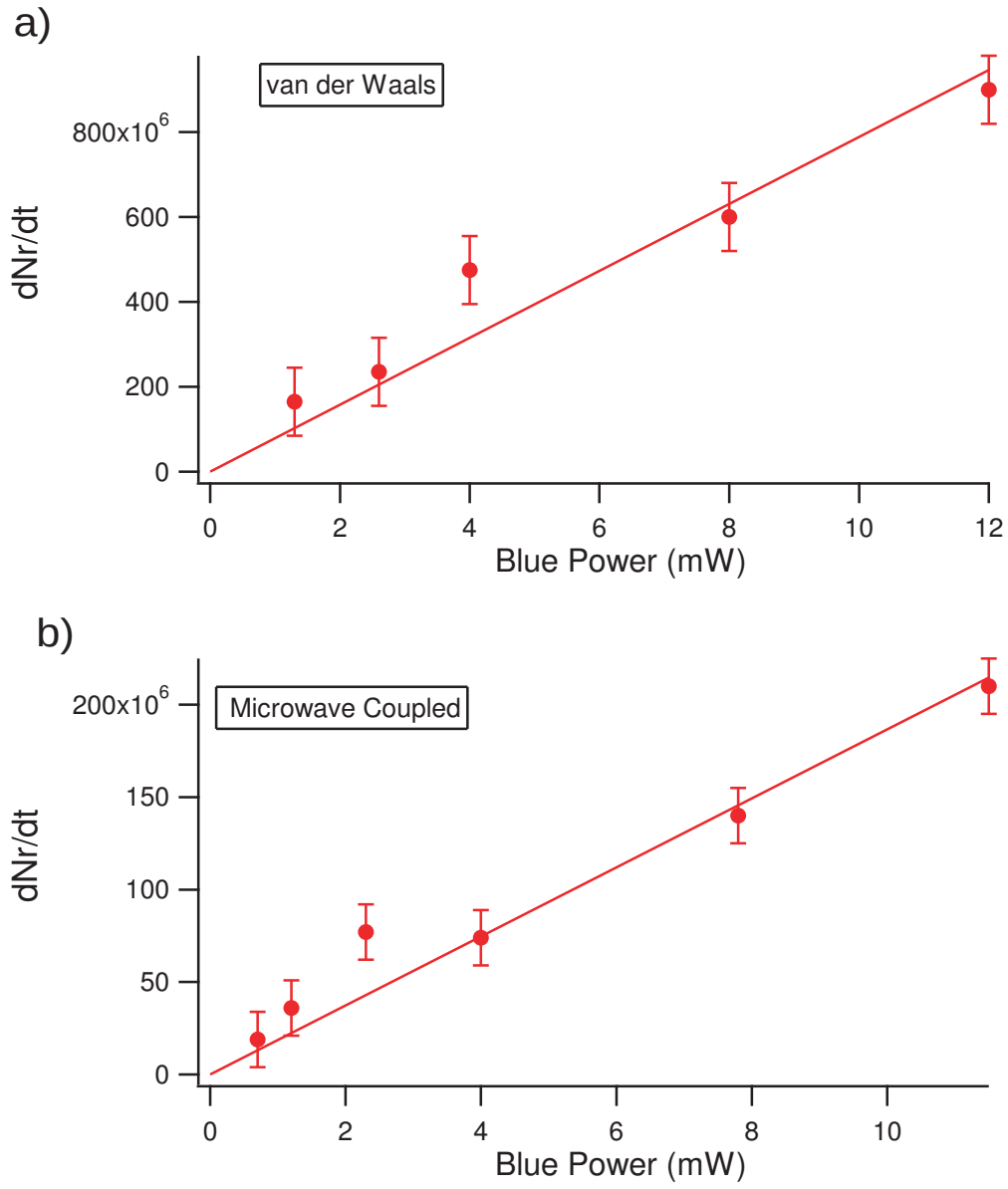

Fig. 8.6: An examination of the initial rate of Rydberg atom production with and without microwaves coupling the $|47s\rangle$ and $|47p_{1/2}\rangle$ states. a) A plot of Rydberg atom production rate versus 480 nm power with van der Waals interactions b) A plot of Rydberg atom production rate versus 480 nm power with microwave coupling. Here the expected dependence is linear in both cases.

scaling of the excitation behavior.

The application of microwave coupling to increase interaction strengths in Rydberg gases for future applications such as quantum computing or single photon sources is worth careful consideration. For these applications, it is necessary to obtain a complete blockade of the sample, with only one atom excited at a time. It is important to emphasize that the observation of suppression in large volumes does not guarantee the effectiveness of blockade on a single atom level.

An excellent example of this distinction can be seen in the case of microwave coupled $|s_{1/2}\rangle \rightarrow |p_{1/2}\rangle$ states. As can be seen in fig. 7.3, there exists a particular angular momentum state of these two atoms which results in zero dipole-dipole interaction. This state would eliminate the possibility of single atom blockade, and make this coupling critically flawed for application in a quantum computer or single photon source. Despite this, in a many body sample there could still exist an average interaction strength resulting in the suppression of excitation, as we saw in Sections 8.2 and 8.3.

Fortunately, the $|s_{1/2}\rangle \rightarrow |p_{3/2}\rangle$ interactions do not contain such "zero states", and all channels have a finite interaction strength. This coupling will then provide a better choice for the pursuit of any application which requires blockade at the single atom level. At the time of the experiments in this chapter, the effect of the angular momentum states had not been considered, and so the microwaves were chosen for experimental convenience to couple the $|s_{1/2}\rangle \rightarrow |p_{1/2}\rangle$ states. In the future, we will switch to the $|p_{3/2}\rangle$ to examine the difference the "zero state" makes. A complete understanding of the effect of this angular momentum coupling is yet to be achieved, and remains an interesting theoretical field.

Going forward, microwave coupling can significantly enhance the blockade volume at small principal quantum numbers. At higher principal quantum numbers, the gain in blockaded volume in fact becomes quite small, due to the fact that the van der

Waals interactions scale as n^{11} while the microwave interactions only scale as n^4. This noticeably reduces the advantage of microwave coupling even at n=60, as seen in Tables 7.1 and 7.2. At high principal quantum numbers it remains unclear if the small gain in interaction strength is worth the loss of excitation rate involved. Further experiments are underway to continue to investigate this possibility, as will be discussed in Section 9.2.

9. CONCLUSION

9.1 Summary of Dissertation

In this section I will conclude the dissertation with a summary of the major results. The primary goal of this dissertation was the implementation of a stimulated emission probe for the study of ultracold Rydberg atoms, which has allowed the exploration of three important areas of Rydberg atom physics.

First, we were able to observe the Rydberg atom dynamics with a tool unavailable to any other group, the stimulated emission probe, allowing the determination of the transfer rate out of the Rydberg state. This transfer rate was an order of magnitude larger than could be expected from spontaneous decay or blackbody transfer, revealing the presence of another process. We were able to observe from the loss rate and dependence on principal quantum number that collisions and ionization were not responsible for this transfer, eventually leading us to the conclusion of superradiance. A simple model of the process agrees well with the experimental data, and this work was the first to emphasize the importance of superradiance for the evolution of a Rydberg atom cloud.

The examination and optimization of a phase-matched four-wave mixing process through the Rydberg state represents the second main contribution of this dissertation. This demonstrates a coherent excitation through the Rydberg state, one of only a few experiments to accomplish this due to the strong Rydberg-Rydberg interactions.

In addition, we have demonstrated that by detuning the process from the Rydberg resonance, up to 50% of the light was emitted into a diffraction limited direction. This increase in collection efficiency is an essential component of a useful single photon source.

Finally, we have begun investigations of the interactions between Rydberg atoms, and developed resonant microwave coupling as a viable strategy to increase the atom-atom interactions. Our technique demonstrated the suppression of excitation resulting from resonant microwave coupling, and gave an experimental measure of the interaction strength in agreement with theory. This opens the way to a successful demonstration of photon anti-bunching and the implementation of a single photon source.

9.2 Ongoing Experiments

The experiments described in this thesis are ongoing, and several experiments are planned for the future. In the short term, several improvements have been planned to verify the suppression of excitation resulting from resonant microwave coupling and to improve the ease of our data taking and analysis. In addition, a yet unexplored variable in our exploration of suppression is the Rabi frequency of the stimulated emission probe. It is expected that with stimulated emission rates significantly higher than the excitation rate, there would be no suppression. Since no Rydberg population could accumulate with a high stimulated emission rate, the blockade would effectively have a "short circuit".

Following the current experiments, a major goal is to increase the ground state atom densities. This would enable the observation of suppression for van der Waals interactions, and allow further investigation into their strength and characteristics. In addition, higher densities would enable the verification of the scaling laws in the strong

interaction regimes. Higher density is also a necessity to accomplish phase-matched four-wave mixing in a small volume which could be blockaded.

Previously, we have used a 20 W Nd:YAG laser to produce a Far Off-Resonance Trap (FORT) with densities as high as $2x10^{15}\ cm^3$ [Sebby-Strabley *et al.*, 2005]. The next step in our lab will be to again establish a FORT, enabling these experiments at densities orders of magnitude higher than the experiments described in this dissertation. While it is possible to use the Holographic Atom Trap described in detail elsewhere [Sebby-Strabley, 2004], this has the drawback of creating an array of microtraps, which would complicate our ability to manipulate and understand the excitation. Instead, a simple FORT should enable densities of $\sim 10^{13}\ cm^3$.

This increased density would provide the ability to pursue evidence for the complete blockade of a small volume by the observation of photon anti-bunching. If only one atom was excited at a time, only one photon could be emitted at a time. This would result in a finite delay between photon emissions, which could be observed in a measurement of the second-order correlation function, $g^{(2)}$ of the emitted light. When combined with phase-matched emission to give high collection efficiency, we have the means to pursue a realistic implementation of a deterministic single photon source.

APPENDIX

A. EXPLANATION OF CALCULATION OF RYDBERG ENERGY LEVELS AND WAVEFUNCTIONS

We have two Igor programs which are used to calculate the energy levels and matrix elements for Rydberg atoms. This appendix will be a brief explanation of the background for these calculations, followed by an explanation of how the program is run. This is meant more as a guide to future use of the programs than a thorough explanation of the physics involved.

A.1 Energy Levels

Our calculation of the Rydberg energy levels is based on energy defect theory. In considering the Rydberg states of alkali atoms, they will be essentially similar to the Hydrogen atom. However, there will be slight differences due to the fact that the nucleus has a finite size that the Rydberg electron can penetrate or polarize. Both of these effects lead to an increased binding energy. The energy can be given by

$$E = \frac{-Ry}{(n - \delta_{nlj})}. \tag{A.1}$$

where Ry is the Rydberg constant of Rubidium, n the principal quantum number, and δ_{nlj} is the quantum defect. The quantum defects are best determined through experimental measurement of the Rydberg level energies. This has been done in two main ways: standard optical spectroscopy from low lying states and rf spectroscopy between nearby Rydberg levels. The most recent and accurate measurements can be

found here [Li *et al.*, 2003] [Han *et al.*, 2006]. In general, the defect is given by:

$$\delta_{nlj} = \delta_0 + \frac{\delta_2}{(n-\delta_0)^2} + \frac{\delta_4}{(n-\delta_0)^4} + \frac{\delta_6}{(n-\delta_0)^6} + \frac{\delta_8}{(n-\delta_0)^8} + ... \tag{A.2}$$

The program which uses this to calculate the energy levels can be found on the computer "Zoom" at $E:\backslash datavault\backslash wavelengths - new$. The command line "lamcalc(F,n,l,j)" will give the energy of the n, l, j Rydberg level above the $5P_{3/2}$ state, following several steps. First, the F level of the $5P_{3/2}$ state is used to determine the original binding energy.

This value is then added to the output of "ecalc(qn,ei,a,b,c,d,e)"

$$= ei - eis - \frac{-ryrb}{(qn - a + \frac{b}{(n-a)^2} + \frac{c}{(n-a)^4} + \frac{d}{(n-a)^6} + \frac{e}{(n-a)^8})}. \tag{A.3}$$

This equation calculates the energy of the Rydberg state using eqn. A.1 with the quantum defect from eqn. A.2, where $\delta_0, \delta_2, \delta_4, \delta_6, \delta_8$ have been labeled a,b,c,d,e. The term ei-eis in the program corrects for the different ionization potential based upon the l,j state. This program is quite accurate, and can be used to locate the transition to Rydberg levels within ∼100 MHz.

A.2 Matrix Elements

The evaluation of Rabi frequencies as discussed in Appendix B, will depend on the evaluation of the matrix element $\langle L_e| \, |r| \, |L_g\rangle^2$. This can be found from the numerical integration,

$$\langle r \rangle = \int r dr P_{n_e l_e}(r) P_{n_g l_g}(r), \tag{A.4}$$

provided that the Rydberg wavefunctions $P_{n_g l_g}$ are known. There are several techniques which can be used to calculate these wavefunctions, but the program used in our lab is based upon the model potential scheme developed by [Marinescu *et al.*, 1994]. The

details of this calculation are quite involved, and so this Appendix will merely give the general principals of the method and explain the proper functioning of the program.

The method used in the program operates through the generation of a model potential. Radial wavefunctions are then obtained by the numerical integration of the Schrödinger equation over this potential. The energy levels resulting from this potential are then compared to those known through quantum defect theory. An iterative process adjusts the parameters of the potential involved until the wavefunctions give the correct values for the Rydberg levels.

The program which uses this model potential technique can be found on the computer "Zoom" at $E{:}\backslash datavault\backslash matrixelem$. The operation of the program is fairly straightforward. The command "eigencalc(n,l)" will use the model potential method to generate the wavefunction for the n,l state, generated as "Psi". This state must then be stored as Psi0 for later integration. Again, run the command "eigencalc(n′, l′)" to obtain the wavefunction for the coupled state. The evaluation of $\int r dr P_{n_e l_e}(r) P_{n_g l_g}(r)$ is then performed with the command "print matrixelem". The output of this command will be the value $\langle r \rangle$ in units of Bohr radii, and is used as explained in Appendix B.

B. THADLAB RABI FREQUENCY

The calculation of Rabi frequencies, and from them excitation rates, is an important aspect of many problems described in this dissertation. It deserves particular attention resulting from the fact that Thadlab defines and uses the term slightly differently than the conventional method. In most textbooks, the Rabi frequency is defined as:

$$\frac{\Omega}{2} = \langle e| \frac{e\vec{r} \cdot \vec{E}}{\hbar} |g\rangle . \tag{B.1}$$

As a result of this definition, the evolution of atomic populations goes as

$$\frac{dC_e}{dt} \propto \frac{\Omega}{2} C_g. \tag{B.2}$$

In order to avoid carrying this factor of $\frac{1}{2}$ throughout long problems, and as a matter of convenience, traditionally Thadlab members have defined the Rabi frequency as

$$\epsilon = \frac{\Omega}{2} = \langle e| \frac{e\vec{r} \cdot \vec{E}}{\hbar} |g\rangle . \tag{B.3}$$

This is the way Rabi frequency is used throughout this dissertation and various calculations, and it is important to keep in mind. The effect of this definition on the most common calculated values is shown in table B.1. This problem is made even more complicated by differing standards on the definition of electric field. Many textbooks define the electric field (for example, [Metcalf and van der Straten, 1999] [Loudon, 2000]) as $E = E_0 \cos(kz - \omega t) = \frac{E_0}{2} e^{ikz-\omega t} + c.c.$, while Thadlab is based off

Parameter	Standard notation	Thadlab notation
Rabi Frequency	Ω	$\epsilon = \frac{\Omega}{2}$
Two-photon Rabi	$\frac{\Omega_1\Omega_2}{2\Delta}$	$\frac{\epsilon_1\epsilon_2}{\Delta}$
AC Stark Shift	$\frac{\Omega^2}{4\Delta}$	$\frac{\epsilon^2}{\Delta}$
Excitation Rate	$\frac{\Omega^2}{\Gamma}$	$\frac{4\epsilon^2}{\Gamma}$

Tab. B.1: The definition of various parameters using both the standard notation and the "Thadlab" notation for easy comparison.

the definition $E = E_0 e^{ikz-\omega t} + c.c.$. As a result, the equation for Rabi frequency found in these textbooks appears consistent with the Thadlab definition, but is not. This issue has been the source of numerous difficulties in previous calculations, and should always be dealt with carefully.

With an understanding of this distinction, I now turn our attention to the way in which this is typically calculated in the lab. A more convenient expression than eqn. B.3 is desired, which can then be calculated fairly quickly using the program described in Appendix A.

Assuming z polarized light, and averaging over the m levels gives

$$\epsilon^2 = \frac{e^2E^2}{\hbar^2}\frac{1}{2J_g+1}\sum_m \langle J_e m_e|\, z\, |J_g m_g\rangle^2 . \tag{B.4}$$

At this point it is convenient to introduce the average oscillator strength,

$$\bar{f} = \frac{2m\omega}{3\hbar(2J_g+1)}\sum_m \langle J_e m_e|\, z\, |J_g m_g\rangle^2 . \tag{B.5}$$

Substituting eqn. B.5 into eqn. B.4, we find that

$$\epsilon^2 = \frac{e^2E^2\bar{f}}{2\hbar m\omega}, \tag{B.6}$$

which can be put into a more convenient form of

$$\epsilon^2 = \frac{\pi\alpha^2 a_0 I\bar{f}\lambda}{h}. \tag{B.7}$$

This can be easily calculated if the intensity, transition wavelength, and average oscillator strength are known. This is generally the starting point for calculating Rabi frequencies. The main calculation is then the average oscillator strength, which requires careful calculation of the matrix element. If we begin with the general oscillator strength between two levels, $|nFm_F\rangle$, this is expressed as:

$$f = \frac{2m\omega}{3\hbar(2F_g+1)} \sum_{m_g m_e} |\langle F_e m_e| r |F_g m_g\rangle|^2. \tag{B.8}$$

Using the Wigner-Eckart Theorem [Sakurai, 1994], the dependence on magnetic quantum numbers and light polarization can be taken into account by 3j symbols, which here sum to one. As a result,

$$f = \frac{2m\omega}{3\hbar(2F_g+1)} \langle F_e| |r| |F_g\rangle^2 . \tag{B.9}$$

This can be further put in terms of a matrix element without hyperfine structure, since

$$\langle F_e| |r| |F_g\rangle^2 = (2F_e+1)(2F_g+1) \begin{Bmatrix} F_e & 1 & F_g \\ J_g & I & J_e \end{Bmatrix}^2 \langle J_e| |r| |J_g\rangle^2 \tag{B.10}$$

giving

$$\begin{aligned} f &= \frac{2m\omega}{3\hbar(2J_g+1)} \langle J_e| |r| |J_g\rangle^2 (2F_e+1)(2F_g+1) \begin{Bmatrix} F_e & 1 & F_g \\ J_g & I & J_e \end{Bmatrix}^2 \\ &= f_{J_g J_e} \left[(2F_e+1)(2F_g+1) \begin{Bmatrix} F_e & 1 & F_g \\ J_g & I & J_e \end{Bmatrix}^2 \right]. \end{aligned} \tag{B.11}$$

For excitation to the Rydberg states, we must sum over the excited state hyperfine states, since the hyperfine manifold cannot be distinguished. The sum of the term in [] over the hyperfine excited states gives one, resulting in a oscillator strength which is

independent of F_g. Similarly to eqn. B.12, we can write

$$\langle J_e|\,|r|\,|J_g\rangle^2 = (2JF_e+1)(2J_g+1)\begin{Bmatrix} J_e & 1 & J_g \\ L_g & 1/2 & L_e \end{Bmatrix}^2 \langle L_e|\,|r|\,|L_g\rangle^2\,, \tag{B.12}$$

giving

$$f = \frac{2m\omega}{3\hbar(2L_g+1)}\langle L_e|\,|r|\,|L_g\rangle^2\,(2J_e+1)(2J_g+1)\begin{Bmatrix} J_e & 1 & J_g \\ L_g & 1/2 & L_e \end{Bmatrix}^2. \tag{B.13}$$

Finally, since the program described in Appendix A calculates $\langle r\rangle = \int r dr P_{n_e l_e}(r) P_{n_g l_g}(r)$, we wish to express the oscillator strength in terms of this. The final evaluation of the oscillator strength can be written as

$$f = \frac{2m\omega}{3\hbar}\frac{L_>}{(2L_g+1)}\,\langle r\rangle^2\,(2J_e+1)(2J_g+1)\begin{Bmatrix} J_e & 1 & J_g \\ L_g & 1/2 & L_e \end{Bmatrix}^2. \tag{B.14}$$

This is evaluated for the particular states of interest in our experiment, and is then used to obtain the Rabi frequencies involved using eqn. B.7.

C. CALCULATION OF MICROWAVE COUPLED ATOM-ATOM INTERACTIONS

The purpose of this Appendix is to explain the means in which the atom-atom interactions strengths for microwave coupling were calculated. It will begin with a simplified picture assuming only one m_J level. Following this calculation will be an explanation of the calculations that arrive from the presence of multiple m_J levels, and the method used to calculate the average interactions factor β.

We begin with the wavefunction of $|ns_{1/2}\rangle$ microwave coupled to $|np_{1/2}\rangle$, as discussed in Section 6.2. It is assumed that these microwaves are linearly polarized on the z-axis. This is again written as

$$|\Psi\rangle = \frac{|s\rangle \pm |p\rangle\, e^{-i\omega t}}{\sqrt{2}}. \tag{C.1}$$

In general, the dipole-dipole interaction can be written as:

$$V_{dd} = -\frac{e^2}{R^3}(3(\vec{r_1}\cdot\hat{R})(\hat{R}\cdot\vec{r_2}) - \vec{r_1}\cdot\vec{r_2}), \tag{C.2}$$

where r_1, r_2 are the orientation of the two dipoles and $\hat{R}$ is the unit vector along the axis of atomic separation.

If it is assumed the atom must remain in a single m_J level, no procession around the z-axis is possible. This gives

$$V_{dd} = -\frac{e^2}{R^3}(3\cos\Theta^2\langle\tilde{z}\rangle^2 - \langle\tilde{z}\rangle^2), \tag{C.3}$$

with

$$\langle\tilde{z}\rangle = \frac{1}{2}(e^{i\omega t}\langle p|\, z\,|s\rangle + e^{-i\omega t}\langle s|\, z\,|p\rangle\,. \tag{C.4}$$

Taking the time average of $\langle\tilde{z}\rangle^2$ eliminates the terms of order $e^{\pm 2i\omega t}$, and results in:

$$V_{dd} = -\frac{e^2}{R^3}\frac{1}{2}(3\cos\Theta^2 - 1)\left\langle p\right| z \left|s\right\rangle^2 . \tag{C.5}$$

This is nearly identical to the case of steady state electric fields, but differs by the factor $\frac{1}{2}$ due to the time dependence of the microwave field.

The situation becomes much more complicated when multiple m_J levels are taken into account. The Hamiltonian for the microwave coupling can be written:

$$H_\mu = \begin{pmatrix} 0 & \mu \\ \mu^\dagger & 0 \end{pmatrix} \tag{C.6}$$

where μ is a 2x2 diagonal matrix coupling the m_J levels of the $|ns_{1/2}\rangle$ and $|np_{1/2}\rangle$ for linearly polarized microwaves. Solving this system gives

$$\Psi_p = \frac{\mu\Psi_s}{E}, \tag{C.7}$$

where E is the eigenvalue, $E = \sqrt{\mu^\dagger\mu}$.

We are interested in the dipole-dipole interaction between two such coupled atoms, $\langle\Psi_1\Psi_2|\, V_{dd}\,|\Psi_1\Psi_2\rangle$, which can be written from Eqn. C.1 as

$$\frac{1}{4}\left\langle(\Psi_{1s} + \Psi_{1p}e^{-i\omega t})(\Psi_{2s} + \Psi_{2p}e^{-i\omega t})\right| V_{dd} \left|(\Psi_{1s} + \Psi_{1p}e^{-i\omega t})(\Psi_{2s} + \Psi_{2p}e^{-i\omega t})\right\rangle . \tag{C.8}$$

The dipole-dipole interaction requires each atom makes transitions between states of opposite parity. Using this fact, Equation C.7, and eliminating the oscillating terms gives:

$$\frac{1}{4}(\langle\Psi_{1s}\ \frac{\mu}{E}\Psi_{2s}|\, V_{dd}\,|\frac{\mu}{E}\Psi_{1s}\ \Psi_{2s}\rangle + \langle\frac{\mu}{E}\Psi_{1s}\ \Psi_{2s}|\, V_{dd}\,|\Psi_{1s}\ \frac{\mu}{E}\Psi_{2s}\rangle). \tag{C.9}$$

At this point, the problem can be more easily solved through the use of spherical tensor algebra. Using [Varshalovich *et al.*, 1988] equations {3.2.1.19} and {5.2.8.40}, Equation C.2 can be written

$$V_{dd} = -\frac{e^2}{R^3}\sqrt{24\pi}\{\{r_1 \otimes r_2\}_2 \otimes Y_2\}_0, \tag{C.10}$$

where Y_2 represents the spherical harmonics and $\otimes$ the Kronecker spherical tensor product for matrices. In addition,

$$\{r_1 \otimes r_2\}_{2M} = \frac{\langle p_{1/2}| \, |r| \, |s_{1/2}\rangle^2}{3} \left[\{T_1^{sp} \otimes T_1^{ps}\}_{2M} + \{T_1^{ps} \otimes T_1^{sp}\}_{2M}\right] \tag{C.11}$$

and

$$\{T_1^{sp} \otimes T_1^{ps}\}_{2M} = \sum_n C^{2M}_{1n\ 1M-n}\ T^{sp}_{1n} \otimes T^{ps}_{1M-n}. \tag{C.12}$$

Calculating the matrix element as described in Appendix B and incorporating the microwave coupling $\mu = \sqrt{2}T^j_{10}1/2$, $\mu^\dagger = (-1)^{j-\frac{1}{2}}\sqrt{2}T^{1/2j}_{10}$ leads to the expression:

$$V_{dd} = (-1)^{j+\frac{1}{2}} \frac{e^2\langle r\rangle^2}{R^3} \frac{\sqrt{24\pi}(2j+1)}{36} \left\{(\{\mu^\dagger T_1^{j\,\frac{1}{2}} \otimes T_1^{\frac{1}{2}j}\mu\}_2 + \{T_1^{\frac{1}{2}j}\mu \otimes \mu^\dagger T_1^{j\,\frac{1}{2}}\}_2) \otimes Y_2\right\}_0. \tag{C.13}$$

Here j has been left general for either the 1/2 or 3/2 state.

The 4x4 matrix C.13 is diagonalized in Mathematica to give the eigenvalues of the system, which are discussed in Section 7.4 and shown in Figure 7.3 for coupling to $p_{1/2}$. In this case the average interaction strength was $\beta = .076$, though one channel had zero microwave coupled interaction, and would only be limited by the van der Waals interaction. The $p_{3/2}$ was also calculated, which did not have this zero channel, with $\beta = .091$.

BIBLIOGRAPHY

[Afrousheh *et al.*, 2004] K. Afrousheh, P. Bohlouli Z., D. Vagale, A. Mugford, M. Fedorov, and J. D. D. Martin, "Spectroscopic observation of resonant electric dipole-dipole interactions between cold Rydberg atoms", Phys. Rev. Lett. **93**, 233001 (2004).

[Afrousheh *et al.*, 2006] K. Afrousheh, P. Bohlouli-Zanjani, J. D. Carter, A. Mugford, and J. D. D. Martin, "Resonant electric dipole-dipole interactions between cold Rydberg atoms in a magnetic field", Phys. Rev. Lett. **73**, 063403 (2006).

[Amthor *et al.*, 2007] T. Amthor, M. Reetz-Lamour, S. Westermann, J. Denskat, and M. Weidemüller, "Mechanical Effect of van der Waals Interactions Observed in Real Time in an Ultracold Rydberg Gas", Phys. Rev. Lett. **98**, 023004 (2007).

[Anderson *et al.*, 1998] W. R. Anderson, J. R. Veale, and T. F. Gallagher, "Resonant Dipole-Dipole Energy Transfer in a Nearby Frozen Rydberg Gas", Phys. Rev. Lett. **80**, 249 (1998).

[Autler and Townes, 1955] S. H. Autler and C. H. Townes, "Stark Effect in Rapidly Varying Fields", Phys. Rev. **100** , 703 (1955).

[Bendkowsky *et al.*, 2009] Vera Bendkowsky, Bjrn Butscher, Johannes Nipper, James P. Shaffer, Robert Lw, and Tilman Pfau, "Observation of ultralong-range Rydberg molecules", Nature, **458**, 1005 (2009).

[Beterov *et al.* (2007)] I. I. Beterov, D. B. Tretyakov, I. I. Ryabtsev, A. Ekers, and N. Bezuglov, "Ionization of sodium and rubidium nS, nP, and nD Rydberg atoms by blackbody radiation", Phys. Rev. A **75**, 052720 (2007).

[Bloembergen, 1996] N. Bloembergen, *Nonlinear Optics*, (World Scientific Publishing, Singapore, 1996.)

[Bohlouli-Zanjani *et al.*, 2007] P. Bohlouli-Zanjani, J. A. Petrus, and J. D. D. Martin, "Enhancement of Rydberg Atom Interactions Using ac Stark Shifts", Phys. Rev. Lett. **98**, 203005 (2007).

[Bohlouli-Zanjani *et al.*, 2006] P. Bohlouli-Zanjani, K. Afrousheh, and J. D. D. Martin, "Optical transfer cavity stabilization using current-modulated injection-locked diode lasers", Rev. Sci. Instrum. **77**, 093105 (2006).

[Brekke *et al.*, 2008] E. Brekke, J. O. Day, and T. G. Walker, "Four-Wave Mixing in Ultracold Atoms using Intermediate Rydberg States", Phys. Rev. A **78**, 063830 (2008).

[Brion *et al.*, 2007] E. Brion, K. Molmer, and M. Saffman, "Quantum Computing with Collective Ensembles of Multilevel Systems", Phys. Rev. Lett. **99**, 260501 (2007).

[Carroll *et al.*, 2006] T. J. Carroll, S. Sunder, and M. W. Noel, "Many-body interactions in a sample of ultracold Rydberg atoms with varying dimensions and densities", Phys. Rev. A **73**, 032725 (2006).

[Cronin *et al.*, 1982] M. Cronin-Golomb, B. Fisher, J. O. White, and A. Yariv, "Passeive (Self-Pumped), Phase Conjugate Mirror: Theoretical and Experimental Investigation", Appl. Phys. Lett. **41**, 689-691 (1982).

[Cotter *et al.*, 1977] C. Cotter, D. C. Hanna, H. W. Tuttlebee, and M. A. Yuratich, "Stimulated hyper-Raman emission from sodium vapor", Opt. Commun. **22**, 190 (1977).

[Cubel Liebisch *et al.*, 2005] T. Cubel Liebisch, A. Reinhard, P. R. Berman, and G. Raithel, "Atom Counting Statistics in Ensembles of Interacting Rydberg Atoms", Phys. Rev. Lett. **95**, 253002 (2005); Phys. Rev. Lett. **98**, 109903(E) (2007) .

[Day *et al.*, 2008b] J. O. Day, E. Brekke, and T. G. Walker, "Dynamics of low-density ultracold Rydberg gases", Phys. Rev. A **77** 052712 (2008).

[Day, 2008] J. O. Day, "Progress Towards the Creation of an On-Demand Single Photon Source Using Rydberg Atoms", Doctoral Thesis, University of Wisconsin-Madison, (2008).

[Dicke, 1954] R. H. Dicke, "Coherence in Spontaneous Radiation Processes", Phys. Rev. **93**, 99 (1954).

[Farooqi *et al.*, 2003] S. M. Farooqi, D. Tong, S. Krishnan, J. Stanojevic, Y. P. Zhang, J. R. Enshwer, A. S. Estrin, C. Boisseau. R. Cote, E. E. Eyler, and P. L. Gould, "Long-Range Molecular Resonance in Cold Rydberg Gas", Phys. Rev. Lett. **91**, 183002 (2003).

[Gaëtan *et al.*, 2009] A. Gaëtan, Y. Miroshnychenko, T. Wilk, A. Chotia, M. Viteau, D. Comparat, P. Pillet, A. Browaeys, and P. Grangier, "Observation of collective excitation of two individual atoms in the Rydberg blockade regime", Nature Physics, **5**, 115 (2009).

[Gallagher, 1994] T. F. Gallagher, *Rydberg Atoms*, (Cambridge University Press, Cambridge, 1994.)

[Greene *et al.*, 2000] C. H. Greene, A. S. Dickinson, and H. R. Sadeghpour, "Creation of Polar and Nonpolar Ultra-Long-Range Rydberg Molecules", Phys. Rev. Lett. **85**, 2458 (2000).

[Gross and Haroche, 1982] M. Gross, and S. Haroche, "Superradiance: An Essay on the Theory of Collective Spontaneous Emission", Phys. Rep. **93** 301 (1982).

[Grover, 1996] L. Grover, "A Fast Quantum Mechanical Algorithm for Database Search", arXiv:quant-ph/9605043v3 (1996).

[Gounand *et al.*, 1979] F. Gounand, M. Hugon, P. R. Fournier, and J. Berlande, "Superradiant cascading effects in rubidium Rydberg levels", Journal of Physics B **12**, 547 (1979).

[Han and Gallagher, 2009] J. Han and T. F. Gallagher, "Millimeter-wave rubidium Rydberg van der Waals spectroscopy", Phys. Rev. A **79**, 053409 (2009).

[Han *et al.*, 2006] J. Han, Y. Jamil, D. V. L. Norum, P. J. Tanner, and T. F. Gallagher, "Rb nf quantum defects from millimeter-wave spectroscopy of cold ^{85}Rb Rydberg atoms", Phys. Rev. A **74**, 054502 (2006).

[Heidemann *et al.*, 2007] R. Heidemann, U. Raitzsch, V. Bendkowsky, B. Butscher, R. Löw, L. Santos, and T. Pfau, "Evidence for coherent collective Rydberg excitation in the strong blockade regime", Phys. Rev. Lett. **99**, 163601 (2007).

[Heidemann *et al.*, 2008] R. Heidemann, U. Raitzsch, V. Bendkowsky, B. Butscher, R. Löw, and T. Pfau, "Rydberg Excitation of Bose-Einstein Condensates", Phys. Rev. Lett. **100**, 033601 (2008).

[Hyafil *et al.*, 2004] P. Hyafil, J. Mozley, A. Perrin, J. Tailleur, G. Nogues, M. Brune, J. M. Raimond, and S. Haroche, "Coherence-Preserving Trap Architecture for Long-Term Control of Giant Ryberg Atoms", Phys. Rev. Lett. **93**, 103001 (2004).

[Jackson, 1999] J. D. Jackson, *Classical Electrodynamics*, (John Wiley and Sons, Inc., New York, 1999.)

[Jaksch *et al.*, 2000] D. Jaksch, J. I. Cirac, P. Zoller, S. L. Rolston, R. Cote, M. D. Lukin, "Fast Quantum Gates for Neutral Atoms", Phys. Rev. Lett **85**, 2208 (2000).

[Johnson *et al.*, 2008] T. A. Johnson, E. Urban, T. Henage, L. Isenhower, D. D. Yavuz, T. G. Walker, and M. Saffman "Rabi Oscillations between Ground and Rydberg States with Dipole-Dipole Atomic Interactions", Phys. Rev. Lett **100**, 113003 (2008).

[Ketterle *et al.*, 1993] W. Ketterle, K. B. Davis, M. A. Joffee, A. Martin, and D. E. Pritchard, "High densisites of cold atoms in a *dark* spontaneous-force optical trap", Phys. Rev. Lett. **70**, 2253 (1993).

[Killian *et al.*, 1999] T. C. Killian, S. Kulin, S. D. Bergeson, L. A. Orozco, C. Orzel, and S. L. Rolston, "Creation of an Ultracold Neutral Plasma", Phys. Rev. Lett. **83**, 4776 (1999).

[Li *et al.*, 2003] W. Li, I. Mourachko, M. W. Noel, and T. F. Gallagher, "Millimeter-wave Spectroscopy of Cold Rb Rydberg Atoms in a Magneto-Optical Trap: Quantum Defects of the ns, np, and nd series", Phys. Rev. A **67**, 052502 (2003).

[Li *et al.*, 2004] W. Li, M. W. Noel, P. J. Tanner, and T. F. Gallagher, "Evolution dynamics of a dense frozen Rydberg gas to plasma", Phys. Rev. A **70**, 042713 (2004).

[Li *et al.*, 2005] W. Li, P. J. Tanner, and T. F. Gallagher, "Dipole-Dipole Excitation and Ionization in an Ultracold Gas of Rydberg Atoms", Phys. Rev. Lett. **94**, 173001 (2005).

[Loudon, 2000] Rodney Loudon, *The Quantum Theory of Light*, (Oxford University Press, Oxford, 2000.)

[Löw *et al.*, 2009] R. Löw, H. Weimer, U. Raitzsch, R. Heidemann, V. Bendkowsky, B. Butscher, H. P. Büchler, and T. Pfau, "Universal scaling in a strongly interacting Rydberg gas", ArXiv:0902.4523v1 (2009).

[Ludvigsen *et al.*, 1998] H. Ludvigsen, M. Tossavainen, and M. Kaivola, "Laser linewidth measurements using self-homodyne detection with short delay", Opt. Comm. **155**, 180 (1998).

[Lukin *et al.*, 2001] M. D. Lukin, M. Fleischauer, R. Cote, L. M. Duan, D. Jaksch, J. I. Cirac, and P. Zoller, "Dipole Blockade and Quantum Information Processing in Mesoscopic Atomic Ensembles", Phys. Rev. Lett. **87**, 037901 (2001).

[Marinescu *et al.*, 1994] M. Marinescu, H. R. Sadeghpour, and A. Dalgarno, "Dispersion coefficients for alkali-metal dimers", Phys. Rev. A **49**, 982 (1994).

[Metcalf and van der Straten, 1999] H. Metcalf and P. van der Straten, *Laser Cooling ad Trapping*, (Springer-Verlag, New York, 1999.)

[Mohapatra *et al.*, 2007] A. K. Mohapatra, T. R. Jackson, and C. S. Adams, "Coherent Optical Detection of Highly Excited Rydberg States Using Electromagnetically Induced Transparency", Phys. Rev. Lett. **98** 113003 (2007).

[Newell, 2003] R. T. R. Newell, "Cold and Dense Clouds of Atoms in a Holographic Atom Trap", Doctoral Thesis, University of Wisconsin-Madison, (2003).

[Nielsen *et al.*, 2000] M. A. Nielsen, and I. L. Chuang, *Quantum Computation and Quantum Information*, (Cambridge University Press, New York, 2000.)

[Reetz-Lamour *et al.*, 2008] M. Reetz-Lamour, T. Amthor, J. Deiglmayr, and M. Weidemuller, "Rabi Oscillations and Excitation Trapping in the Coherent Excitation of a Mesoscopic Frozen Rydberg Gas", arXiv:0711.4321v2 (2008).

[Rehler and Eberly, 1971] N. E. Rehler and J. H. Eberly, "Superradiance", Phys. Rev. A **3**, 1735 (1971).

[Robinson *et al.*, 2000] M. P. Robinson, B. Laburthe Tolra, M. W. Noel, T. F. Gallagher, and P. Pillet, "Spontaneous Evolution of Rydberg Atoms into an Ultracold Plasma", Phys. Rev. Lett. **85**, 4466 (2000).

[Sakurai, 1994] J. J. Sakurai, *Modern Quantum Mechanics*, (Addison-Wesley, New York, 1994.)

[Saffman and Walker, 2002] M. Saffman and T. G. Walker, "Engineering single atom and single photon sources from entangled atomic ensembles", Phys. Rev. A **66**, 065403 (2002).

[Saffman and Walker, 2005] M. Saffman and T. G. Walker, "Entangling single- and N-atom qubits for fast quantum state detection and transmission", Phys. Rev. A **72**, 042302 (2005).

[Saffman and Walker, 2005] M. Saffman and T. G. Walker, "Analysis of a quantum logic device based on dipole-dipole interactions of optically trapped Rydberg atoms", Phys. Rev. A **72**, 022347 (2005).

[Sebby-Strabley, 2004] J. Sebby-Strabley, "Demonstration of Dense Mesoscopic Atomic Clouds in a Holographic Atom Trap", Doctoral Thesis, University of Wisconsin-Madison, (2004).

[Sebby-Strabley *et al.*, 2005] J. Sebby-Strabley, R. T. R. Newell, J. O. Day, E. Breeke, and T. G. Walker, "High Density Mesoscopic Atom Clouds in a Holographic Atom Trap", Phys. Rev. A **71**, 021401(R) (2005).

[Shor, 1996] P. Shor, "Polynomial-Time Algorithms for Prime Factorization and Discrete Logarithms on a Quantum Computer", arXiv:quant-ph/9508027v2 (1996).

[Singer *et al.*, 2004] K. Singer, M. Reetz-Lamour, T. Amthor, L. G. Marcassa, and M. Weidemüller, "Suppression of Excitation and Spectral Broadening Induced by Interaction in a Cold Gas of Rydberg Atoms," Phys. Rev. Lett. **93**, 163001 (2004).

[Singer *et al.*, 2005] K. Singer, M. Reetz-Lamour, T. Amthor, S. Fölling, M. Tscherneck, and M. Weidemüller, "Spectroscopy of an ultracold Rydberg gas and signatures of Rydberg-Rydberg interactions", J. Phys. B **38**, S321 (2005).

[Sorokin *et al.*, 1973] P. P. Sorokin, J. J. Wynne, and J. R. Lankard, "Tunable coherent IR source based upon four-wave parametric conversion in alkali metal vapors", Appl. Phys. Lett. **22**, 342 (1973).

[Stenholm, 1984] S. Stenholm, *Foundations of Laser Spectroscopy*, (John Wiley and Sons, New York, 1984.)

[Sun and Robicheaux, 2008] B. Sun and F. Robicheaux, "Spectral linewidth broadening from pair fluctuations in a frozen Rydberg gas", Phys. Rev. A **78**, 040701(R) (2008).

[Svelto, 1998] O. Svelto, *Principles of Lasers*, (Springer Science+Business Media, Inc., New York, 1998.)

[Teo *et al.*, 2003] B. K. Teo, D. Feldbaum, T. Cubel, J. R. Guest, P. R. Berman, and G. Raithel, "Autler-Townes spectroscopy of the $5S_{1/2} - 5P_{3/2} - 44D$ cascade of Cold ^{85}Rb atoms", Phys. Rev. A **68**, 053407 (2003).

[Tong *et al.*, 2004] D. Tong, S. M. Farooqui, J. Stanojevic, S. Krishnan, Y. P. Zhang, R. Cote, E. E. Eyler, and P. L. Gould, "Local Blockade of Rydberg Excitation in an Ultracold Gas", Phys. Rev. Lett. **93**, 016406 (2004).

[Urban *et al.*, 2009] E. Urban, T. A. Johnson, T. Henage, L. Isenhower, D. D. Yavuz, T. G. Walker, and M. Saffman , "Observation of Rydberg blockade between two atoms", Nature Physics, **5**, 110 (2009).

[Varshalovich *et al.*, 1988] D. A. Varsholovich, A. N. Moskalev, and V. K. Khersonskii, *Quantum Theory of Angular Momentum*, (World Scientific, Singapore, 1988.)

[Vogt *et al.*, 2006] T. Vogt, M. Viteau, J. Zhao, A. Chotia, D. Comparat, and P. Pillet, "Dipole blockade through Rydberg Föster resonance energy transfer", Phys. Rev. Lett. **97**, 083003 (2006).

[Vogt *et al.*, 2007] T. Vogt, M. Viteau, A. Chotia, J. Zhao, D. Comparat, and P. Pillet, "Electric-Field Induced Dipole Blockade with Rydberg Atoms", Phys. Rev. Lett. **99**, 073002 (2007).

[Walker *et al.*, 1990] T. Walker, D. Sesko, C. Weman, "Collective behavior of optically trapped neutral atoms", Phys. Rev. Lett. **64**, 408 (1990).

[Walker and Saffman, 2005] T. G. Walker and M. Saffman, "Zeros of Rydberg-Rydberg Föster Interactions", J. Phys. B **38**, S309 (2005).

[Walker and Saffman, 2008] T. G. Walker and M. Saffman, " Consequences of Zeeman degeneracy for the van der Waals blockade between Rydberg atoms", Phys. Rev. A **77**, 032723 (2008).

[Walz-Flannigan *et al.*, 2004] A Walz-Flannigan, J. R. Guest, J.-H. Choi, and G. Raithel, "Cold-Rydberg-gas dynamics", Phys. Rev. A **69**, 063405 (2004).

[Wang *et al.*, 2007] T. Wang, S. F. Yelin, R. Côté, E. E. Eyler, S. M. Farooqi, P. L. Gould, M. Koštrun, D. Tong, and D. Vrinceanu, "Superradiance in ultracold Rydberg gases", Phys. Rev. A **75**, 033802 (2007).

[Weatherill, 2008] K. J. Weatherill, J. D. Pritchard, R. P. Abel, M. G. Bason, A. K. Mohapatra, and C. S. Adams, "Electromagnetically induced transparency of an interacting cold Rydberg ensemble", J. Phys. B **41**, 201002 (2008).

[Wunderlich *et al.*, 1990] R. K. Wunderlich, W. R. Garrett, R. C. Hart, M. A. Moore, and M. G. Payne, "Nonlinear optical processes near the sodium 4D two-photon resonance", Phys. Rev. A **41**, 6345 (1990).

[Yelin *et al.*, 2005] S. F. Yelin, M. Kostrun, T. Wang, and M. Fleischhauer, "Correlation in superradiance: A closed-form approach to cooperative effects", arXiv:0509184v1 (2005).

[Yariv, 1971] A. Yariv, *Introduction to Optical Electronics*, (Holt, Rinehart and Winston, Inc., New York, 1971.)

[Yavuz *et al.*, 2009] D. D. Yavuz, N. A. Proite, and J. T. Green, "Nanometer-scale optical traps using atomic state localization", Phys. Rev. A **79**, 055401 (2009).